2-1-2019

Numerical modeling and optimization study for the geometry of film cooling holes

Mohammad Mahmoud Alshehaby

The American University in Cairo
School of Science and Engineering

NUMERICAL MODELING AND OPTIMIZATION STUDY FOR THE GEOMETRY OF FILM COOLING HOLES

A Thesis Submitted to
Department of mechanical engineering

in partial fulfillment of the requirements for the degree of
Master of Science in Mechanical Engineering

by **Mohammad Mahmoud Alshehaby**

under the supervision of **Dr. Lamyaa El-Gabry**
Associate Professor, Department of Mechanical Engineering
The American University in Cairo

September, 2018

To my beloved parents and siblings

ABSTRACT

Film cooling is one of the essential approaches developed to protect the gas turbine blades and vanes from the passing, very high temperature, gases. It does so through covering the surface with a film of coolant air. Experimental and numerical studies have identified the important parameters affecting the film cooling aerodynamic and thermal behavior. Nevertheless, researchers are still concerned with more enhancement of film cooling performance through deeper understanding of the parameters that control coolant jet behavior. Being an important controlling parameter, the coolant nozzle geometry has been optimized in the current study. The analysis was performed in terms of adiabatic film effectiveness and heat transfer coefficient. The remaining key parameters were neutralized through fixing the coolant pipe inlet area and the pitch-to-hole-width ratio. Realizable k-ε model with scalable wall function has been selected to perform the current numerical study, being the most suitable RANS-based tested model in predicting the experimentally reported film cooling indicators at the blowing ratio of one. After proving the model accuracy, it was utilized to verify the cooling superiority of the racetrack slot (rectangular slot with fully round ends) over the typical round hole. Afterwards, the cooling performance of the racetrack slot was investigated at different aspect ratios. The optimum recorded racetrack geometry, having an aspect ratio of seven, served as a starting point for further optimization of the coolant pipe shape utilizing ANSYS Fluent Adjoint solver. The numerical optimization tool allows for a powerful, less-constrained, irregular shape optimization. Starting from the optimum racetrack geometry, the optimum irregular pipe shape was designated in two optimization steps, through which the average adiabatic film effectiveness over the test surface has increased from 0.24 to 0.34.

KEYWORDS

CFD, Computational Fluid Dynamics, Turbulence Modeling, Gas Turbine, Flat Plate, Film Cooling, Adiabatic Film Effectiveness, CRVP, Counter Rotating Vortex Pair, Racetrack Slot, Shape Optimization, Adjoint Solver

ACKNOWLEDGEMENT

At first, praise be to Allah for his countless blessing and continuous guidance; for enlightening my way; for giving me the knowledge to think and the power to work.

Then, my sincere thanks to Dr. Lamyaa El-Gabry. Her close supervision throughout the research stages added great value to this work.

I would like also to thank Kasem Eid for introducing ICEM CFD mesh generator to me; Omar Osama for suggesting me to utilize the Adjoint solver optimization tool in my research; Mohamed Osman for being motivating, and supportive whenever needed. The useful discussion with all of you had enriched this research to be as it is now. I would like also to thank Noha Hassanin, Omar Elsherif, and Ashraf Bazan for their encouragement in the journey of my thesis.

Last but not least, I would like to express my gratitude to my family for their support and encouragement throughout the research periods.

NOMENCLATURE[1]

A	area
b	racetrack streamwise thickness
C_p	specific heat
D	diameter of film cooling round hole
h	convective heat transfer coefficient
I	coolant-to-mainstream momentum flux (dynamic pressure) ratio
k	turbulence kinetic energy
L	coolant pipe length
M	coolant-to-mainstream mass flux (blowing) ratio
Nu	Nusselt number
P	pressure
p	pitch; distance from a midway point between two adjacent holes to the next midway point
Pr	Prandtl number
q	heat flux
r	recovery factor
S	entropy
s	racetrack straight spanwise length (without rounded ends)
T	temperature
T_{static}	freestream static temperature

[1] Some outsourced figures may contain different nomenclature.

T_{total}	freestream total temperature
U	velocity in Cartesian x-direction
u	streamwise velocity
U^*	normalized U-velocity
u_τ	friction velocity; $u_\tau = \sqrt{\tau_w/\rho}$
V	volume
v	velocity
w	coolant hole's width; maximum spanwise distance of the hole
w^*	width of racetrack coolant slot, having an aspect ratio s/b=7
X	streamwise distance from circular hole leading-edge
Y	spanwise distance from hole centerline
y	first cell height (normal to wall)
Z	vertical distance from flat plate surface
Γ	heat diffusivity
δ_{99}	boundary layer thickness
ε	turbulence dissipation rate
ζ	adiabatic film effectiveness
θ	normalized air temperature
λ	thermal conductivity
μ	viscosity
ρ	density
σ_k	turbulent kinetic energy Prandtl number

σ_ϵ	turbulent dissipation rate Prandtl number
τ_w	wall shear stress

Abbreviations

CFD	Computational Fluid Dynamics
CRVP	Counter Rotating Vortex Pair
EARSM	Explicit Algebraic Reynolds Stress Model
LES	Large-Eddy Simulation
NGV	Nozzle Guide Vanes
RANS	Reynolds-averaged Navier–Stokes
RNG	Renormalization Group
SST	Shear Stress Transport

Subscripts

av	area-weighted average
aw	adiabatic wall
c	coolant
f	facet of mesh element
rec	recovery
sur	surface
t	turbulent
∞	mainstream inlet

TABLE OF CONTENTS

LIST OF TABLES

LIST OF FIGURES

1. INTRODUCTION

1.1. Gas Turbine

Brayton cycle is the ideal model for gas turbine engines. Its main components; *the compressor, the combustion chamber, and the expander*, are illustrated, along with thermodynamic P-V and T-S diagrams, in Figure 1.1. However, gas turbines typically operate in *open cycles* [1] at which fresh air's pressure and temperature are increased within the compressor, then the temperature is elevated during the combustion process in the combustion chamber. The resulting high enthalpy gases expand, partially, within the turbine to generate the shaft work required to drive the compressor. The remaining energy is used either; to create thrust downstream the propelling nozzle in aircraft engines, or to generate extra shaft work through additional turbine's stages in industrial gas engines. [2]

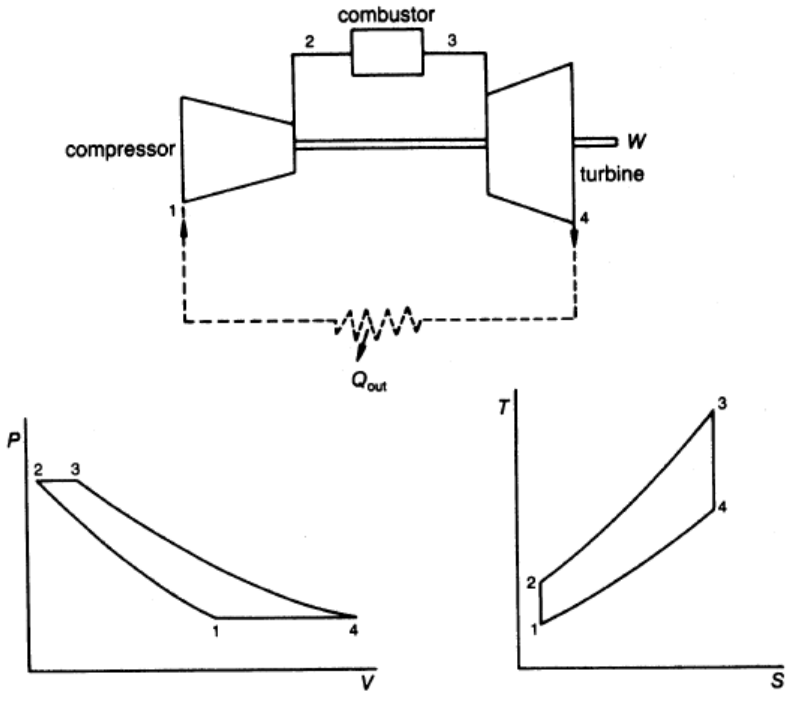

Figure 1.1: Main components, and P-V and T-S diagrams of standard Brayton cycle [3]

Increasing both pressure ratio, to a certain limit, and firing temperature are necessary to optimize the gas turbine efficiency [3]. Figure 1.2 shows the overall cycle thermal efficiency against pressure ratio for different firing temperatures.

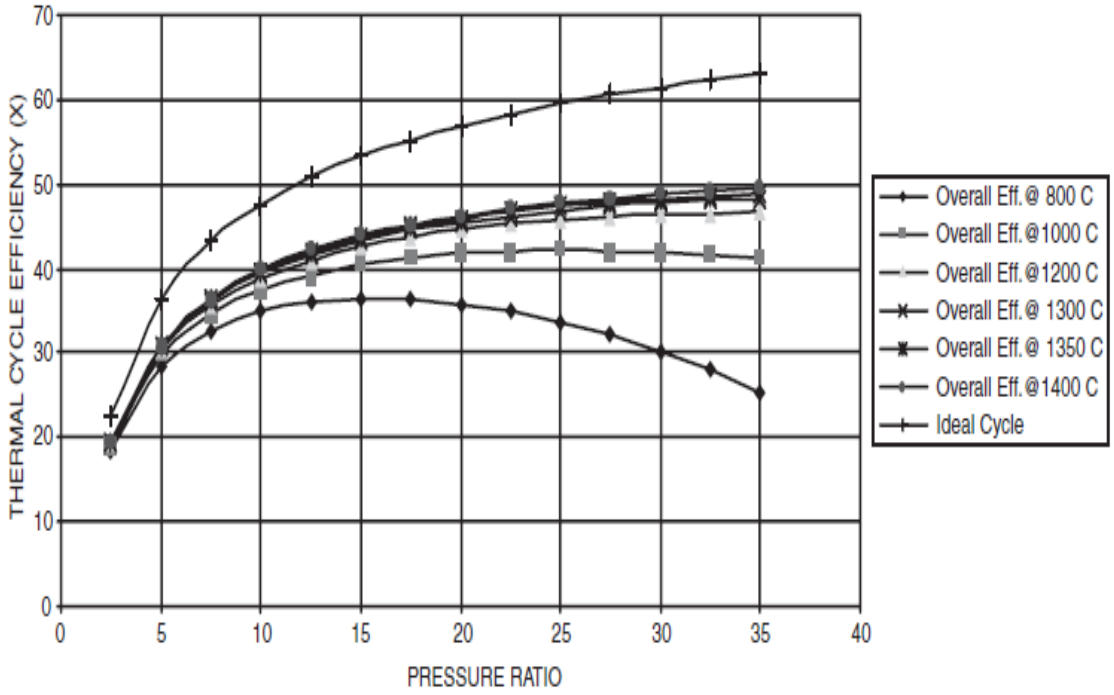

Figure 1.2: Overall cycle thermal efficiency against pressure ratio for different firing temperatures [3]

Focusing on long life service, industrial gas turbines were more conservative in terms of pressure ratio and firing temperature than aircraft engines which focus on higher reliability. However, by the introduction of aero-derivative gas turbines (gas turbines modified from concurrent lighter aircraft engines) to the industrial sector in the early 1990s, the performance gap between both disciplines of gas turbines started to diminish [3, 4]. Figure 1.3 is a picture of a typical commercial aircraft gas engine (*Rolls-Royce Trent 1000*), while Figure 1.4 presents the main components of a medium size industrial gas turbine (*Solar Turbines*).

Figure 1.3: Rolls-Royce Trent 1000 engine presented at Goodwin Hall, Virginia Tech, Blacksburg, VA, USA [2]

[2] The photo was taken by the author.

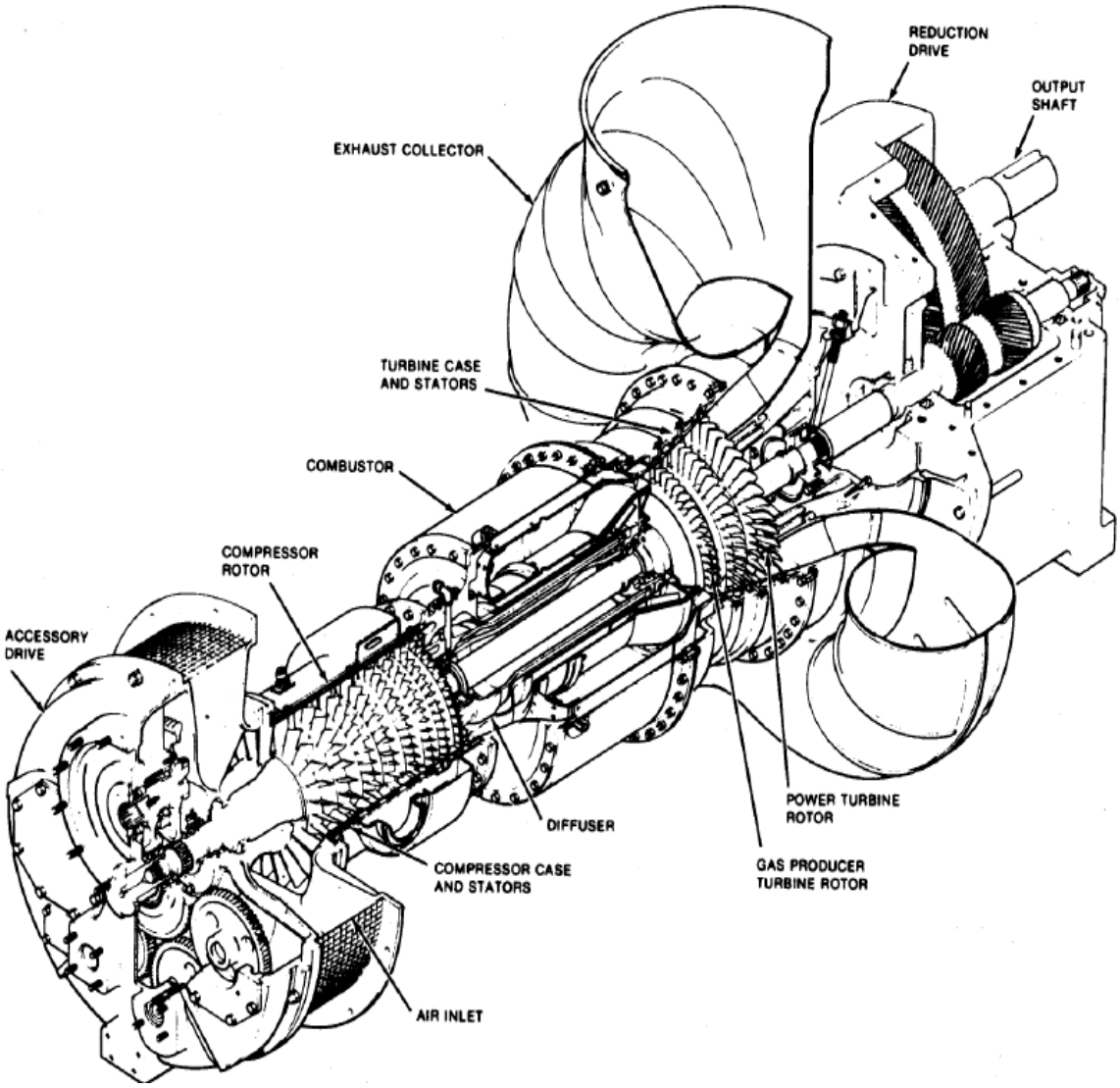

Figure 1.4: Medium size industrial gas turbine (Solar Turbines) [3]

To improve the overall efficiency of gas turbine's cycle, three main areas have been subjected to continuous design development: increasing the efficiencies of turbomachinery components in compressors and turbines, modifying the basic cycle by introducing intercooling, regeneration, and/or reheating, and increasing the turbine inlet (or firing) temperature [1]. Limited to a certain inlet temperature, early issuances of gas turbines were working under low efficiency conditions; as low as 15% in the early 1950s. With continuous development in both blades' metallurgy and cooling systems design, the working conditions

(firing temperature and pressure ratio) for new gas turbines has been considerably elevated from the early 1950s till the present time: from 800 °C to 1600 °C inlet temperature, and from less than 10:1 to 40:1 pressure ratio. The result is a significant growth in turbines' overall thermal efficiency; from 15% in the early 1950s to more than 45% nowadays. [3]

However, some components such as nozzle guide vanes (NGV) may fail under this elevated inlet temperature which excessively exceeds the permissible metal temperature. The problem is addressed by using advanced cooling schemes to properly cool the metal surface, guaranteeing that its temperature doesn't exceed the permissible one [5]. **Two main cooling schemes**, are developed to protect the critical turbine components: **internal cooling** at which air is bled from the compressor then pass through cooling passages inside the blade body; and **film cooling** at which the compressed bled air is ejected through holes, or slits, on the blade surface to cover and protect it from mainstream hot gases. Both cooling techniques are essential for modern gas turbines design. Nevertheless, only film cooling is the subject of the current study.

1.2. Film Cooling

As demonstrated in Figure 1.5, "Film cooling is the introduction of a secondary fluid (coolant or injected fluid) at one or more discrete locations along a surface exposed to a high temperature environment to protect that surface not only in the immediate region of injection, but also in the downstream region" [6]. It is one of the most effective cooling mechanisms in gas turbines because, unlike internal cooling which removes the heat inside the blade's body, it spreads a coolant layer between the hot gas stream and the objective surface. Additionally, heat inside the blade body is removed partially through the coolant flow before leaving the hole's exit [5]. Film cooling with injection through continuous slot is a two-dimensional

phenomenon which allowed for simple analytical model's development [2]. However, three-dimensional film cooling flow associated with discrete coolant holes gradually becomes a two-dimensional phenomenon at the far downstream distance. [7]

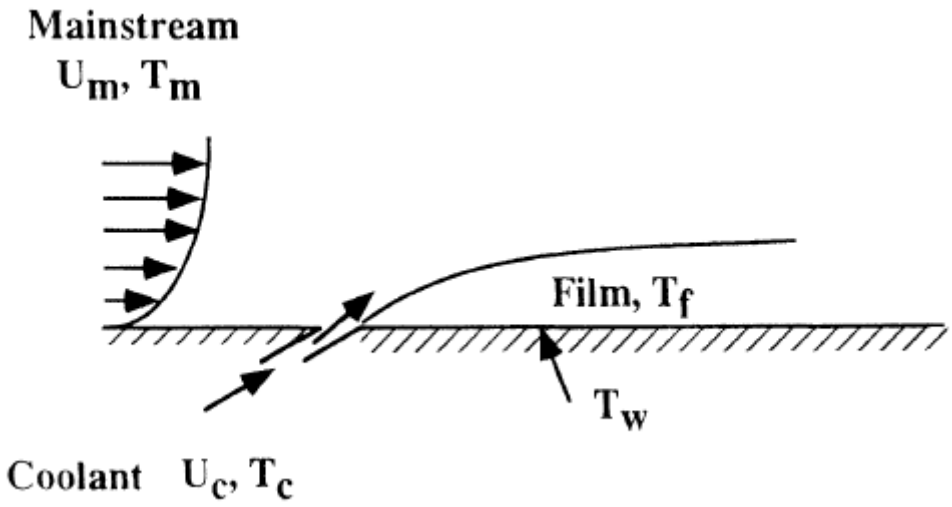

Figure 1.5: Schematic of film cooling concept [8]

Proper cooling design aims, not only to cool the blades' surface using minimum amount of coolant air, but to ensure a uniform temperature distribution [2] and to limit the coolant penetration into the mainstream hot gases as well. The uniform temperature distribution prevents thermal stresses for the blades' body, while the penetration of the coolant into the mainstream increases the turbine's aerodynamic losses. Figure 1.6 shows a typical film cooling nozzles distribution in turbine's high-pressure NGV section.

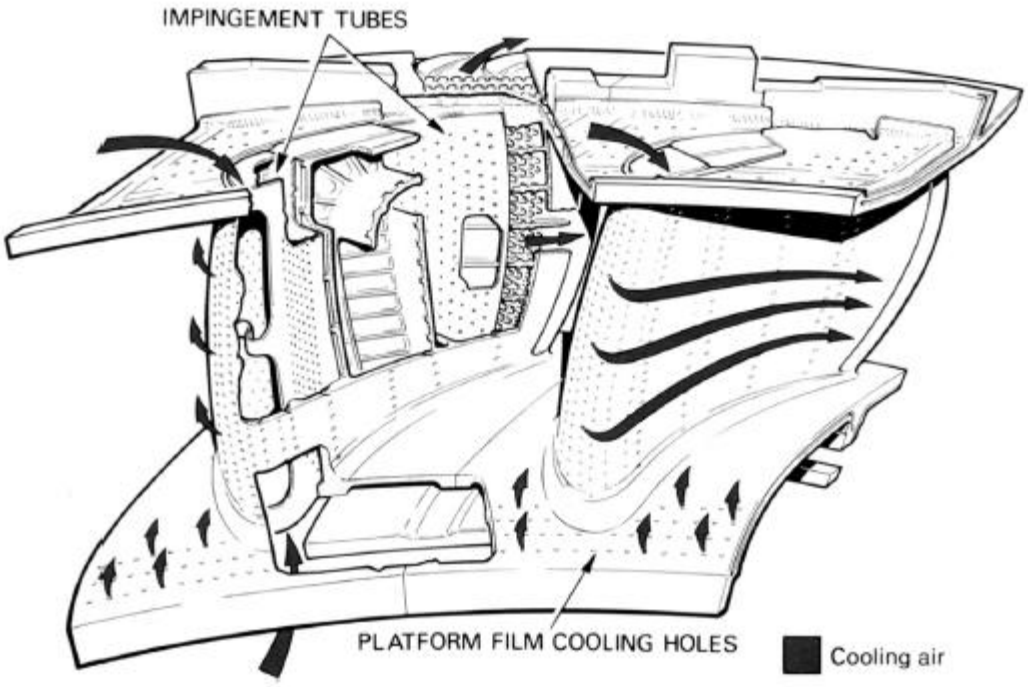

Figure 1.6: Film cooling nozzles distribution in turbine's high-pressure NGV section (Source: Rolls Royce) [4]

One of the most significant aerodynamic feature associated with the film cooling process is the formation of two counter rotating vortex pair (CRVP). Figure 1.7 displays CRVP, along with other important aerodynamic phenomena accompanying the ejected coolant; the shear layer and the wake region. CRVP associated with the coolant jet ejected from discrete holes evolves in size and moves, within the jet, in the three-dimensions. Its size and position have a great influence on the jet attachment/detachment pattern, and the flow aerodynamic losses. [9]

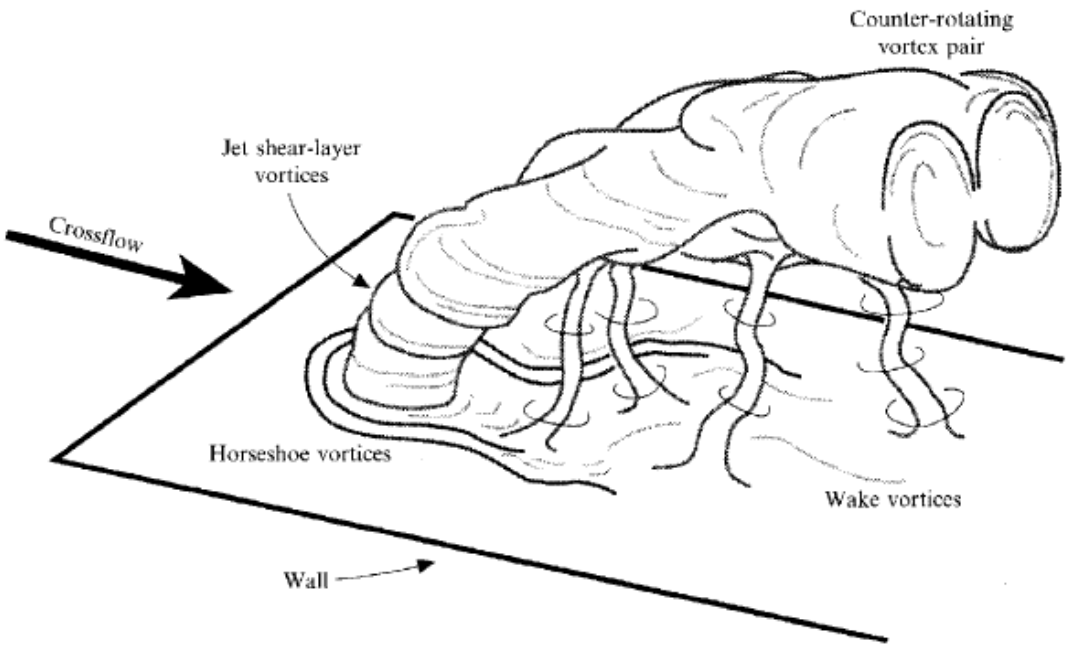

Figure 1.7: Schematic of important aerodynamic jet features [10]

2. LITERATURE REVIEW AND RESEARCH OBJECTIVE

2.1. Film Cooling Affecting Parameters

The turbine thermal and aerodynamic performances are influenced greatly by film cooling. Through deeper understanding of the important parameters affecting the coolant jet behavior, researchers hope to achieve more control on the jet optimizing its cooling effect along with turbine efficiency. The most important parameters, as established by accumulative dense studies, can be classified under two main categories: the flow (coolant/mainstream) conditions, and the geometry and configuration of coolant holes. The relevance and importance of each parameter has been carefully explored through numerous of experimental and numerical studies as shown in the coming subsections.

2.1.1. **The Effect of Flow (Coolant/Mainstream) Conditions**

Density ratio, velocity ratio, blowing (mass flux) ratio, momentum flux (dynamic pressure) ratio, freestream turbulence, upstream boundary layer thickness, and mainstream pressure gradient; all these coolant/mainstream's flow parameters were found to affect the film cooling performance. Among these parameters, both blowing and momentum flux ratios, defined by Equation 1.1 and Equation 1.2 respectively, were more investigated [2] due to the continuous debate about the comparative importance and relevance of each at different locations downstream the coolant hole.

$$M = {\rho_c v_c}/{\rho_\infty v_\infty} \qquad (1.1)$$

$$I = {\rho_c {v_c}^2}/{\rho_\infty {v_\infty}^2} \qquad (1.2)$$

Density, Velocity, Mass Flux, and Momentum Flux Ratios

The blowing ratio indicates the coolant-to-mainstream relative thermal capacity. The higher the blowing ratio, the better the film cooling effect. Nevertheless, too high blowing ratio usually leads to a jet lift-off which reduces the film cooling effect. The typical range of the blowing ratios in gas turbine airfoil is from 0.5 to 2.0. On the other hand, the range for the density ratios is from 1.5 to 2.0. [5]

Ramsey and Goldstein [11] experimentally investigated the film cooling effectiveness of 90° and 35° inclined jet. They showed that, due to the coolant jet mixing with the mainstream, the film effectiveness decreases when blowing ratio increased above the specified optimum value of 0.5 [2]. The designated optimum blowing ratios of 0.5 was verified after which by Martinez-Botas and Yuen [12] who experimentally examined the thermal jet performance over a flat plate for different holes' arrangements and jet issuance angles. The range of blowing ratios tested was varied from 0.33 to 2, while the density ratio was kept near to unity.

Utilizing Large-Eddy Simulation (LES) technique, Renze et al. [13] investigated the effect of both velocity and density ratios on film cooling aerodynamic and thermal behavior for a gas turbine blade. The coolant was injected into the main flow through 30° inclined pipe. The research finding distinguished between the near-to-hole region, at which velocity ratio was designated as the most suitable parameter that specifies the dynamic behavior of the flow field, and the far downstream region, at which mass flux ratio (i.e., both velocity and density ratios) was found to be the dominant similarity parameter affecting the cooling efficiency.

Thole et al. [14] measured the thermal field downstream of a row of inclined jets with a crossflow for a range of density ratio between 1.2 and 2 under different velocity, blowing,

and momentum flux ratios. Among these parameters, they nominated the momentum flux ratio to be the dominant scaled parameter affecting the **jet aerodynamic behavior**; the attachment to (or the detachment from) the flat plate surface, and the mixing with the freestream air. In detail; the jet was found to remain attached to the surface downstream the coolant hole until the momentum flux ratio reaches 0.4, detach then reattach for the values between 0.4 and 0.8, and finally remains detached when the momentum flux ratio exceeds 0.8. The momentum flux ratio was found to be the suitable scaled parameter that characterizes the **film thermal effect** as well. After that, a more detailed analysis to these results was conducted by Sinha et al. [15]. They combined twelve different cases of mass flux and momentum flux ratios by independently altering both density and velocity ratios to reveal their significance on the **film thermal effectiveness**. The analysis showed that: the mass flux ratio consistently scales the centerline effectiveness of the attached jet, while the momentum flux ratio generally characterizes it for the detached-reattached jet. However, the spread of the coolant film characterized by the laterally averaged film effectiveness, was found to be significantly diminishing when decreasing the density ratio and increasing the momentum flux ratio.

Freestream Turbulence

Bons et al. [16] analyzed the effect of freestream turbulence on the film cooling effectiveness downstream a single row of holes at blowing ratio ranging from 0.55 to 1.85, and freestream turbulence ranging from 0.9 to 17 percent. They found that the increased freestream turbulence has an adverse effect on the film cooling in the near vicinity of the coolant jet exit, while the coolant film diverges laterally to cover more surface area with the downstream flow movement. The experimental work of Mayhew et al. [17] concluded that, for typical round holes over a flat plate with density ratio near the unity, the freestream turbulence tends to

increase the area-averaged film effectiveness at high blowing ratio (M = 1.5), while decreasing it at low blowing ratios (M = 0.5 and 1). The increase in mixing between the jet and the mainstream was nominated as the possible reason for the freestream turbulence's favorable effect at higher blowing ratio (as it tends to reattach the higher energetic jet to the surface) and the adverse effect at lower blowing ratios (as it tends to dilute the, originally attached, lower energetic jet).

Upstream Boundary Layer

The detailed measurements of flow and film effectiveness parameters performed by Foster and Lampard [18] downstream a row of holes over a flat plate showed that; the thicker the upstream boundary layer, the more laterally diluted the film. As a result, the less effective the film becomes. The conclusion of more lateral film dilution with thicker upstream boundary layer agrees with the findings of Goldstein et al. [19] who noticed an inverse correlation between the centerline film effectiveness values and the ratio of boundary layer thickness to cylindrical coolant hole diameter. They attributed the trend to the deeper jet penetration resulting from the lower near-to-wall momentum of the thicker boundary layer. However, when the ratio of the boundary layer thickness to the hole diameter exceeds a specific value, the noticed inverse correlation tends to be invalid since no further decrease in the film effectiveness figures has been noticed, especially at higher blowing ratios and far downstream locations.

Mainstream Pressure Gradient

Teekaram et al. [20] experimentally studied the effect of the mainstream pressure gradient on the coolant film issued from an inclined two-dimensional slot and a single row of three-dimensional holes. The study showed a minimal significance of the mainstream pressure

gradient on the film effectiveness for the two-dimensional, and the attached (low blowing ratio) three-dimensional jets. The experimental work of Schmidt and Bogard [21] was limited to a single row of inclined round (three-dimensional) holes in a flat plate. The study confirms the slight impact of the mainstream pressure gradient on the three-dimensional jet when it is not completely detached. Furthermore, no effect of the mainstream pressure gradient on the completely detached jet was recorded.

2.1.2. The Effect of Coolant Hole Geometry and Configuration

In order to achieve better film cooling effect, several publications have focused on the coolant nozzle geometry parameters and configuration such as: the shape of the coolant hole exit, the arrangement and the spacing between the coolant holes, the coolant nozzle orientation (compound) angle, the coolant nozzle inclination (simple) angle, and the coolant nozzle and pipe shaping.

Coolant Hole Exit Shape

The shape of the coolant hole has a great influence on the downstream turbulent mixing process. Film cooling slots have been used in the earlier stages of gas turbine design. The superior attachment of the slot film due to the Coanda effect; *the tendency of the film to stay attached to the surface when it bends away from the jet direction*, and the spanwise uniformity of the coolant film spurred several researchers to study the film cooling slots with different shapes and arrangements [2]. Tangential slots were among the early types that were extensively experimented since they maximize the streamwise component of the jet momentum and reduce the perpendicular component, lessening the film lift-off [2]. Hartnett et al. [22] studied a tangential slot similar to the one that was used by Wieghardt [23]; shown in Figure 2.1 [2]. Seban [24] presented the step-down tangential slot, in which the slot lip allowed

the film to be injected at a lower level than the mainstream as illustrated in Figure 2.2. This approach decreased the mixing between the film and the mainstream and ensured that the film is injected at zero degree with the surface. The tangential slots have been then replaced with, more practical and easier to manufacture, straight non-tangential slots; presented in Figure 2.3. It was studied experimentally by Metzger et al. [25] to obtain heat transfer rates in near-to-injection regions.

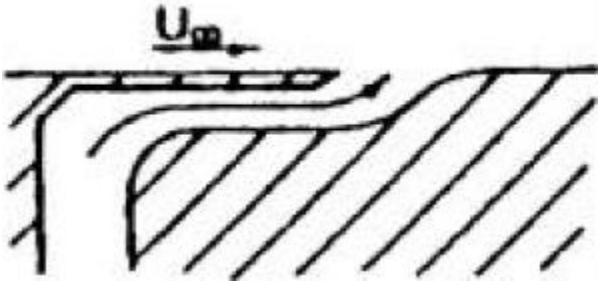

Figure 2.1: Tangential slot introduced by Wieghardt [23, 2]

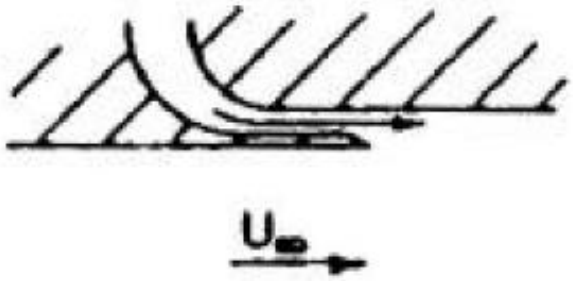

Figure 2.2: Tangential step-down slot presented by Seban [24, 2]

Figure 2.3: Straight non-tangential slot presented by Metzger [25, 2]

The geometry of the slot coolant hole reduces the strength of turbine's components. This drawback led the researchers to quickly discard farther research on the slot geometry for

the cooling of gas turbine's vanes and blades which are subjected to extremely high stresses. Nevertheless, slots are still in use for cooling the vanes' trailing edges in some turbines designs to improve their net performance by allowing thin trailing edges [26]. Discrete cooling holes are required to maintain the strength and prolong the life of the vane. Using the realizable k-ε model with Y-plus value around 30, Shalash et al. [27] compared the film cooling performance of three different discrete cooling holes illustrated in Figure 2.4: typical circular (round) hole, rectangular (isosceles trapezoid) slot, and oval (racetrack) slot. The study concluded that; for the same coolant area and pitch, the racetrack slot gives the best cooling performance in terms of adiabatic film effectiveness and jet coverage area, while the isosceles trapezoid outperforms the typical round hole, showing a minor CRVP effect. However, the experimental test of Singh et al. [28] revealed the aerodynamic advantage of the typical round hole when compared to the racetrack and the V-shape ones; illustrated in Figure 2.5. On the contrary to Shalash et al. [27], the long edge of racetrack slot studied by Singh et al. [28] was aligned parallel to the streamwise direction. The three cooling hole shapes have the same exit area, and the same spanwise spacing normalized by the jet diameter. Expressing the least flow loss, the discharge coefficient of the round hole was found to be 10% higher than that of both racetrack and V-shape ones.

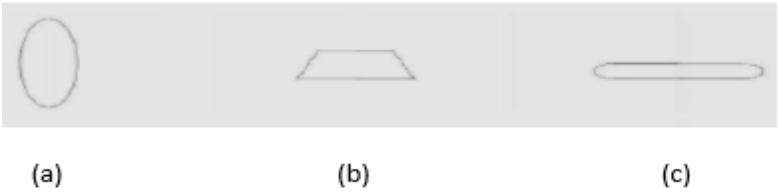

Figure 2.4: Discrete cooling holes: (a) typical circular (round) hole, (b) rectangular (isosceles trapezoid) slot, and (c) oval (racetrack) slot; studied by Shalash et al. [27]

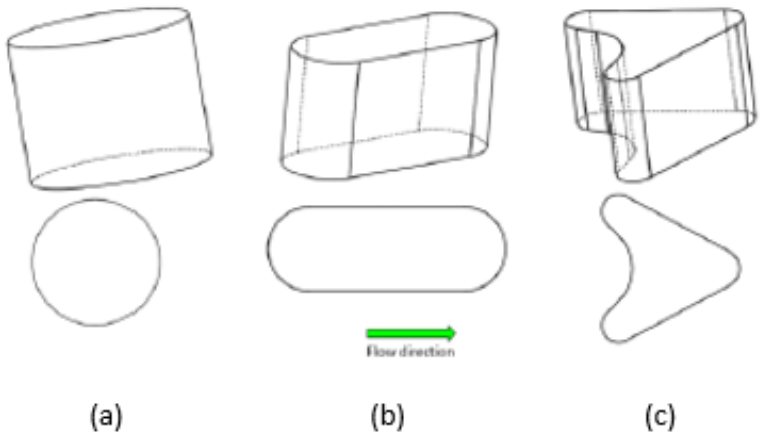

Figure 2.5: Discrete cooling holes: (a) typical round hole, (b) racetrack hole, and (c) V-shape hole; studied by Singh et al. [28]

The circular hole used to be the most common film cooling hole's shape for two major reasons: the ease of manufacturing, and the least effect on vane strength due to the absence of sharp angles. Goldstein et al. [29] experimentally studied the adiabatic film effectiveness for a cylindrical hole in a flat plate at two different angles with the surface; 35° and 90°. They found a drastic decrease in the film effectiveness of the circular hole compared to that of previously studied continuous slot. The film effectiveness deterioration was found to be more significant with the increase of the blowing ratio due to the detachment of the film air. Non-uniform distribution of the cooling air over the surface was another observed major disadvantage of the circular holes.

Arranging the film cooling holes in a staggered pattern, reducing the spanwise holes' spacing, and ejecting the coolant with an orientation (compound) angle; all of these approaches were introduced to eliminate the non-uniformity problem of the discrete cylindrical holes. On the other hand, two main approaches have been adopted to overcome the coolant jet detachment: injecting the cooling air at narrower inclination angle with the cooled surface, and introducing the coolant into the mainstream through shaped (divergent) nozzle. Some of the

attempts to evaluate the effect of the stated approaches on the film cooling performance are presented in the next few paragraphs.

Coolant Holes Arrangement and Spacing

Arranging the rows of film cooling holes in a staggered pattern enhances the uniformity of the coolant film. Alternately, the pattern of film effectiveness becomes spanwise-periodic when using only one row of the cooling holes. [30]

The spanwise spacing between film cooling holes is proved to have an impact on the film effectiveness as well. The film cooling performance is expected to be enhanced when the spacing between adjacent holes is reduced. This parameter, along with other ones, has been studied by Goldstein et al. [19] who examined the effect of the spanwise spacing between film cooling holes on the film effectiveness. The laterally averaged film cooling effectiveness decreased when the spacing was increased to 6D because no interaction between the adjacent holes was detected, and every jet behaved as a single one leaving a significant area between holes uncovered by the cooling film as shown in Figure 2.6. Ligrani et al. [31] also noticed the inverse correlation between the spanwise holes' spacing and the laterally-averaged film effectiveness values. However, the effect decreases at the far downstream region.

Foster and Lampard [18] also concluded that; the smaller the holes' spacing, the enhanced the film lateral coverage and the relaxed the jet lifting-off effect. Kruse [7], through his dense study over a range of pitch-to-diameter ratio from 1.5 to 5, referred the increase in the film effectiveness with narrower holes' spanwise spacing to the counter-rotating vortices interaction between adjacent jets which forces the jets down reducing their mixing with the mainstream. [32]

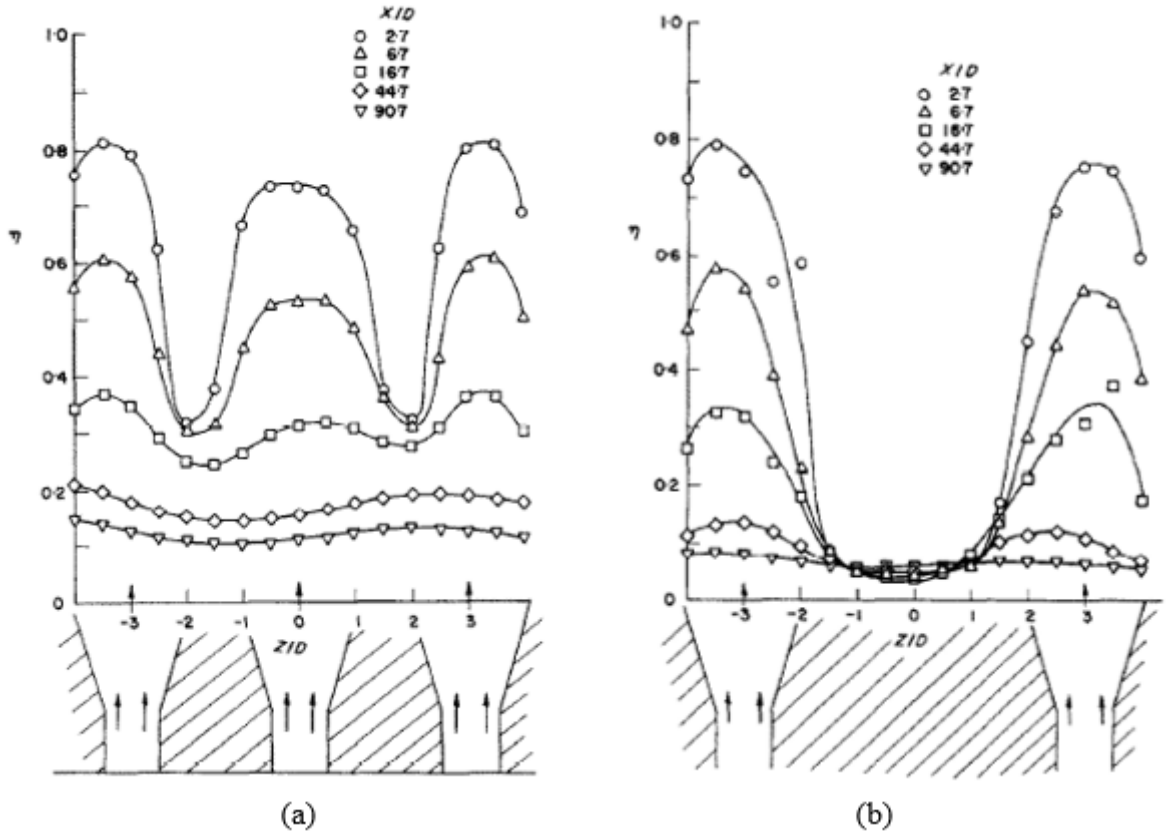

Figure 2.6: Lateral variation of film cooling effectiveness for M=0.5 downstream laterally divergent: (a) 3D spaced holes, and (b) 6D spaced holes [19]

Coolant Hole Orientation (Compound) Angle

Ligrani et al. [31], Ekkad et al. [33, 34], and Sen et al. [35] experimentally analyzed the effect of ejecting the coolant with an angle tilted away from the streamwise direction toward the spanwise one (the compound angle). The coolant, in each study, was ejected with 35° inclination angle with the surface and a range of typical blowing ratios.

Ligrani et al. [31] noticed a significant enhancement in the cooling effect when ejecting the coolant from staggered array of 30° compound angle cooling holes instead of the simple angle ones till the downstream distance X/D=60; After which, both ejection strategies approximately give the same laterally-averaged cooling effect. Gao et al. [36] attributed the common observation of the enhancement of film effectiveness with the compound angle

hole's configuration to the fact that ejected coolant is strongly bended by the mainstream momentum, covering more surface area. However, Ekkad et al. [33, 34] observed, not only the increase of film effectiveness, but also an increase in heat transfer coefficient values with the compound angle increased from 0° to 90°.

Furthermore, Sen et al. [35] evaluated the data downstream a single row of holes over a flat plate for a range of momentum flux ratios from 0.16 to 3.9. Three sets of holes, as illustrated in Figure 2.7, were investigated; round holes with simple angle, round holes with 60° compound angle, and divergent holes with 60° compound angle. The analysis differentiated between two cases: low momentum flux ratio, at which a minor effect of compound angle on the heat transfer rate was recorded; and high momentum flux ratio, at which the increase of the compound angle significantly increases the heat transfer rate, but increase the adiabatic film effectiveness values at the same time. However, the study reached to the conclusion of an adverse effect of the compound angle on the overall film cooling performance at higher momentum flux ratios.

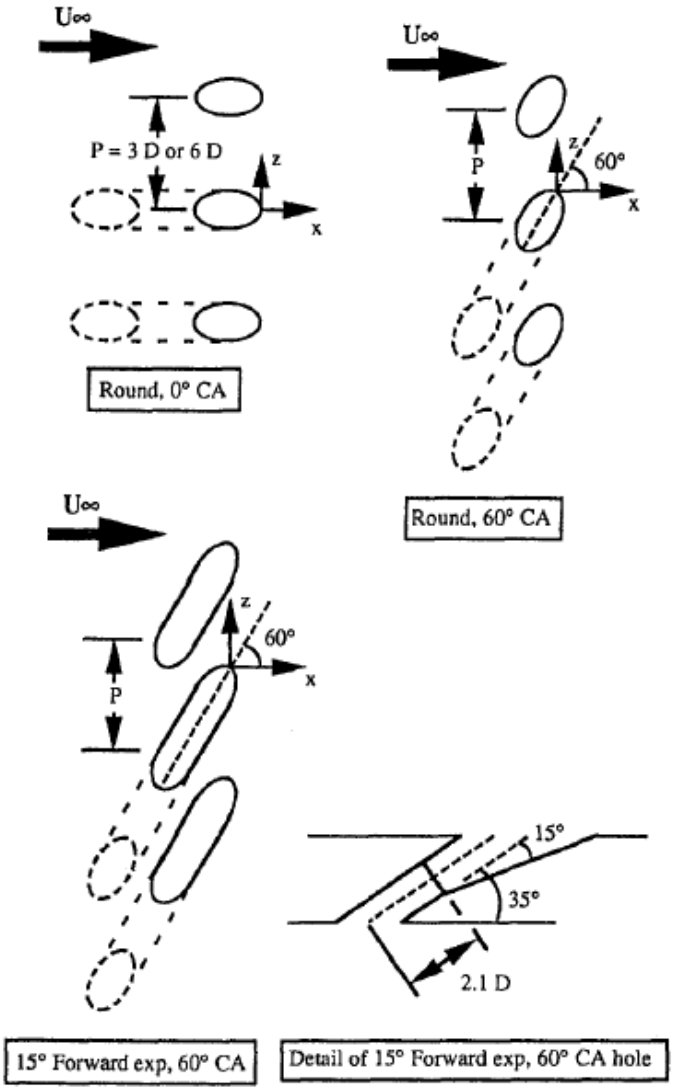

Figure 2.7: Three sets of coolant holes: round holes with simple angle, round holes with 60° compound angle, and divergent holes with 60° compound angle; investigated by Sen et al. [35]

Coolant Hole Inclination Angle

Yuen and Martines-Botas [37], and Kohli and Bogard [38] experimentally investigated and compared different round holes' inclination angles to examine their effect on the film cooling performance. The former study was performed on a flat plate for blowing ratio ranging from 0.33 to 2. Alternatively, the latter one altered the momentum flux ratio, keeping the density ratio fixed at 1.6. The general conclusion from both studies is: starting from a certain

inclination angle, *30° for* [37] *and 35° for* [38], the increase of the hole inclination angle drove down the film effectiveness. An exception at intermediate downstream regions ($7 \leq X/D \leq 26$) was mentioned by [37] when 60° inclination angle gave better effectiveness than 30°. Additionally, sharper degradation in cooling capacity associated with 55° inclination angle was mentioned by [38]. The study also revealed that the adverse effect of increased inclination angle on cooling effectiveness is more significant at higher momentum ratios. Jia et al. [39] and Akbar et al. [9] also compared different nozzles' inclination angles. The former recorded the formation of recirculation bubbles at jet angles greater than 40° for a range of blowing ratios from 2 to 9. The latter noticed, *as illustrated in* Figure 2.8, smaller, close to the wall, and away from each other CRVPs associated with smaller inclination angles; all of which delay the film separation and improve its cooling effectiveness.

Distinguished from previous general conclusion of cooling efficiency drop off when increasing the injection angle, the outcome of Foster and Lampard's study [18] differentiated between two cases: low blowing ratio, at which small injection angle gives better cooling effectiveness; and high blowing ratio, at which the opposite is true.

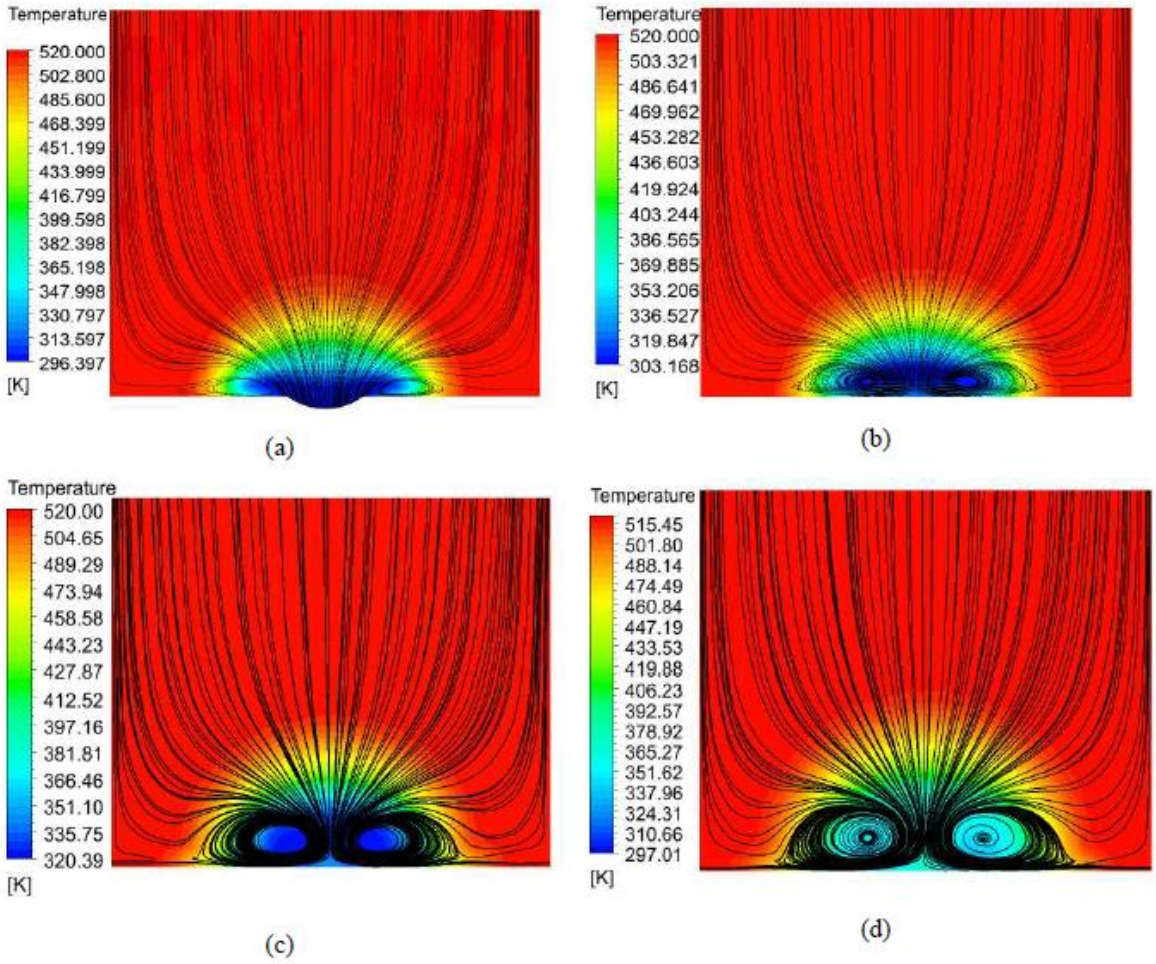

Figure 2.8: CRVP on cross-flow plane at X/D=1.0 for 1.76 density ratio; and: (a) 25°, (b) 45°, (c) 90°, and (d) 135° injection angles [9]

Coolant Nozzle and Pipe Shaping

Generally, the shaped holes outperform the regular cylindrical ones because the divergent exit of the former reduces the jet momentum, restricting its lift-off [36]. Figure 2.9 illustrates four *typical shaped film cooling nozzles*; the classic-shaped, fan-shaped, laidback, and conical film holes. The classic-shaped film nozzle expands in both lateral (like fan-shaped) and forward (like laidback) directions, while the conical one expands equally around its axis. [40]

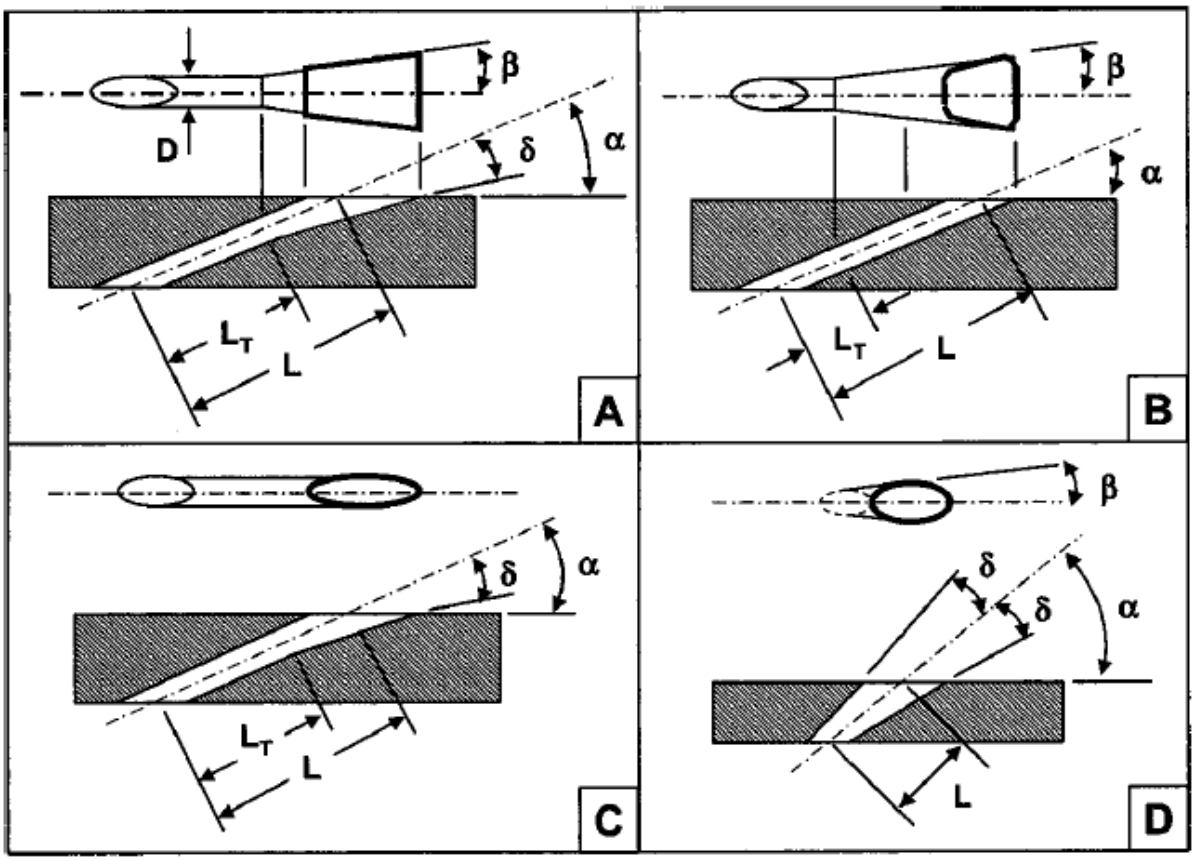

Figure 2.9: Typical shaped cooling nozzles designs: (a) classic-shaped, (b) fan-shaped, (c) laidback, and (d) conical [40]

The statement about the jet momentum reduction for the shaped nozzle agrees with the finding of Goldstein et al. [19] experimental study over a flat plate; A dramatic reduction in the jet lift-off at the 10° laterally shaped nozzle exit when compared to regular cylindrical nozzle design. As a consequence, an improvement in film effectiveness for the shaped holes over the regular cylindrical ones was recorded. Moreover, the lateral spread of the film cooling effectiveness downstream the shaped holes was enhanced, while greater variation downstream the regular cylindrical ones can be evidently noticed from Figure 2.10. Additionally, the figure shows that film cooling tends to become a two-dimensional phenomenon at the far downstream locations for both holes' designs. Colban and Thole [41] studied the fan-shaped film nozzle from both aerodynamic and thermal perspectives. The researchers attributed the more

aerodynamic losses associated with the cylindrical holes than that associated with the shaped ones, for the same flow conditions, to the higher jet separation from the blade surface accompanying with the former. The study showed that shaped holes also gave a higher cooling effect at the end-walls, making them better from both aerodynamic and thermal perspectives.

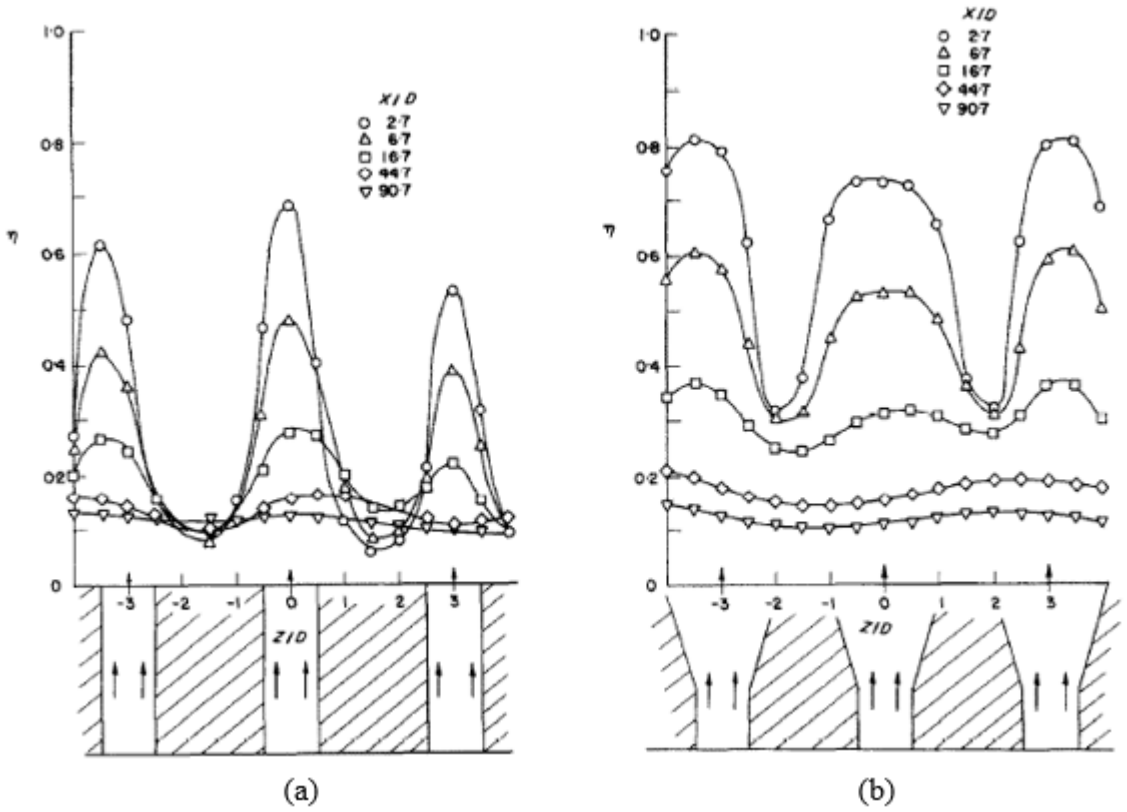

Figure 2.10: Lateral variation of film cooling effectiveness for M=0.5 downstream 3D spaced: (a) regular cylindrical holes, and (b) laterally divergent holes [19]

The higher coverage area and the better cooling performance drew the researchers' attention back to non-tangential slot film cooling. A comparison between straight and shaped slots, both are inclined at 35° with flat plate surface, has been conducted experimentally by Farmer et al. [42]. They compared the film effectiveness and the heat transfer coefficient for both configurations illustrated in Figure 2.11, having a coolant-to-mainstream density ratio of 1.55. Shaping the slot inlet and exit was found to improve the adiabatic film effectiveness and the heat transfer coefficient specially at far downstream region. However, the researchers

mentioned the necessity of detailed velocity field analysis to discover the effective aerodynamic phenomena. Hyams et al. [43] numerically studied aerodynamic and thermal performance of both straight and shaped slots. They compared slots of shaped inlet, exit and both with straight slot at blowing, density, and slot's length-to-width ratios ranging from 1-to-2, 1.5-to-2, and 3-to-4.5 respectively. They concluded that joining slot inlet and exit shaping gives best film cooling performance as it preserves the turbulence elimination effect at both slot ends. However, at low blowing ratios, the enhancement was comparable to that provided by shaping the exit only.

Figure 2.11: Straight and shaped (inlet and exit) non-tangential slots' configurations studied by Farmer et al. [42]

Advancement in manufacturing techniques motivated film cooling researches to investigate innovative coolant nozzles and holes' configurations. Sargison et al. [44] investigated the performance parameters of new patented nozzle design; *The Converging Slot-Hole (Console; for short)*, illustrated in Figure 2.12. The *Console* nozzle converges from multi near-circular shapes to a continuous slot, preserving the material mechanical strength higher than that of typical slot. The researchers compared measured data for a *Console* row with three typical rows of cylindrical, fan-shaped, and slot cooling nozzles. All configurations had the same exit area, and were inclined by 35° to a surface of flat plat at engine representative Reynolds number. A side from its mechanical integrity advantage, the results downstream the *Console* nozzle's row showed similar film cooling effectiveness and heat transfer coefficient to that of typical slot. Visualization data presented by Sargison et al. [45] verified that, similar to the slot film, the *Console* film stays attached to the surface throughout the studied range of

momentum flux ratios; from 1.1 to 40. Moreover, upstream and downstream total pressure data presented in Figure 2.13 revealed the superiority of the *Console* design from aerodynamics prospective. The comparable aerodynamic efficiency of the *Console* to that of no-coolant-flow (only mainstream) case has been attributed to the absence of flow separation inside the *Console* nozzle (due to accelerated flow), and downstream the exit. The benefits of having an accelerating coolant flow were introduced previously by Gehrer et al. [46] who numerically investigated under-expanded transonic jet that expands from a slit exit into a lower pressure mainstream flow. Due to the super attachment of the coolant film to the wall, the design was suggested for the use at blade's high curvature surfaces like the leading edge.

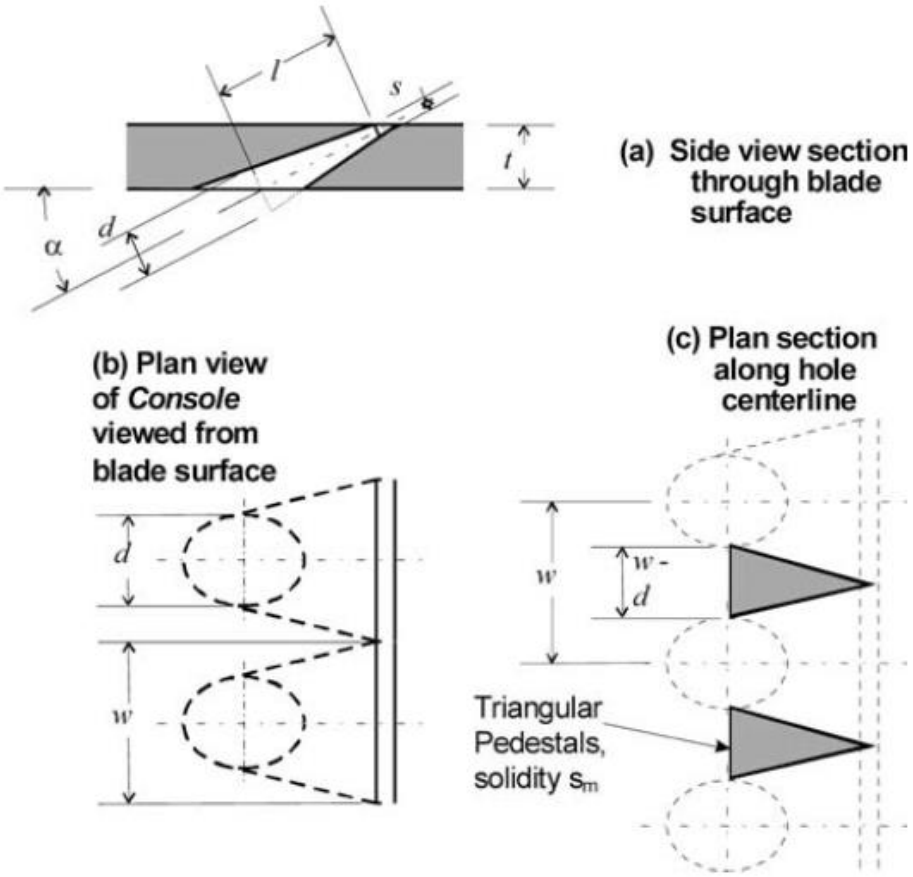

Figure 2.12: Console design investigated by Sargison et al. [45]

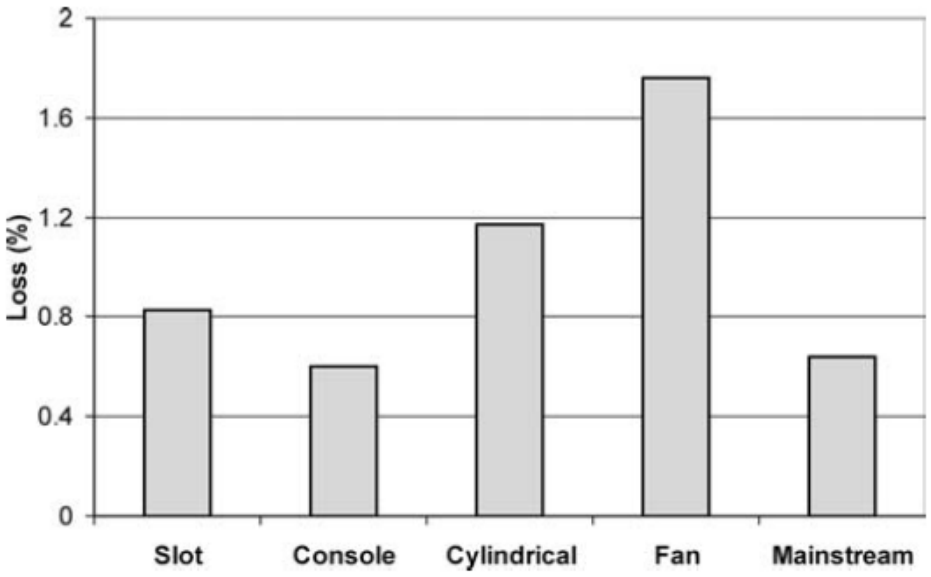

Figure 2.13: Aerodynamics loss comparison between four coolant nozzle configurations for mainstream velocity of 2.6 m/s, and momentum flux ratio of 1.1 (except for the only mainstream case) [45]

Recently; Kim et al. [47] numerically analyzed four different shaped film cooling holes; louver (classic), dumbbell, fan, and crescent; illustrated in Figure 2.14. The results show that, among the investigated four shapes, the dumbbell hole performed better in terms of spatially averaged film effectiveness, while the louver one was the worst. Nevertheless, crescent shape gave wider film coverage, biasing the coolant film away from the centerline, especially with the increase of blowing ratio.

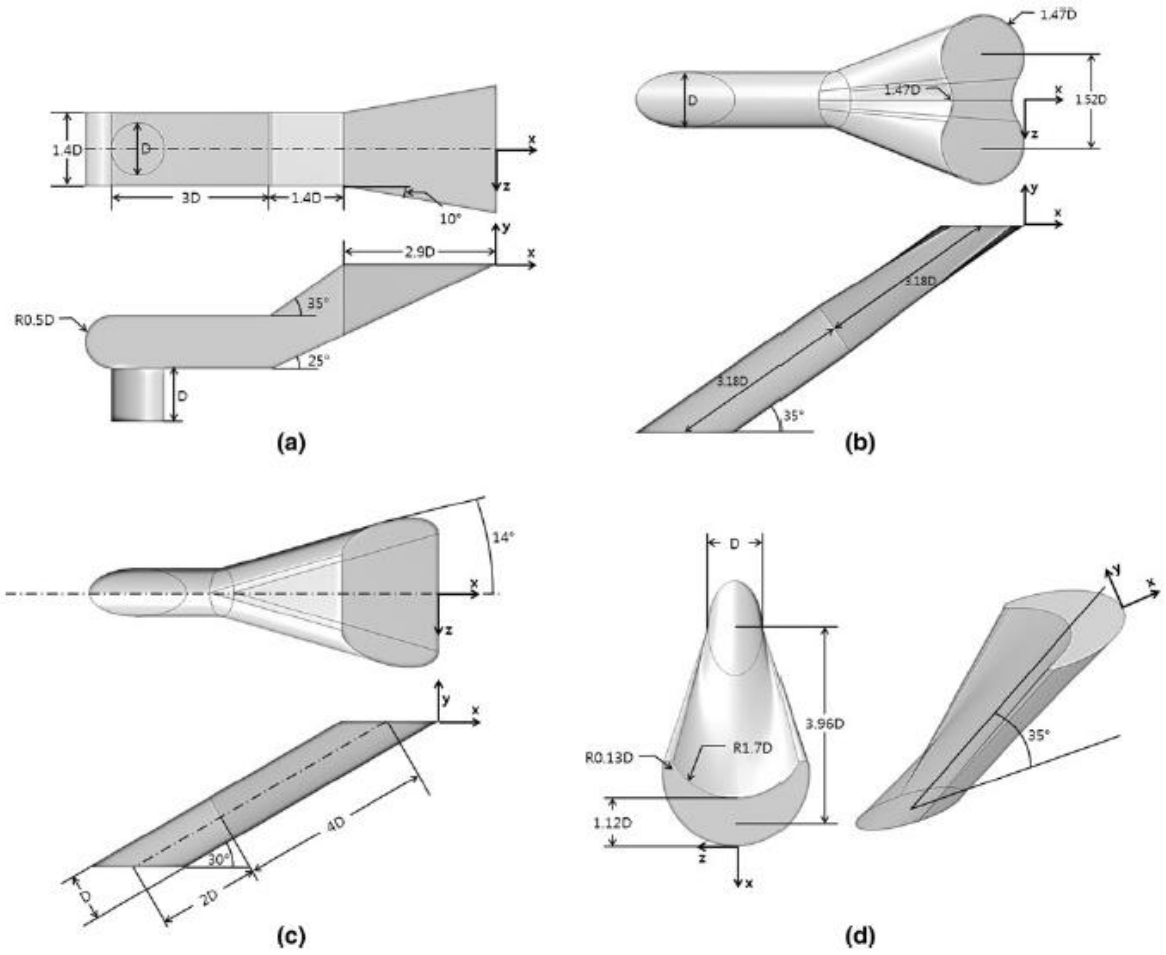

Figure 2.14: Four shaped holes: (a) louver (classic), (b) dumbbell, (c) fan, and (d) crescent; analyzed by Kim et al. [47]

Among other flow and geometry configuration parameters, Akbar et al. [9] tested the effect of forward and backward's coolant pipe curvature on the film behavior. Contrary to the forward curvature pipe, and due to inertial effect, the innovated reversed curvature pipe kept the exit coolant flow concentrated near to the trailing edge of the hole, improving its cooling effect. Velocity distribution contours at the pipe exit for both forward and backward curvature pipes, with 20D radius of curvature, is shown in Figure 2.15.

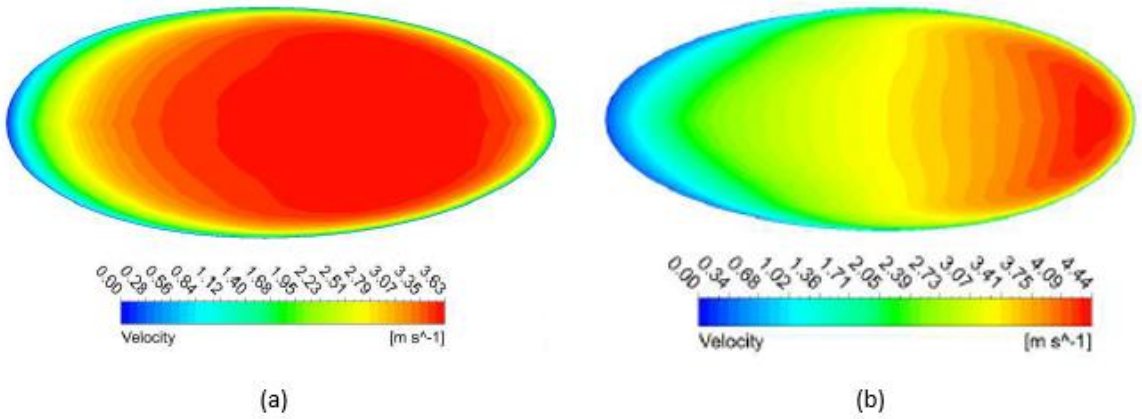

Figure 2.15: Velocity distribution contours at pipe exit for: (a) forward curvature pipe, and (b) backward curvature pipe [9]

2.2. Research Objective

The purpose of this study is to compare racetrack hole shape to the circular one to confirm that the cooling effect of the former outperforms that of the latter; After which, optimum racetrack geometry (aspect ratio) was explored and served as the baseline for novel irregular shape optimization of the cooling pipe. More explanation of the comparison conditions and the optimization analysis is held in the "Research Strategy"; *section 3.1*.

3. RESEARCH METHODOLOGY

3.1. Research Strategy

Throughout the current study, the comparison between the racetrack and the typical round hole shapes was performed by neutralizing the important parameters, other than the hole exit shape, that were proven to affect the film cooling behavior. Some of these parameters were neutralized in previous comparison [27] by fixing both the velocity ratio and the coolant cross-sectional area. Fixing these two parameters, *together with setting the same boundary temperatures (hence, the same boundary densities)*, for both cases (the circular and the racetrack ones) leads to a conclusion of fixed blowing and momentum flux ratios. Nevertheless, the lateral extent effect was eliminated by fixing the ratio of the racetrack slot width (w), *alternatively; the round hole diameter (D)*, to the pitch (p). Fixing the pitch-to-width ratio (p/w) ensures unbiased laterally and area averaged results as an inference of unbiased jet coverage indication. Hence, the observations are only outcomes of the geometric feature of the cooling hole and its effect on the flow.

After showing the racetrack slot superiority over the circular hole, the same strategy is accomplished to discover its optimum geometric variables by investigating the cooling performance over an extended range of aspect ratios; the ratio of the racetrack straight spanwise length (s) to its streamwise thickness (b), as illustrated in Figure 3.1. Afterwards, the designated racetrack optimum geometry served as a starting point for more promising irregular pipe shape optimization utilizing the capability of the *Adjoint solver*; an advanced add-on module to *ANSYS Fluent* software.

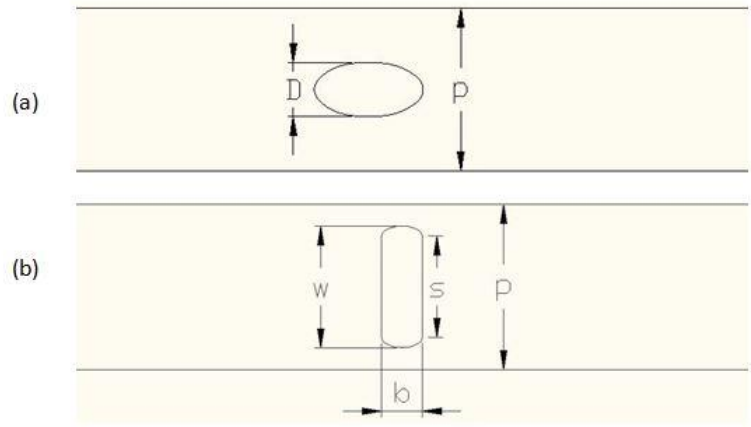

Figure 3.1: The geometric variables for; (a) circular hole and, (b) racetrack slot

In general, the performance was evaluated in terms of both centerline and laterally-averaged adiabatic film effectiveness, and Nusselt number. Furthermore, to inspect the effect of vertical and lateral dissipations on the film cooling thermal behavior, both the adiabatic film effectiveness over the whole test surface and the normalized temperature contours on different cross-flow planes were presented. Velocity field data was also analyzed and compared to temperature field ones to shed a light on the aerodynamic mechanisms that affect the normal and lateral thermal dissipation of the coolant film.

3.2. Data Used for Validation

The experiments selected to validate the current numerical study were conducted by: El-Gabry et al. [48], of which velocity field data and turbulence quantities were reported; and Thurman et al. [49], of which temperature field data and heat transfer parameters were presented. Both large scale experimental models were designed to give detailed information about the aerodynamic and thermal behavior of the flat plate film cooling at blowing ratios 1 and 2. The large scale model allows for high spatial resolution to capture the shear layer, weak

region, and other complex three-dimensional phenomena in the downstream vicinity of coolant holes. [48]

Figure 3.2 shows the three coolant holes of the experiment model. The distance from a certain hole centerline to an adjacent hole centerline; *pitch*, is 3D. Coolant air is fed through three separate flow meters to the coolant tubes and ejected from 19.05 mm (0.75 inch) diameter holes. The tubes are 30° inclined to the mainstream direction. The length of each coolant passage from the flow meter to the hole exit; *L*, is greater than 23D to effectively achieve fully developed coolant flow at the hole exit, even for the higher coolant velocity at M=2. The tests were implemented in a suction type tunnel, illustrated in Figure 3.3, of 20.32 x 20.32 cm (8 x 8 inch) cross-section and 86.36 cm (34 inch) length for the main flow domain. Before entering the test section, the mainstream air passes through a flow conditioner; a set of screens, grid, and filters. [48]

Figure 3.2: Experiment model photograph [48]

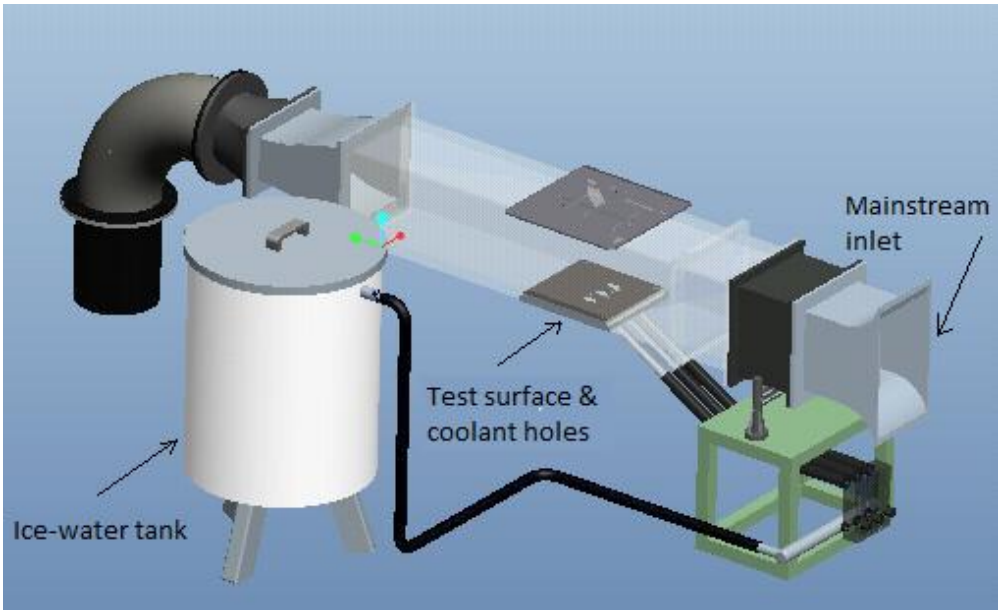

Figure 3.3: Experiment model illustration[3] [49]

The experimental research modeled three different sets of experiments according to the different required data: To measure velocity and turbulence data, the mainstream and the coolant air were kept at the same, room, temperature and no heat is transferred from, or into, the fluid domain (**adiabatic wall – flow field data**) [48]; To compare adiabatic film effectiveness values, the coolant air was cooled to 20 °C under the mainstream air temperature and no heat is transferred from, or into, the fluid domain (**adiabatic wall – thermal field data**) [49]; Lastly, To present heat transfer coefficient in terms of Nusselt number, additional to the 20 °C difference between the mainstream and the coolant air temperatures, constant heat flux was applied to the air through the test surface in the downstream vicinity of the cooling holes exits by the mean of copper bus bars (**non-adiabatic wall – thermal field data**). [49]

[3] The labels were added to the original figure to show the design components.

3.2.1. Adiabatic Flow Field Experimental Settings and Measurements

This set of experiment was designed to capture mean velocity, turbulent fluctuations, turbulent stresses, turbulent kinetic energy, and turbulent dissipation rate; along jet centerline and various cross-flow planes; downstream the coolant holes. The mean velocity and turbulent shear stress measurements were satisfactorily compared to two data sets from literature [50, 51]; thus, confirming the validity of the experimental design. [48]

The mainstream air inlet velocity is kept at 9.1 m/s (30 ft/s), and measured by the mean of Pitot tube. Velocities downstream the coolant holes were measured using hotwire probes to capture the three-dimensional velocity components and turbulent stresses. However, the mean velocity and velocity fluctuations uncertainties were less than 4% and 5% respectively, while the Reynolds stress uncertainties were typically less than 15% but were as much as 25% in some regions of high turbulence. Measurements at the inlet of test section showed freestream turbulence intensity about 4%, and boundary layer thickness; δ_{99}, about 1.27 cm (0.67D). Reynolds number, based on freestream velocity and coolant hole diameter, is 11,000. The integral (macro) and dissipation (micro) turbulent length scales at the inlet of test section were found to be 3mm (which is roughly the size of the wire mesh upstream of the test section) and 0.5 mm respectively. [48]

3.2.2. Adiabatic Thermal Field Experimental Settings and Measurements

This set of experiment was designed to determine the adiabatic film effectiveness over the flat plate test surface, and measure the temperatures across various cross-flow planes; all of which are downstream of the coolant holes. The same measurements and settings controls described for the flow field experimental set are applied to the thermal field ones as well.

Moreover, the mainstream air inlet temperature was fixed to 25 °C. It was measured, along with the coolant temperature, by the mean of open-ball thermocouples placed upstream of the holes and inside the coolant tubes respectively. The coolant was chilled to 5 °C by passing it through a copper tube coiled inside an ice-water tank as shown in Figure 3.3. The coolant passage is, then, insulated up through the holes exits. Type E thermocouple probe was utilized to measure the temperatures along the jet centerline and various cross-flow planes downstream of coolant holes; as illustrated in Figure 3.4. The finest temperature measurement resolution near to the flat plate surface was 0.254 mm. Generally, the temperature uncertainty measurements at the region of interest were found to be less than 5%. [49]

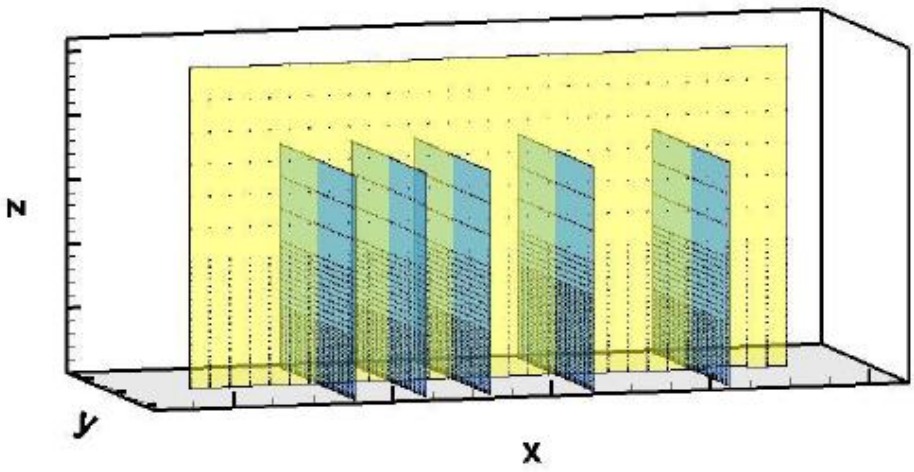

Figure 3.4: Survey planes for thermocouple probe [49]

3.2.3. Non-Adiabatic Thermal Field Experimental Settings and Measurements

This set of experiment was designed to demonstrate the heat transfer coefficient over the flat plate test surface downstream the coolant holes. The same measurements and settings controls described for both flow field and adiabatic thermal field experimental sets are applied to the non-adiabatic thermal field one as well.

Additionally, constant heat flux was applied to the flat plate test surface through cupper bus bars. The copper bus bars were attached to a thin sheet of Inconel which, in turn, was attached to the test surface. A power supply was connected to the copper bus bars to feed them with electric power and heat the test surface. The surface temperature was measured using steady state liquid crystals thermography. Both power supplied and surface temperature were recorded to generate Nusselt number contours over the flat plate test surface. [49]

3.3. Coordinates Orientation and Data Presentation[4]

The same Cartesian coordinates orientation illustrated in Figure 3.4 is used to present the current study results; The domain is symmetric about the plane [Y=0]; The test surface and the hole exit lie on the plane [Z=0]; X-coordinate is aligned with the bulk mainstream flow. To the aim of saving computational power, noticing the similarity, only one hole with one pitch (p) lateral extent is modeled for each case.

For the circular hole case, the coordinates' origin is set at the coolant hole leading-edge; so that the *circular coolant hole* extends from [X/D=0] to [X/D=2] in streamwise direction, and from [Y/D=-0.5] to [Y/D=0.5] in the spanwise direction; to be consistent with the experimental results illustrations. For all other hole shapes representations, the trailing-edges were kept at [X/D=2] regardless of hole extent in X-dimension; hence, regardless of the leading-edge position. The characteristic length selected to spatially normalize X-dimension for all the studied cooling hole shapes is the circular pipe diameter; D. The above routine facilitated the data comparison at the same downstream distances directly from the results illustrations.

[4] It is recommended to review this section to clear any confusion about the presentation of the results.

Satisfying the comparison conditions described in the "Research Strategy"; *section 3.1*, Y-dimension was spatially normalized by the coolant hole diameter (D) or width (w) for the circular and the other hole shapes respectively. An exception is made for the last stage when comparing the performance of the different nozzle geometries under the condition of equal coolant mass flux per pitch. In this case, Y-dimension was spatially normalized by a selected single coolant hole width (w) regardless of each hole width or dimeter.

However, the spatial normalization of Z-dimension in each normal-to-wall data illustration depends on the companion one in the following manner; For XZ center-plane representation, both dimensions are normalized by the round hole diameter (D) to keep the relative spatial consistency for the jet propagation; For YZ planes representations, Z-dimension is normalized by selected constant hole width (w*) to fit the purpose from the comparison by showing correct relative vertical penetration of the coolant jet, even for different hole geometries.

3.4. Numerical Modeling for the Case M=1

3.4.1. Mesh Generation

Non-uniform hexahedral structured grid was generated using ANSYS ICEM CFD 17.1 mesh generator. Figure 3.5 shows general view of the domain's surface grid. Finer mesh structure was assigned for the region of interest downstream the coolant jet exit hole, at which high turbulence and rapid changes in fluid properties is expected, to capture the gradient of the fluid properties efficiently. O-grid configuration was generated to preserve the grid quality when meshing round passages. Figure 3.6 and Figure 3.7 display the generated O-grid at the circular and the racetrack pipes' inlet planes respectively.

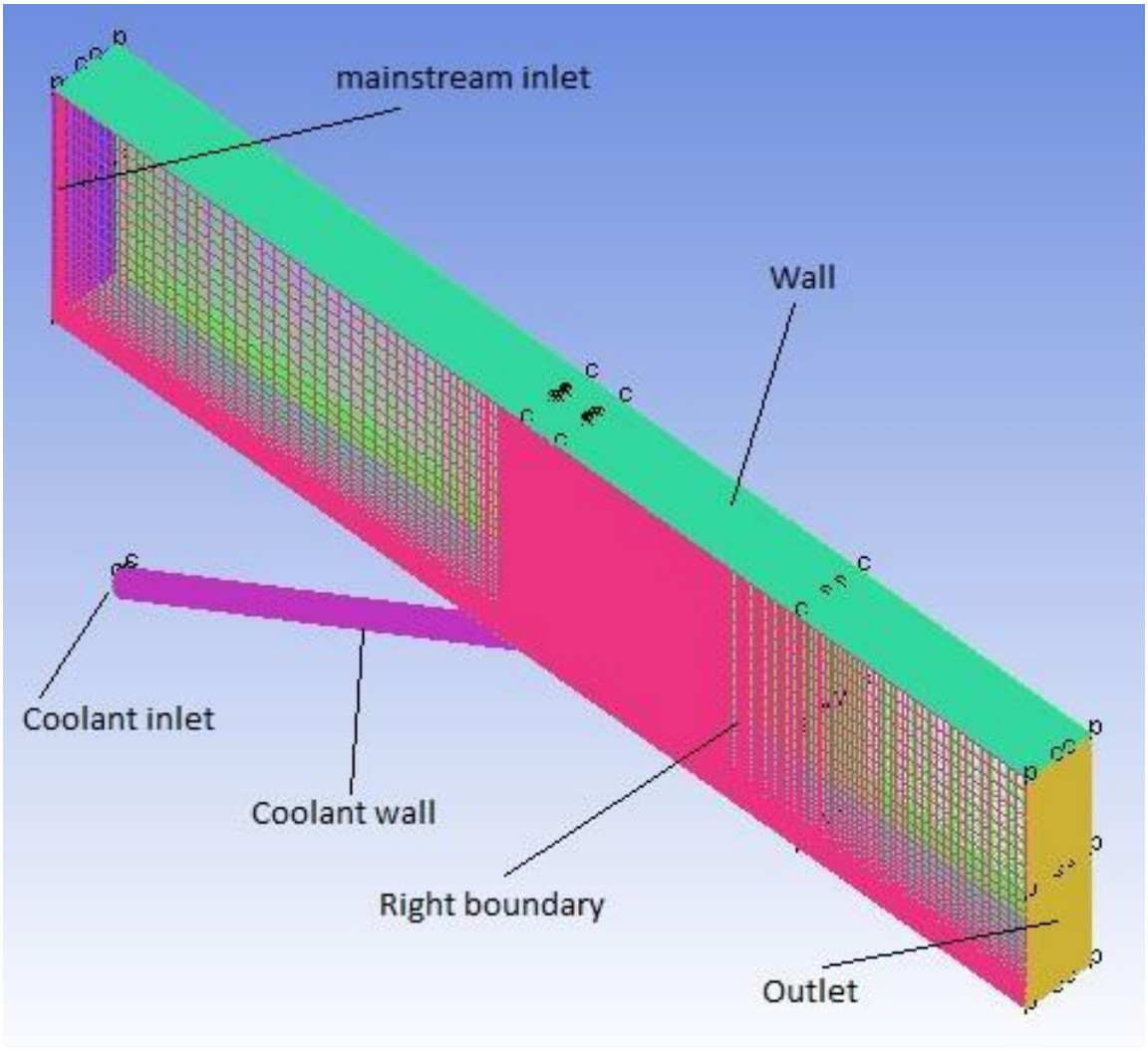

Figure 3.5: The domain boundaries, extent and surface grid

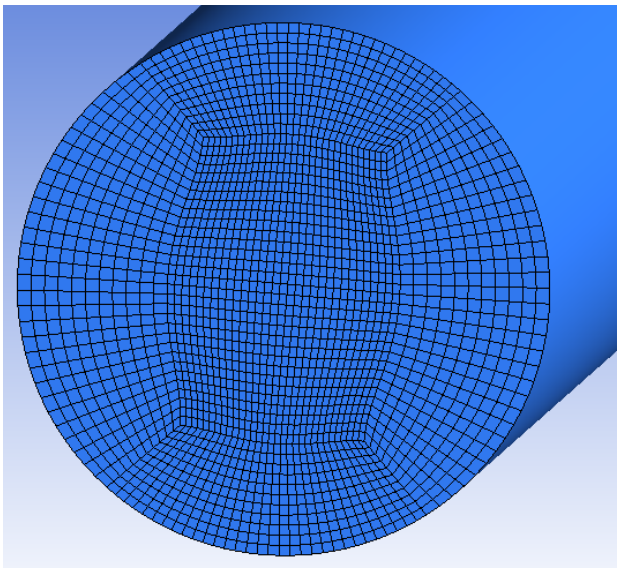

Figure 3.6: O-grid structure at the circular pipe's inlet plane

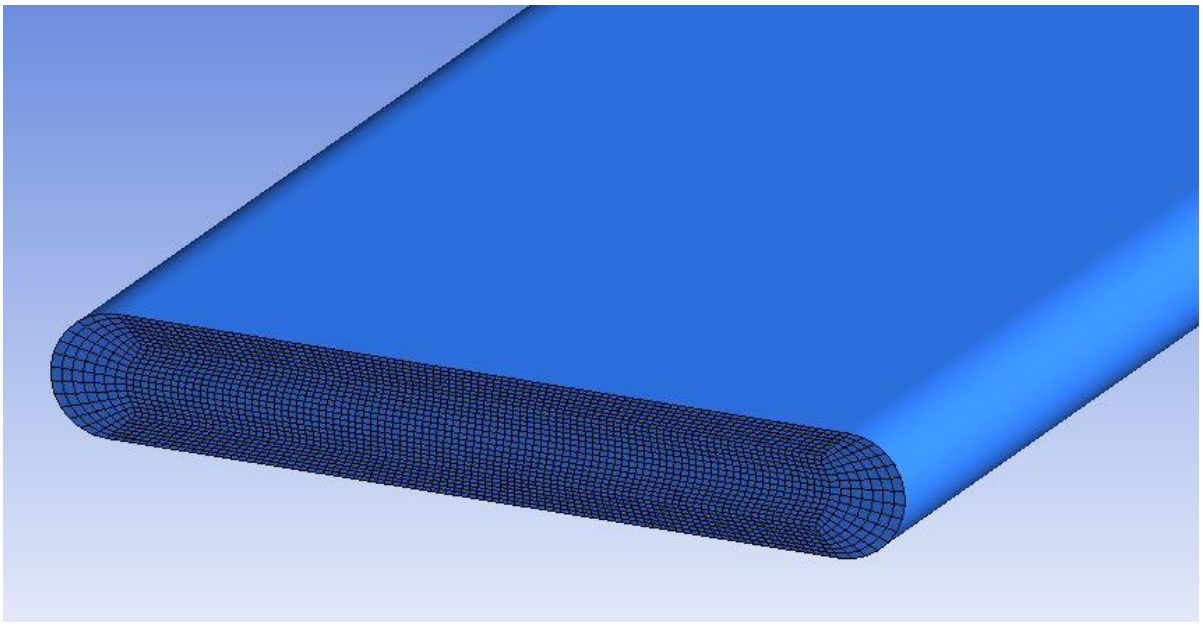

Figure 3.7: O-grid structure at the racetrack pipe's inlet plane

To model the viscous sub layer effectively, the near wall grid spacing was tuned to meet Y-plus requirement for each turbulence model. Y-plus is calculated based on Equation 3.1 [52]. Table 3.1 shows average Y-plus values at the coolant hole's downstream vicinity, *the test surface,* and the total number of grids elements for each studied turbulence model at M=1.

The reason for distinguishing *the test surface plane* from the remaining walls is clarified later in the "Boundary Conditions"; *section 3.4.2*.

$$Y^{+} = {\rho u_{\tau} y}/{\mu} \qquad (3.1)$$

Table 3.1: Y-plus values at the "test surface" and total number of grids elements for each studied turbulence model at M=1

Turbulence Model	Average Y-Plus at Test Surface	Total Number of Grid's Elements
Standard k-ε with scalable wall function	5	1.5 million
Realizable k-ε with scalable wall function	5	1.5 million
EARSM k-ε with scalable wall function	5	1.5 million
Yang-Shih k-ε	1	2.0 million
SST k-ω	1	2.0 million

Owing to the character of the adiabatic film effectiveness (ζ), defined by Equation 3.2, in indicating the film cooling performance, its values at the jet centerline (*because of lack of laterally averaged experimental data*) was nominated for the grids independency study and the numerical models validations

$$\zeta = \frac{T_{aw} - T_{\infty}}{T_c - T_{\infty}} \qquad (3.2)$$

The grid independency study was conducted by comparing the centerline adiabatic film effectiveness of consecutive refinements of the grid along all directions. A grid-independent solution was confirmed the instant where there is no substantial change in the centerline adiabatic film effectiveness values relative to the change in the grid size. An example of grid sensitivity analysis for *realizable k-ε model with scalable wall function* (the most suitable model, among the studied ones, that fits experimental centerline adiabatic film effectiveness

data at M=1) is presented in Figure 3.8. The figure reports that there is no significant change in centerline adiabatic film effectiveness values associated with successive grid refinements from 1.5, passing by 2.0, and ending with 3.2 million grid elements. Thus, the least grid size (1.5 million elements) was used for the mentioned turbulence model to compare it with the other selected models, which were subjected to similar grid analysis as well.

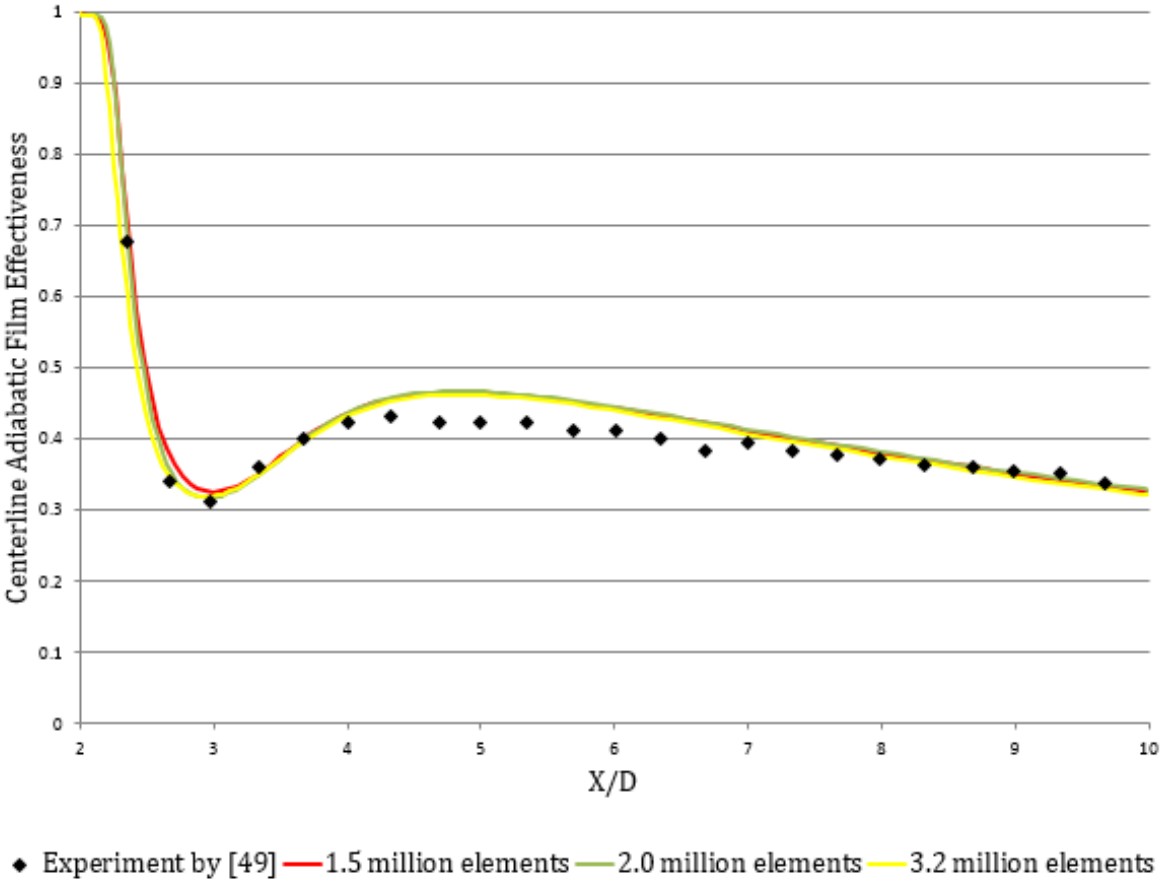

Figure 3.8: Grid independency study of realizable k-ε model with scalable wall function at M=1

3.4.2. Boundary Conditions

To attain the numerical solution, the boundary conditions listed in Table 3.2 were set to the boundaries shown in Figure 3.5. The working fluid for the whole domain is air with incompressible ideal gas properties. Additionally, viscous heating effect is enabled.

Turbulence length scale value of 3 mm, and 4% freestream turbulence intensity, which were calculated and measured by El-Gabry et al. [48], are defined as the turbulence parameters specifying the mainstream inlet conditions.

Starting from the coolant hole trailing edge towards the downstream direction, new boundary plane called "test surface" was identified as a medium for applying heat flux apart from the remaining adiabatic walls to simulate the non-adiabatic experimental setup illustrated in Figure 3.3.

Again; To save computational power, noticing the similarity, only one of the three holes was modeled, limiting the lateral domain extent to one pitch. The "symmetry", alternatively; "periodic", condition was applied to the domain side boundaries since they are the midway planes between two adjacent holes. Figure 3.1 illustrates the lateral extent of fixed pitch computational domain for both circular and racetrack hole shapes.

Table 3.2: Boundary conditions of the numerical models at M=1

Boundary	**Boundary Conditions**	
Mainstream inlet	Type	Velocity inlet
	Temperature	298.15 K
	Velocity magnitude	9.1 m /s
	Turbulence intensity	4 %
	Turbulence length scale	3 mm
Coolant inlet	Type	Velocity inlet
	Temperature	278.15 K
	Velocity magnitude	9.1 m /s
	Turbulence intensity	0 %
	Hydraulic diameter	19.05 mm

Boundary	**Boundary Conditions**	
Outlet	Type	Pressure outlet
	Gauge pressure	0 Pa
	Backflow total temperature	298.15 K
	Backflow Turbulence intensity	4 %
	Backflow turbulent viscosity ratio	10
Test surface	Type	Wall
	Wall motion	Stationary wall
	Shear condition	No slip
	Heat flux	0 for adiabatic model 2500 W/m^2 for non-adiabatic model
Walls	Type	Wall
	Wall motion	Stationary wall
	Shear condition	No slip
	Heat flux	0
Coolant wall	Type	Wall
	Wall motion	Stationary wall
	Shear condition	No slip
	Heat flux	0
Side boundaries (right & left)	Type	Symmetry

3.4.3. Numerical Turbulence Models

Aiming to find a numerical model with faithful simulation for film cooling associated phenomena at M=1, four numerical models were studied and compared to the experimental centerline adiabatic film effectiveness values reported by Thurman et al. [49]. The four chosen RANS-based turbulence models are: *Standard k-ε with scalable wall function*, *Realizable k-ε with scalable wall function*, *SST k-ω*, and *EARSM k-ε with scalable wall function*. The solver used with the *Realizable k-ε* model is *ANSYS Fluent release 16.1*, while *ANSYS CFX release 16.1* is used for the rest ones.

The reason for using scalable wall function with all chosen k-ε models is to, concurrently, maintain the feature of structured grid, and ensure as near-wall resolution as allowed by the k-ε model without erroneous implementation of the logarithmic wall law at the viscus sublayer throughout the studied surface. Maintaining a structured grid, along with meeting the model Y-plus requirement, becomes more challenging with flow separation that causes differentiated local fluid velocities. The scalable wall function limits the use of the logarithmic wall function to the point of intersection with linear sublayer formulation [53]. This also allowed to perform the grid independency studies without having the concern of model sensitivity to the near-wall grid. Utilizing the mesh sensitivity example illustrated in Figure 3.8 to clarify; All the grids approximately gave the same centerline adiabatic film effeteness curve although the average Y-plus of the coarsest grid is 5, while the value is 0.5 for the finest one.

Table 3.3 presents the solvers' given values for the different constants of the studied models. Due to their verified efficient performance, the default values were kept as it is. Other

constants that were not available to check via the solvers' user interfaces are not reported in this table.

Table 3.3: Numerical models' constants at M=1

Standard k-ε			
C_μ	$C_{2\epsilon}$	σ_k	σ_ϵ
0.09	1.92	1.0	1.3
Realizable k-ε			
$C_{2\epsilon}$	σ_k	σ_ϵ	
1.9	1.0	1.2	
SST k-ω			
β*	α	β	
0.09	0.553167	0.075	
EARSM k-ε			
C_μ	$C_{2\epsilon}$		
0.09	1.92		

Nevertheless, turbulent Prandtl number was changed from its default value, 0.9, for both *standard k-ε with sellable wall function* and *SST k-ω* models. It was set at 0.6 for the former and 0.7 for the latter; values which were found to give better agreement with the experimental centerline adiabatic film effectiveness data. Figure 3.9 shows the gradual decrease of turbulent Prandtl number until reaching the optimal value for the *standard k-ε model with scalable wall function*.

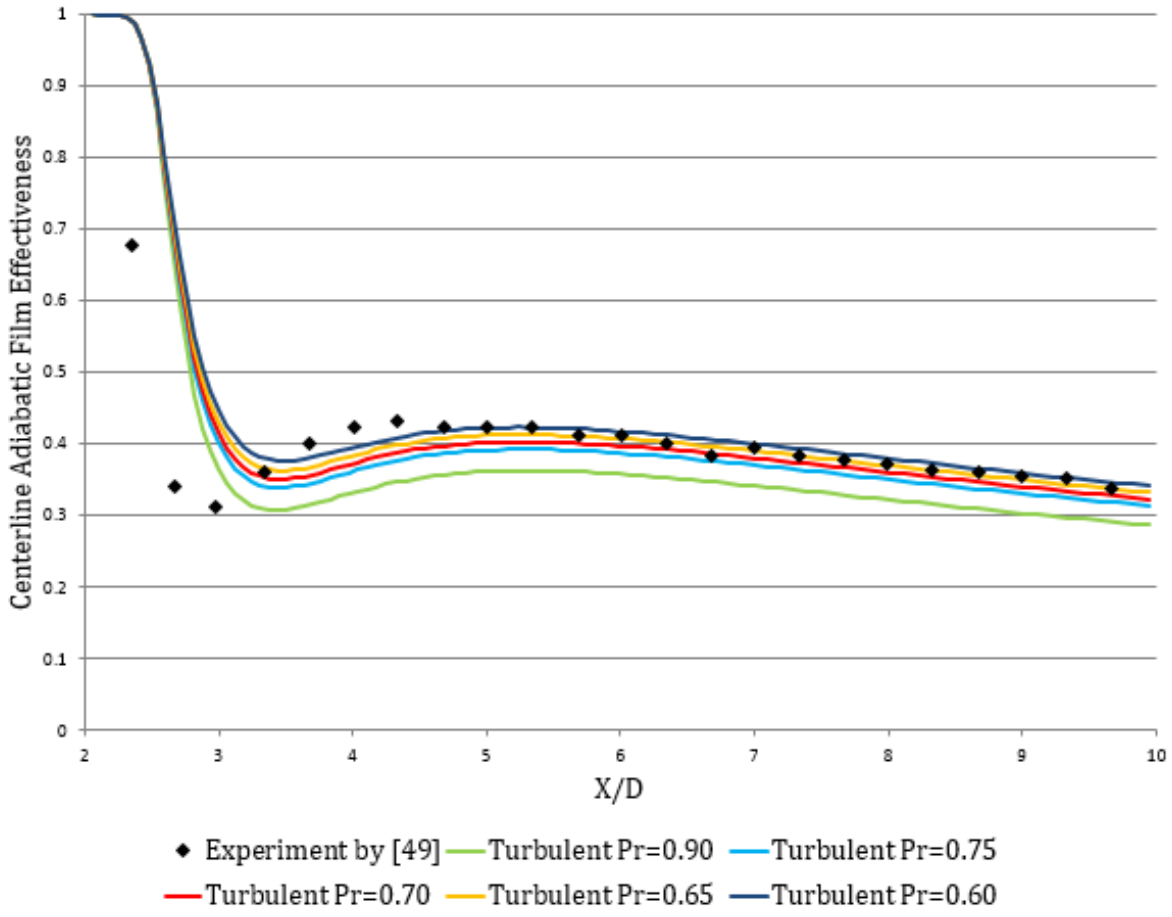

Figure 3.9: Effect of Pr_t on centerline adiabatic film effectiveness predictions for standard k-ε model with scalable wall function at M=1

The conclusion from Figure 3.9 agrees with the mathematical formulation that relates turbulent heat diffusivity (Γ_t) and turbulent Prandtl number (Pr_t); Equation 3.3. The decrease of turbulent Prandtl number increases the turbulent heat diffusivity, allowing for rapid jet diffusion towards the cooled surface, and hence increases the adiabatic film effectiveness.

$$\Gamma_t = {\mu_t}/{\rho Pr_t} \qquad (3.3)$$

The SIMPLEC (SIMPLE-Consistent); a pressure-based segregated algorithm, is used for pressure-velocity coupling. The second order scheme is used for the spatial discretization

of the pressure, while QUICK scheme is chosen for the convective terms; momentum, turbulent kinetic energy, turbulent dissipation rate and energy.

3.5. Numerical Modeling for the Case M=2

3.5.1. Mesh Generation

The same meshing technique and grid independency considerations that were described for the case M=1 in *section 3.4.1* are applied to the case M=2 as well. The only difference is the statistics of the grids as presented in Table 3.4.

Table 3.4: Y-plus values at the "test surface" and total number of grids elements for each studied turbulence model at M=2

Turbulence Model	Average Y-Plus at Test Surface	Total Number of Grid's Elements
Realizable k-ε with scalable wall function	5	1.5 million
Realizable k-ε with enhanced wall treatment	1	2.0 million
SST k-ω	1	2.0 million

3.5.2. Boundary Conditions

The same boundary conditions that were described for the case M=1 in *section 3.4.2* are applied to the case M=2 as well. The only exception is the coolant inlet velocity magnitude which was set at 18.2 m/s to account for the new blowing ratio.

3.5.3. Numerical Turbulence Models

Guided by the validation results from the numerical modeling case of M=1, three numerical models were studied and compared to the experimental centerline adiabatic film effectiveness values at M=2 reported by Thurman et al. [49]. The three chosen RANS-based turbulence models are: *Realizable k-ε with scalable wall function, Realizable k-ε with*

enhanced wall treatment, and *SST k-ω*. The solver used with the *Realizable k-ε* models is *ANSYS Fluent release 16.1*, while *ANSYS CFX release 16.1* is used for the *SST k-ω* one.

The reason for testing the *enhanced wall treatment* approach with the *realizable k-e* model that it gave, to some extent, good agreement with experimental heat transfer coefficient data at M=1. However, its adiabatic film effectiveness prediction was not promising; hence, it has not been included among the presented results for the case M=1 in Table 3.1. *Enhanced wall treatment* is a near-wall modeling method that combines a two-layer model with enhanced wall functions to overcome the lack predictions of the model at near-to-wall unsatisfactory resolved regions. [52]

Table 3.5 presents the solvers' given values for different constants of the studied models that were also kept as it is due to its verified efficient performance in literature. Nevertheless, only for *SST k-ω* model, turbulent Prandtl number was changed from 0.9 (its default value) to 0.7 (as for the case of M=1), trying to achieve better agreement with the experimental centerline adiabatic film effectiveness.

Table 3.5: Numerical models' constants at M=2

Realizable k-ε		
$C_{2\ \epsilon}$	σ_k	σ_ϵ
1.9	1.0	1.2
SST k-ω		
β*	α	β
0.09	0.553167	0.075

As for the M=1; SIMPLEC algorithm is used to couple pressure and velocity, second order scheme is used for the spatial discretization of the pressure, and QUICK scheme is used for the spatial discretization of the convective terms.

3.6. Irregular Pipe Geometry Optimization Using the Adjoint Solver for the Case M=1

In order to step forward from the optimum hole shape that have a restriction of maintaining specific geometry feature (the racetrack) to free irregular shape optimization, *ANSYS Fluent Adjoint solver* with discrete adjoint approach has been utilized. This section describes the procedures followed and the settings applied to the Adjoint solver for the case M=1.

3.6.1. Overview, Assumptions, and Implementation Procedures of the Adjoint Solver

The Adjoint solver simultaneously calculates the derivatives of a specified solution variable with respect to the input parameters; the boundary conditions and the geometry in terms of surface mesh nodes coordinates. These derivatives assume first order flow sensitivity to the change of each input parameter [54]. Once the solver calculated the sensitivity fields, the design change constraints should be defined and the desired change in the specified solution variable of interest should be quantified. The constrained change in the selected input parameter (most importantly, the shape of appointed geometry parts) can be calculated using the quantified objective change in the solution variable of interest along with its sensitivity field to the chosen input parameter. Nevertheless, geometry is not a single parameter, it is rather a combination of surface mesh nodes coordinates in the appointed geometry parts. Thus, modifying the position of these mesh nodes to satisfy the desired objective change is not straight forward, and the need for powerful optimization technique arises. It was found that making changes to the surfaces proportional to their local sensitivity data is an effective methodology since small changes will have a large effect on the solution variable of interest. This principle represents the basis of the design optimization technique called simple gradient algorithm. [54]

Adjoint solver feature of limiting the changes that arise in the flow variables with respect to these of input parameters to linear correlations produces a direct relationship between the input parameters and the solution variable of interest. Hence, the adjoint solution is specific to the current flow state [54], which adds more deteriorating factor to the accuracy of predictions. Clearly, the larger the change targeted, the more important the nonlinearity impacts. As a result, the less accurate the predictions become.

Adjoint solver assumes either laminar or turbulent, steady incompressible single-phase flow in an inertial frame of reference [54]. The assumptions are compatible with the conditions of the flow under investigation, so the accuracy of the adjoint calculations will not be affected by them. For turbulent flow, however, standard wall functions are employed on all walls and a frozen turbulence is assumed, in which the effect of changes to the state of the turbulence is not taken into account when computing sensitivities. [54]

The Adjoint solver is typically used in an iterative way as illustrated in Figure 3.10. The original shape with solved flow state is subjected to **adjoint operations** to produce new geometry (mesh) that is, in turn, subjected to flow solution process. This concludes one complete cycle of the iterations that may be repeated based on the output evaluation. The **adjoint operations** involve:

1- defining the solution observable of interest and the solver settings,
2- running the Adjoint solver for the observable/flow-condition combination to produce the sensitivity field,
3- specifying the shape modification constraints and quantifying the objective change in the observable of interest,
4- computing the optimum shape modification, and
5- morphing from old into new mesh.

More details about the implementation of these procedures are available in the following sections.

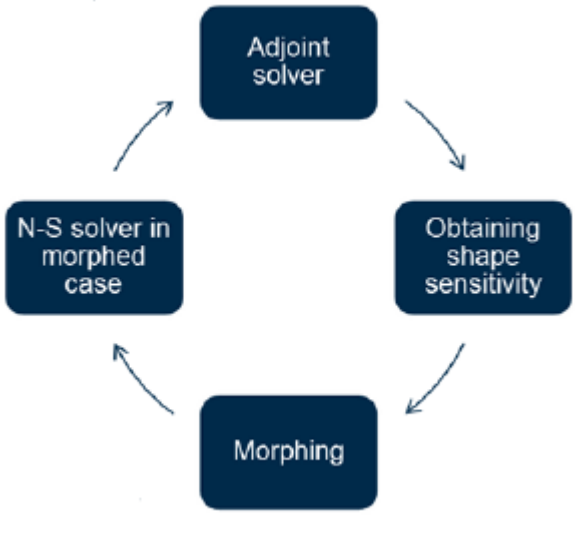

Figure 3.10: One Cycle of Iterations using the Adjoint solver [55]

3.6.2. Defining the Solution Observable of Interest

Area-weighted average temperature over the test surface was chosen as the solution variable of interest that the Adjoint solver, based on the current flow state, will calculates its derivative with respect to the geometry and the boundary conditions. The objective function is to minimize the area-weighted average test surface temperature defined by Equation 3.4.

$$T_{av} = \frac{\Sigma_f |A_f| T_f}{\Sigma_f |A_f|} \qquad (3.4)$$

3.6.3. Defining the Adjoint Solver Settings

Solution Schemes

Using the same solution schemes for both the adjoint and the flow solutions gives the most accurate converged adjoint results, while using dissimilar schemes affects, but does not

deteriorate, the derivatives' calculations [54]. However, the second order and QUICK spatial discretization schemes, that were respectively used for the of pressure and momentum solution of the flow, are not available for the Adjoint solver. Instead, standard and First Order Upwind schemes are used for the adjoint calculations of pressure and momentum respectively. Moreover, Solving the energy equation was enabled during the adjoint calculations in order to calculate the temperature sensitivity field.

Solution Initialization and Advancement Controls

By default, the Adjoint solver is initialized by values computed from the state of the flow solution. Nevertheless, initialization sets the value of the adjoint velocity (the vector of weights associated with the components of the residual of the momentum equation in each cell) and the adjoint pressure (the adjoint value associated with the residual of the continuity equation) to zero everywhere in the problem domain. Solver settings is, then, automatically adjusted based on the trends observed as the calculations advance to encourage convergence [54]. Figure 3.11 shows an example of solution-based advancement control parameters (Courant number, artificial compressibility, flow rate Courant scale, and energy equation scaling) values at the end of the first adjoint calculations attempt. The values have been gradually modified, based on solution trends, from the default values (0.1 for the artificial compressibility, and 1 for the rest parameters). The figure reveals the incompressible flow condition by implementing low artificial compressibility effect to the adjoint continuity equation. Moreover, the low values of both flow rate Courant scale and energy equation scaling reveals the instability encountered by the solver throughout the adjoint calculations [54]. The reason and the applied solution to deal with these encountered instabilities are discussed hereafter.

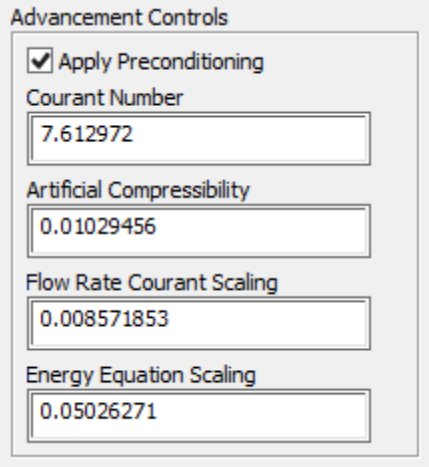

Figure 3.11: Adjoint advancement control parameters values at the end of, and based on, first step adjoint calculations

Stabilization Scheme

Large cell counts, complex geometry, high Reynolds number, small scale unsteadiness, and strong shear; all these factors increase the opportunity that adjoint solution will encounter instability issues. Despite the spatial localization of these instabilities, the linearity of the adjoint problem provides no intrinsic limit on their growth during the solution advancement. A stabilized solution scheme will be required to obtain adjoint solutions for problems. [54]

Being the least resource-intensive stabilization scheme among these available in the Adjoint solver interface [54], dissipation scheme was utilized to damp the growth of expected instabilities. It provides stabilization for the solution advancement of the adjoint calculations by introducing nonlinear damping strategically into the calculation domain. The strategy is to trace a marker based on the state of the adjoint solution, then apply damping only to regions where large markers is observed. [54]

Under-Relaxation Factors

Under-relaxation factors for the adjoint momentum, continuity, local flow rate, and energy were set to 0.6 reflecting low, but less aggressive, solution advancement. The factors were, then, increased when calculations became stable to accelerate the convergence.

3.6.4. Specifying the Shape Modification Constraints

Figure 3.12 is an example of the Cartesian box that was used in order to bound the mesh modification. Any node lies outside the bounding box is not allowed to move. Excluding the inlet section of the coolant pipe ensures constant inlet cross-sectional area that is, along with using the same inlet velocity and temperature, guarantees similar mass flux for all modified and original geometries. On the other hand, enlarging the bounding box beyond the coolant pipe boundaries was essential to allow for free shape modification for the exit hole, and to avoid severe cells' skewness at the interface between the coolant pipe and the flat plate surfaces. Furthermore, second order continuity, a continuous second derivative, of mesh morphing between movable and unmovable walls was set, resulting in smoother mesh transition at these regions. However, the movement of the mesh nodes in Y-direction was disabled to prevent any modification in the flat plate surface topology. Moreover, symmetry plane [Y=0] was defined as a constraint for the mesh morphing process.

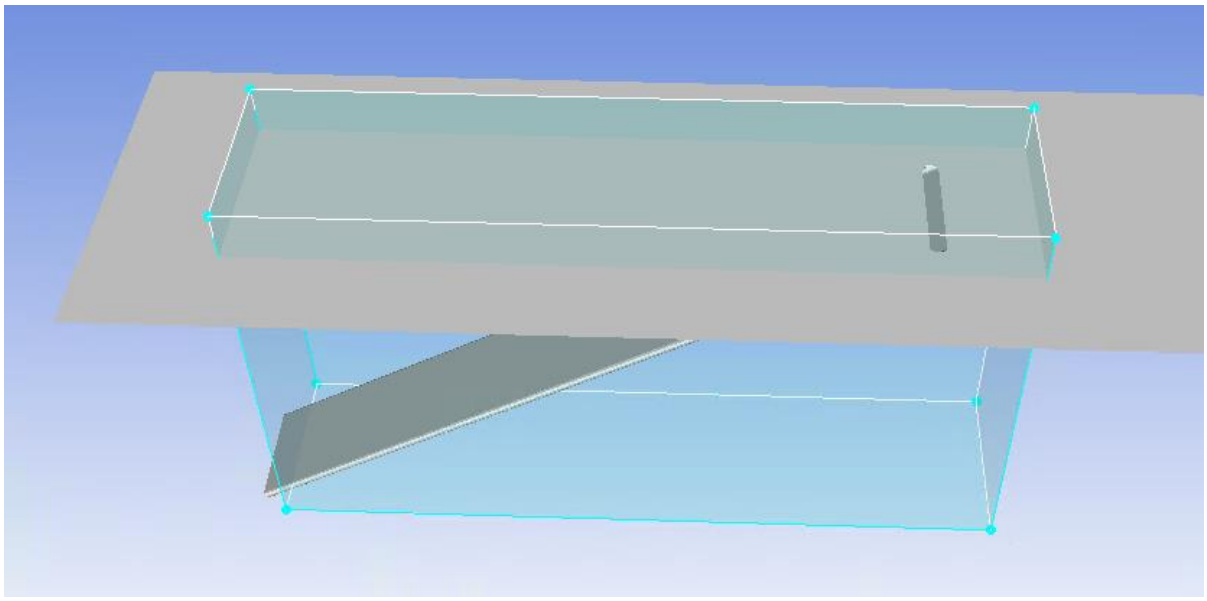

Figure 3.12: An example for mesh modification boundary

The motion of the mesh nodes inside the prescribed bounding box is depending on the movement of control points [54]. The number of these control points in each coordinate direction within the prescribed moving bounding box is specified. The control points are distributed evenly in each coordinate direction. The spacing between the control points defines the characteristic spatial scale for the morphing operation [54]. Based on practice, twenty control points were applied in each coordinate direction and resulted in smoother mesh morphing operations for the three shape modification steps.

3.6.5. Quantifying the Objective

In order to compute the optimum shape modification, the objective change of the predefined observable of interest, the area-weighted average test surface temperature, needs to be quantified. Large objective change should be avoided for two essential cautions: undesired mesh distortion, and overstepping the local minimum surface temperature [54]. Exceeding the local optimum value by setting an overoptimistic objective is a probable consequence of an intrinsic feature of the Adjoint solver; the first order flow sensitivity fields' calculations. For

the current study, minimizing the temperature by 1% was tested and found to be the suitable objective for the first two geometry modification steps. For the third step, the objective is reduced to 0.5% temperature minimization to avoid mesh distortion. However, the analysis over the whole test surface showed null cooling improvement when morphing from the second modified shape to the third modified one. Hence, no further adjoint operation was performed.

3.6.6. Shape Modification

The Adjoint solver's design tool was utilized to compute the optimum mesh deformation satisfying the predefined objective and constraints based on the calculated sensitivity field.

The next step is solving the flow of the modified geometry using Fluent solver, then exporting the temperature data over the test surface to evaluate the actual enhancement and test the adequacy of the new geometry for another optimization cycle.

4. RESULTS AND DISCUSSIONS

4.1. RANS Model Validation for the Case M=1

The validation exercise served the purpose of determining the numerical parameters that suitably predict the film cooling effectiveness and associated heat transfer. The parameters include the mesh size and construction, the definition of the boundary conditions, and the choice of the turbulence model along with suitable quantification of its constants.

A comparison between the four chosen turbulence models to validate them using the experimental centerline adiabatic film effectiveness readings at blowing ratio 1 is shown in Figure 4.1. Although the slight over-prediction in the downstream region from X/D=4 to X/D=7, the figure illustrates the superiority of realizable k-ε model with scalable wall function among the other ones in predicting the actual adiabatic film effectiveness values along the jet centerline. Consequently, the model has been selected to analyze and compare the performance of different geometries henceforth.

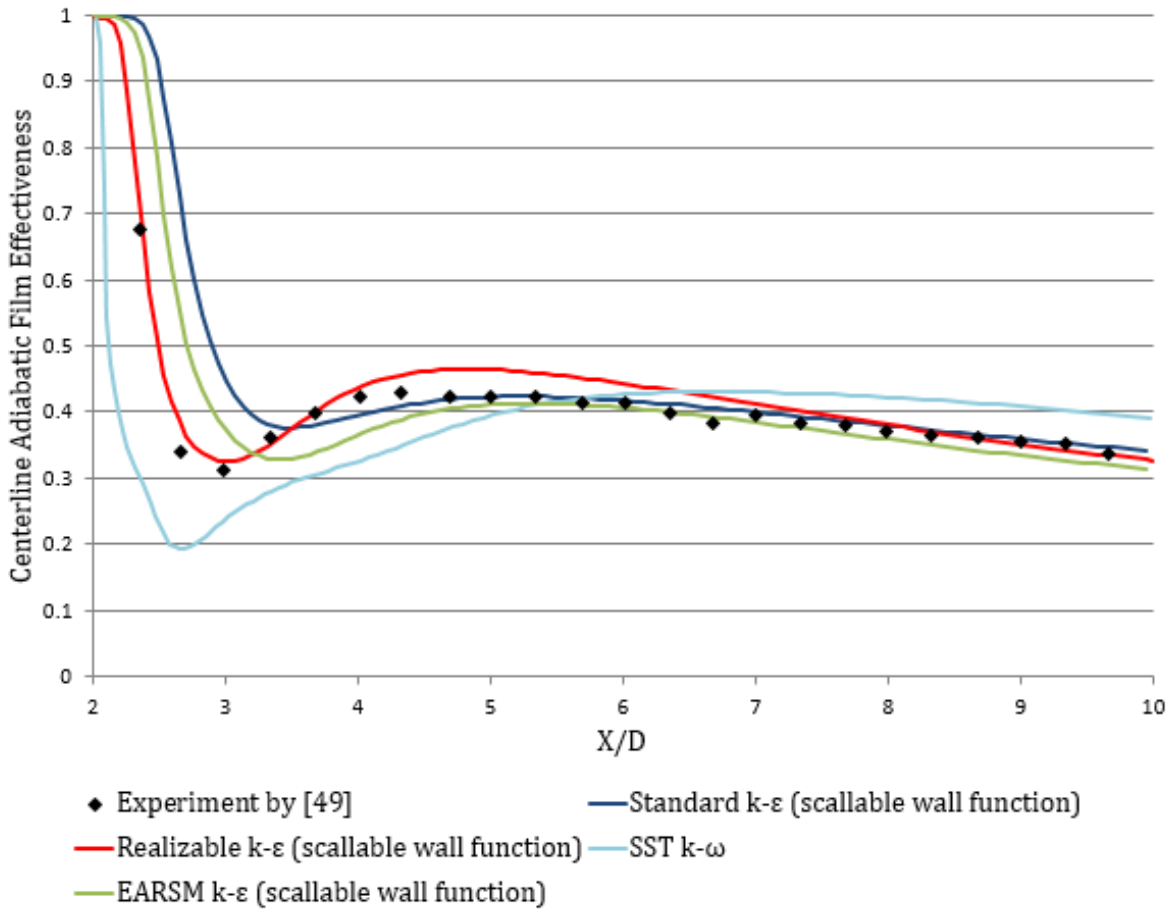

Figure 4.1: Validation of numerical codes for M=1

Realizable *k-ε* was first proposed by Shih et al. [56] in 1994 as an attempt to enhance numerical predictions for a variety of flow regimes. The model is distinguished from standard and RNG-based *k-ε* models by two characteristics: the dissipation rate equation and the eddy viscosity formulation. As described by Shih et al. [56], "*The new [then] model dissipation rate equation is based on the dynamic equation of the mean-square vorticity fluctuation at large turbulent Reynolds number. The new [then] eddy viscosity formulation is based on the realizability constraints; the positivity of normal Reynolds stresses and Schwarz' inequality for turbulent shear stresses*". As same as standard and RNG-based *k-ε* models, the eddy viscosity (μ_t) is defined by Equation 4.1, but the realizability constraints are guaranteed for the

realizable *k-ε* model by setting variable, instead of constant, $C\mu$ which is sensitive to the mean flow deformation and the turbulence fields (*k* and *ε*). [56, 52]

$$\mu_t = \rho C_\mu \, {k^2}/{\epsilon} \qquad (4.1)$$

After showing the superiority of the realizable k-ε model with scalable wall function in predicting the adiabatic film effectiveness values along the jet centerline, it is still important to test its accuracy in predicting the velocity and the temperature fields, and the heat transfer coefficient at the jet downstream region as well.

A comparison between experimental and numerical normalized U-velocity contours (U^*), defined by Equation 4.2, along the jet centerline is shown in Figure 4.2. Realizable k-ε model with scalable wall function closely predicts the normalized U-velocity contours; with slight underestimation near to the cooled surface. The worst estimation lies near to the hole exit; from X/D=2 till X/D=4.

$$U^* = {U}/{U_\infty} \qquad (4.2)$$

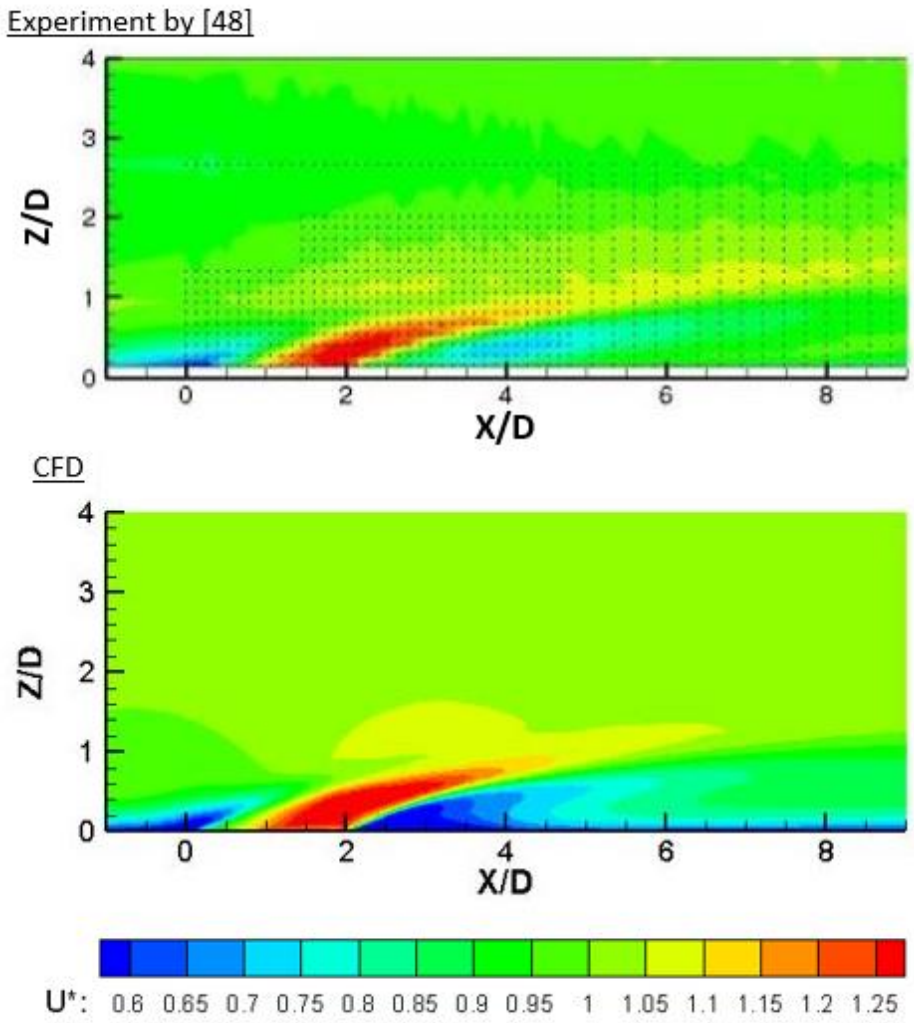

Figure 4.2: Normalized U-velocity validation along jet centerline at M=1

Realizable *k-ε* model with scalable wall function seams to predict the normalized temperature (θ), defined by Equation 4.3, to a far extent as shown in Figure 4.3. Nevertheless, the jet appears to sustain longer before suffering from thermal diffusion.

$$\theta = \frac{T - T_\infty}{T_c - T_\infty} \qquad (4.3)$$

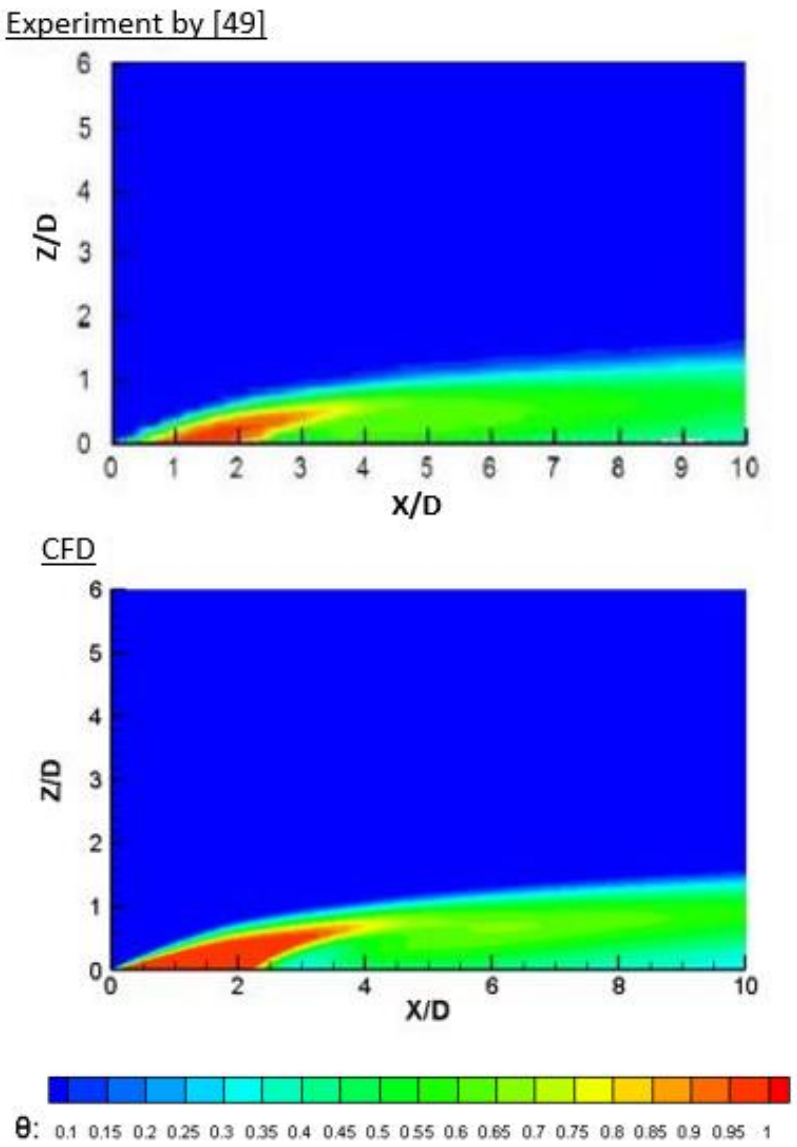

Figure 4.3: Normalized temperature validation along jet centerline at M=1

The convective heat transfer coefficient (h) is an important indicator for the heat transfer. For a constant heat flux (q) applied to the test surface, and given recovery temperature (T_{rec}); the convective heat transfer coefficient is related to the surface temperature (T_{sur}) by Equation 4.4. The recovery temperature is defined by Equation 4.5. Where the recovery factor (r) and the Prandtl number (Pr) are calculated by Equation 4.6 and Equation 4.7 respectively.

$$h = q/(T_{sur} - T_{rec}) \quad (4.4)$$

$$T_{rec} = T_{rec} + r\,(T_{total} - T_{static}) \quad (4.5)$$

$$r = Pr^{1/3} \quad (4.6)$$

$$Pr = C_p\,\mu/\lambda \quad (4.7)$$

Nusselt number (*Nu*), defined by Equation 4.8, is utilized to generalize the heat transfer indications. Fixing suitable characteristic length (the coolant pipe diameter; *D*) and assuming constant thermal conductivity (λ), Nusselt number directly quantifies the convective heat transfer coefficient. Accordingly, it quantifies the surface temperature for constant surface heat flux and given recovery temperature.

$$Nu = h\,D/\lambda \quad (4.8)$$

Despite of computing less lateral spread, the realizable *k-ε* model with scalable wall function predicts the overall level of Nusselt number contours qualitatively as illustrated in Figure 4.4. However, the numerical model gives the same degeneration trend captured by the experimental measures toward the downstream direction.

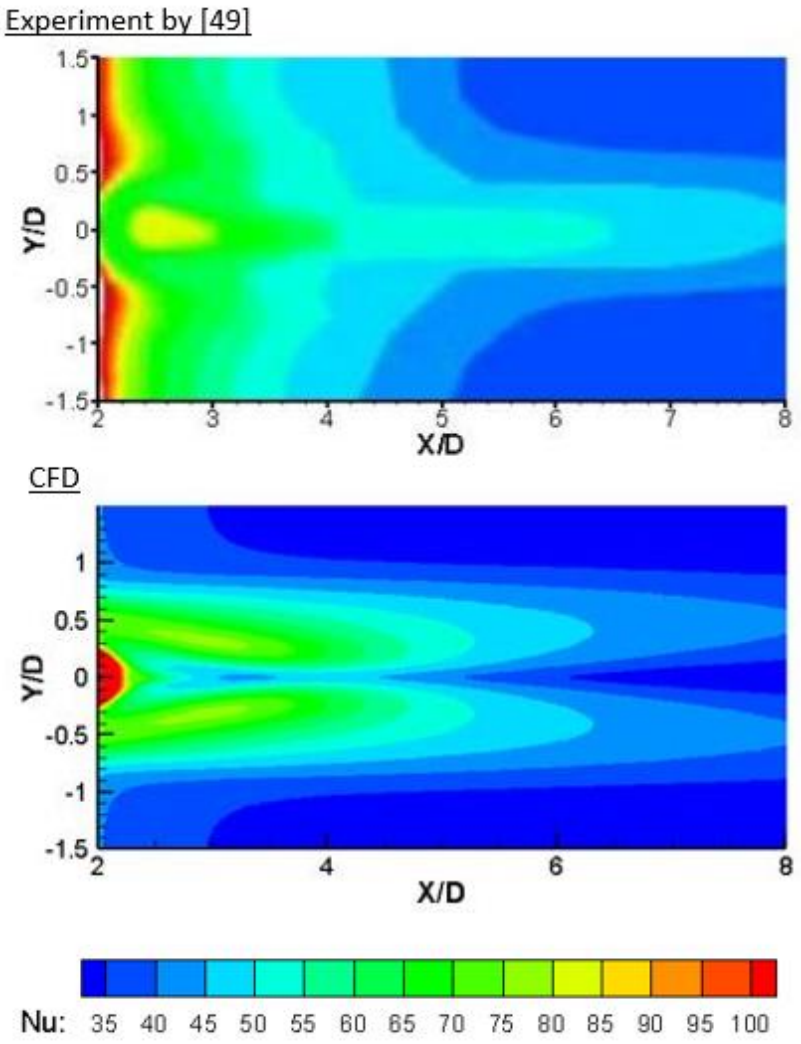

Figure 4.4: Nu number validation on test surface at M=1

4.2. Deficiency of RANS Models Predictions at M=2

A comparison between the three chosen turbulence models to validate them using the experimental centerline adiabatic film effectiveness readings at blowing ratio 2 is shown in Figure 4.5. All tested models underpredict the adiabatic film effectiveness, falling rapidly and diverging from the measured values. Although the predictions of the *realizable k-ε model with enhanced wall treatment* sustain for a slightly longer downstream distance when compared to the other tested models, its computed adiabatic film effectiveness values fall down quickly,

giving as less as half of that of the experimental data before reaching the downstream distance X/D=5.

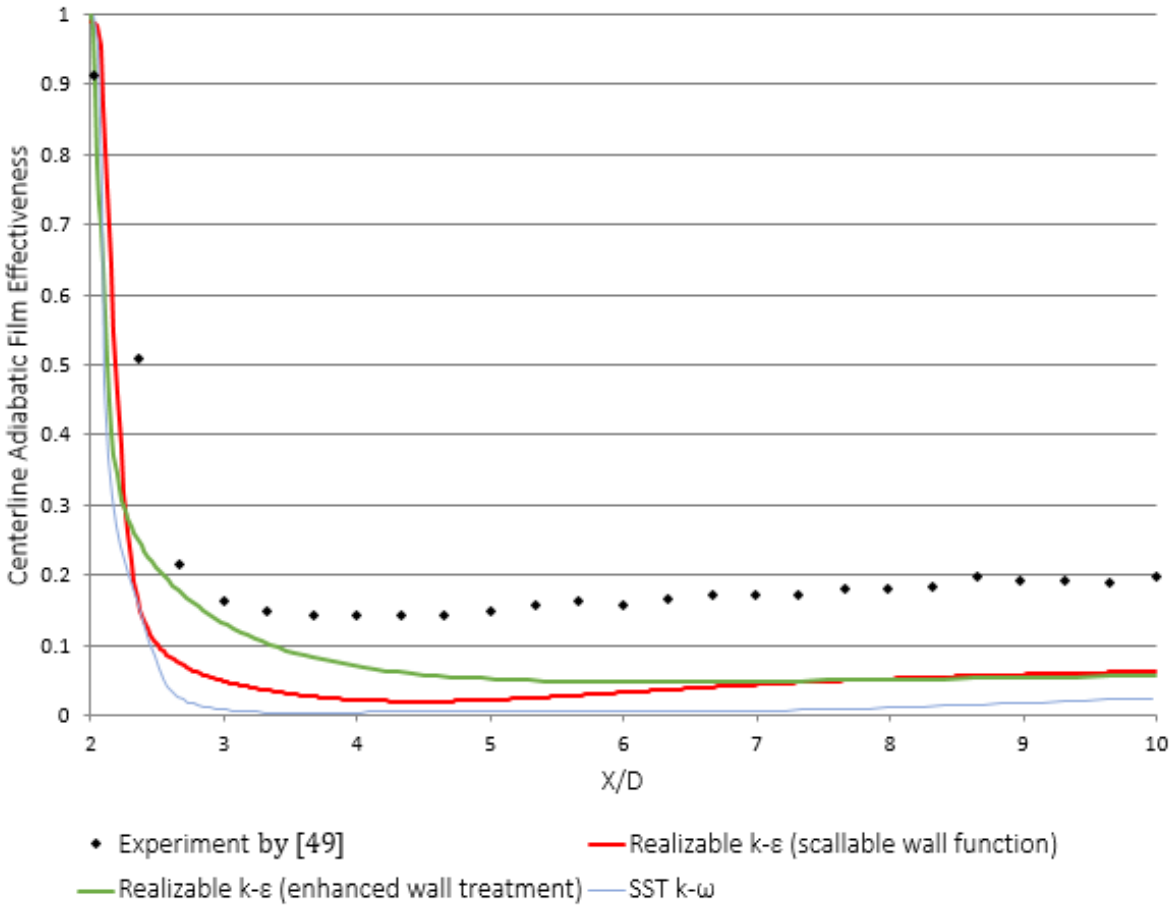

Figure 4.5: Validation of numerical codes for M=2

However, the inaccuracy of RANS models to predict the film cooling behavior at high blowing ratios is well known among the film cooling community. The reason is the lack of the isotropic models to simulate the complex turbulent features associated with the significant jet separation that happens at high blowing ratios. Accordingly, the remaining part of the current study (the comparison and the optimization of the coolant pipe geometry) is limited to the blowing ratio 1 only.

4.3. Comparison between the Circular and the Racetrack Cooling Holes at M=1

The film cooling performance, in terms of both the centerline and laterally averaged adiabatic film effectiveness, of the racetrack slot having an aspect ratio s/b=3 was tested and compared to that of the circular hole having the same flow area and pitch-to-width ratio p/w=3. The comparison in Figure 4.6 shows a remarkably higher and sustained centerline adiabatic film effectiveness for the racetrack slot than that for the circular hole. Furthermore, the laterally averaged adiabatic film effectiveness results, presented in Figure 4.7, demonstrate the superiority of the racetrack slot over the circular hole; not only along the jet centerline, but also over the lateral extent of the test surface. Nevertheless, the difference between the laterally averaged curves is less than that between the centerline ones, and gradually converging towards the downstream direction. At the downstream location X/D=10, the racetrack slot's centerline and laterally averaged adiabatic film effectiveness values are, respectively, about three and two times higher than those of the circular hole.

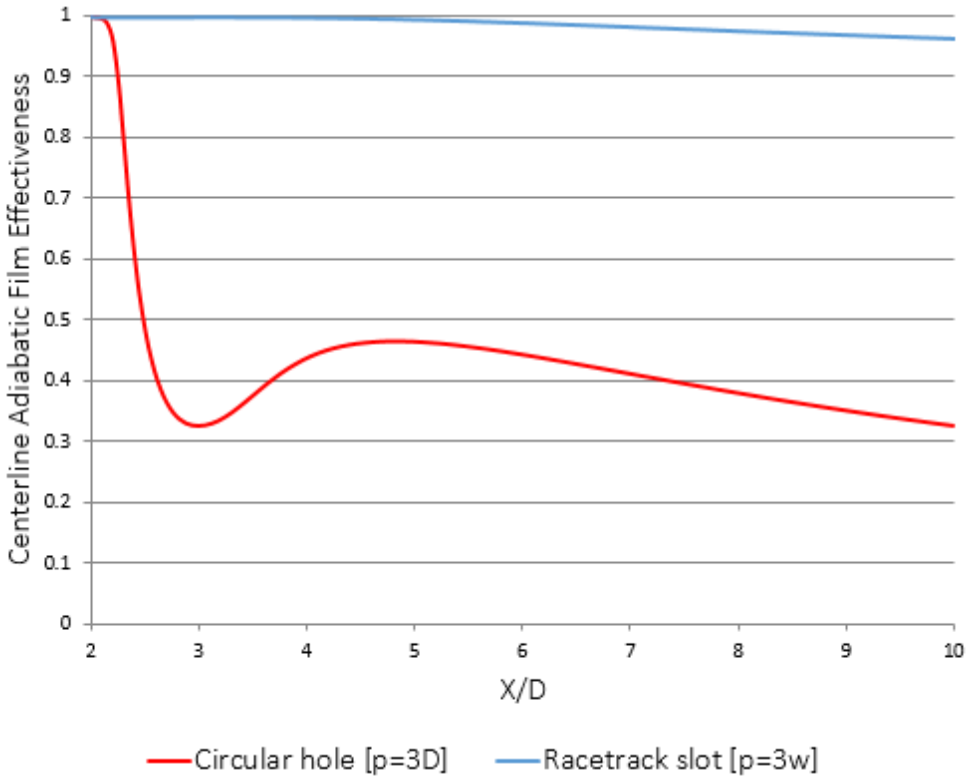

Figure 4.6: Centerline adiabatic film effectiveness for the circular hole and the racetrack slot; having the same p/w=3, and s/b=3; at M=1

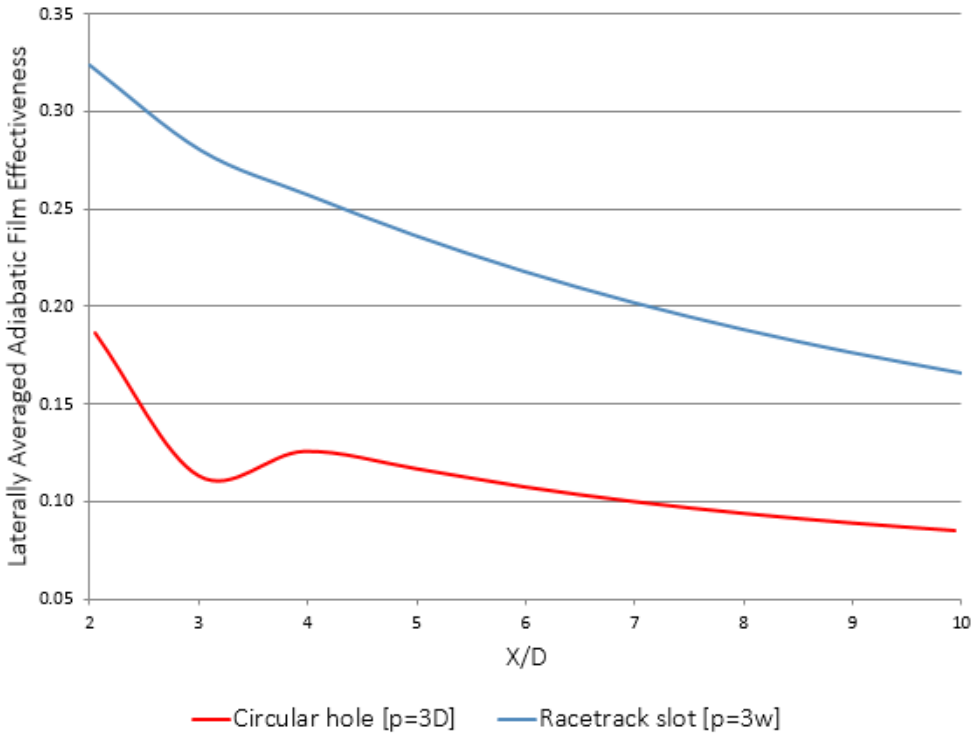

Figure 4.7: Laterally averaged adiabatic film effectiveness for the circular hole and the racetrack slot; having the same p/w=3, and s/b=3; at M=1

4.4. Optimization of the Racetrack Aspect Ratio for M=1

For the aim of optimizing the racetrack slot geometry to give its highest possible film cooling performance, after verifying its superiority over the circular hole, the research is directed towards altering a characteristic geometry parameter of the racetrack slot; **the aspect ratio**. Accordingly, the racetrack aspect ratio was stepwise changed from 2.5 to 8. The optimization is performed in terms of adiabatic film effeteness curves, and Nusselt number contours.

4.4.1. Identifying the Optimum Racetrack Aspect Ratio

Starting from the value of 2.5, increasing the aspect ratio progressively to 8 drove down the centerline adiabatic film effectiveness from 0.97 to 0.83 at the cross-flow plane X/D=10,

as shown in Figure 4.8, expressing the influence of the racetrack aspect ratio on the film cooling performance.

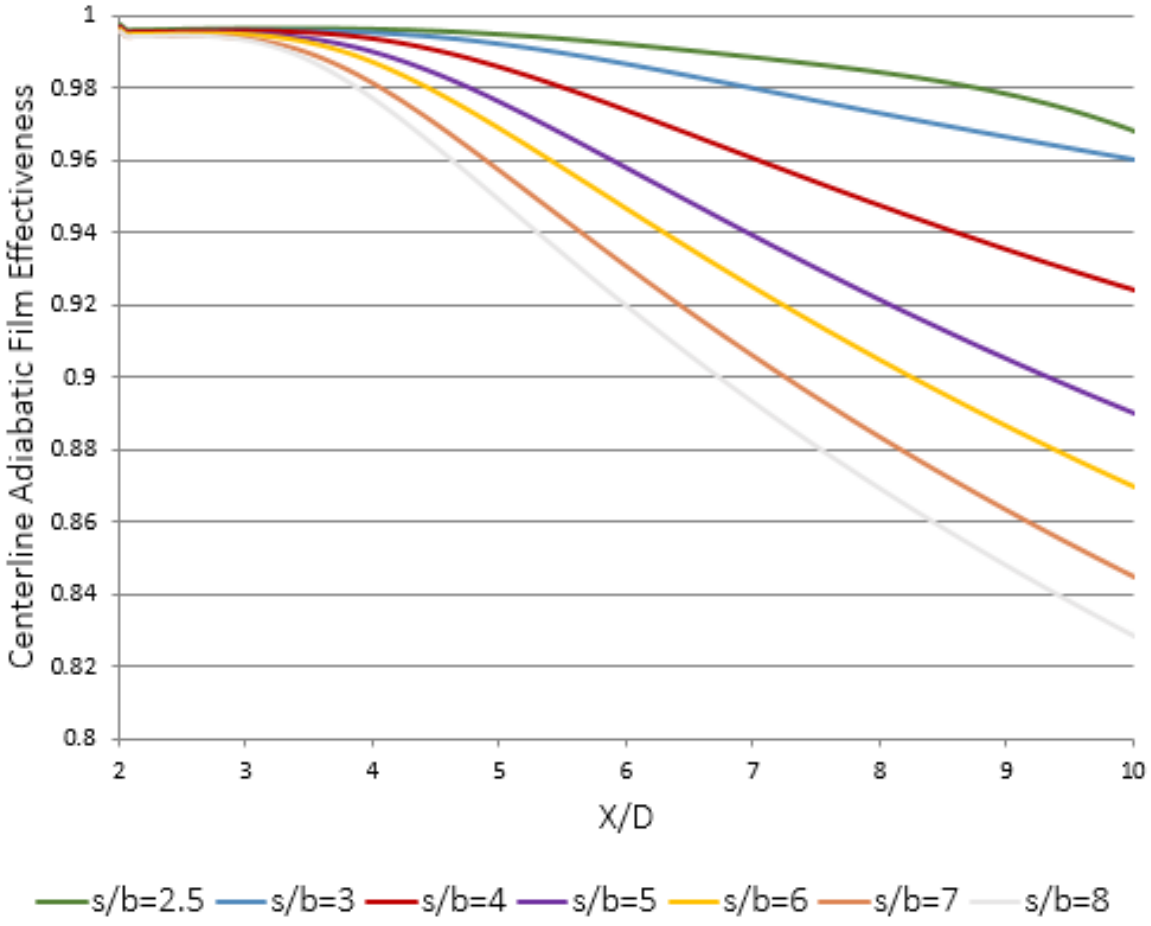

Figure 4.8: Centerline adiabatic film effectiveness comparison between racetrack slots; having p/w=3, and s/b=2.5, 3, 4, 5, 6, 7 & 8; at M=1

Nonetheless, the conclusion cannot be deduced exclusively from the centerline indicators because it only refers to a certain narrow, although important, area within the cooled surface. A more general indicative quantity, *the laterally averaged adiabatic film effectiveness*, responds to the change of the aspect ratio in an opposite way to what the centerline one does, as demonstrated in Figure 4.9. The increase of the laterally averaged adiabatic film effectiveness with the aspect ratio becomes more significant toward the downstream direction, where more time for mixing and thermal dissipation is available. In figures, increasing the

aspect ratio stepwise from 2.5 to 8 (or 7) drove up the laterally averaged adiabatic film effectiveness by a noticeable factor of 1.4, *from 0.15 to 0.21*, at the cross-flow plane X/D=10.

Further discussion to analyze the opposite trend of the two adiabatic film effectiveness indicators is postponed to the end of the current section after designating the optimum aspect ratio. However, the laterally averaged adiabatic film effectiveness curves nominate 7 or 8 to be the optimum racetrack aspect ratios, with slight preference for the former over the latter at the near downstream vicinity of coolant hole exit; X/D=2~3.

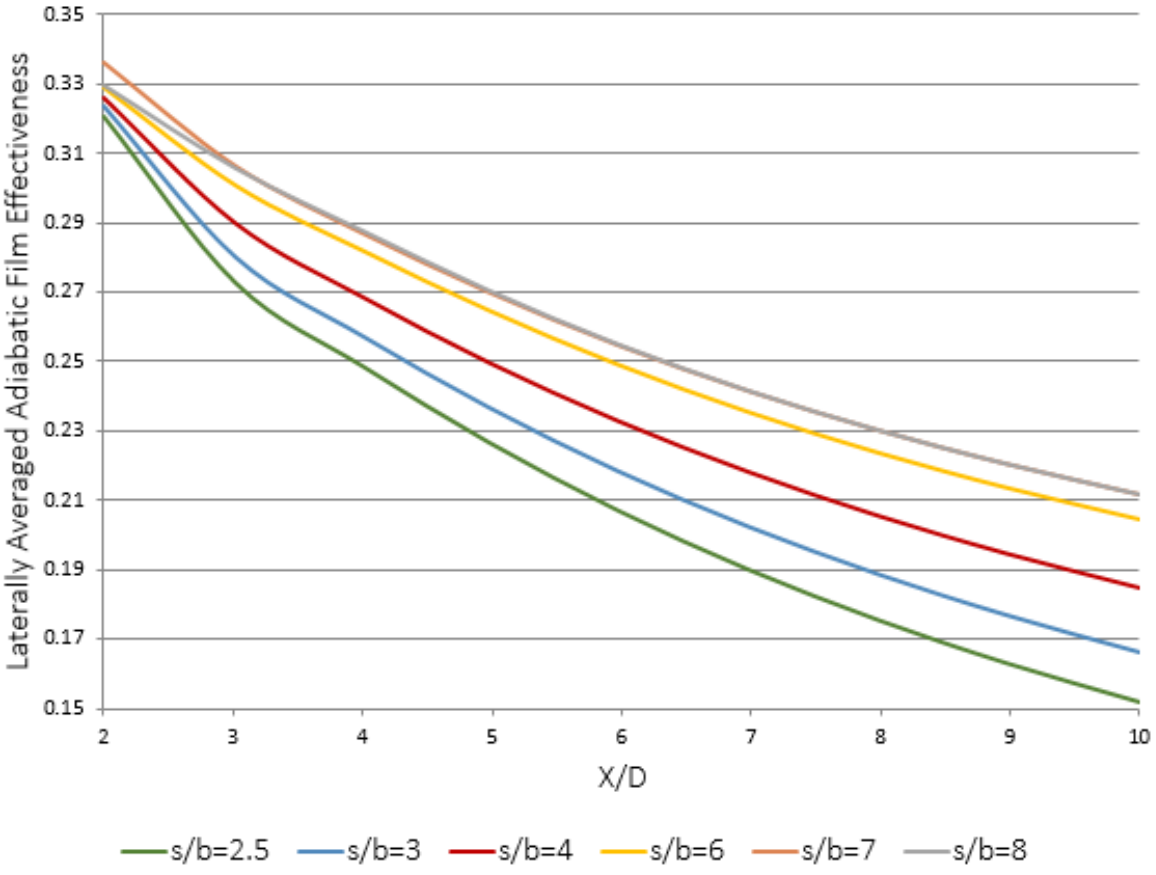

Figure 4.9: Laterally averaged adiabatic film effectiveness comparison between racetrack slots; having p/w=3, and s/b=2.5, 3, 4, 6, 7 & 8; at M=1

Assuming constant thermal conductivity, it can be simply concluded from the set of Equations (4.4 ~ 4.8) that increased Nusselt number implies increased heat transfer coefficient,

and reduced temperature difference between the heated surface ant the freestream air; That is, for a unit temperature difference between the surface and freestream, more heat is transferred from the surface due to the coolant film effect.

Nusselt number distributions over the heated surface for different investigated racetracks' aspect ratios are compared in Figure 4.10. Increasing the aspect ratio from 2.5 to 5 extended the cooling effect to a longer downstream distance. Nevertheless, the improvement is localized to the jet centerline. Further increase in the aspect ratio from 5 to 8 yields further shrinkage in the cooling effect along the jet centerline.

Once more, the area of interest is not limited to the jet centerline. A comparison over the entire heated surface shows that the heat transfer is improved by either increasing or decreasing the aspect ratio from 5 on the ways to its borderlines; 2.5 and 8. Furthermore, the enhancement toward the increased aspect ratio is better than that toward the opposite direction in terms of the cooling effect uniformity.

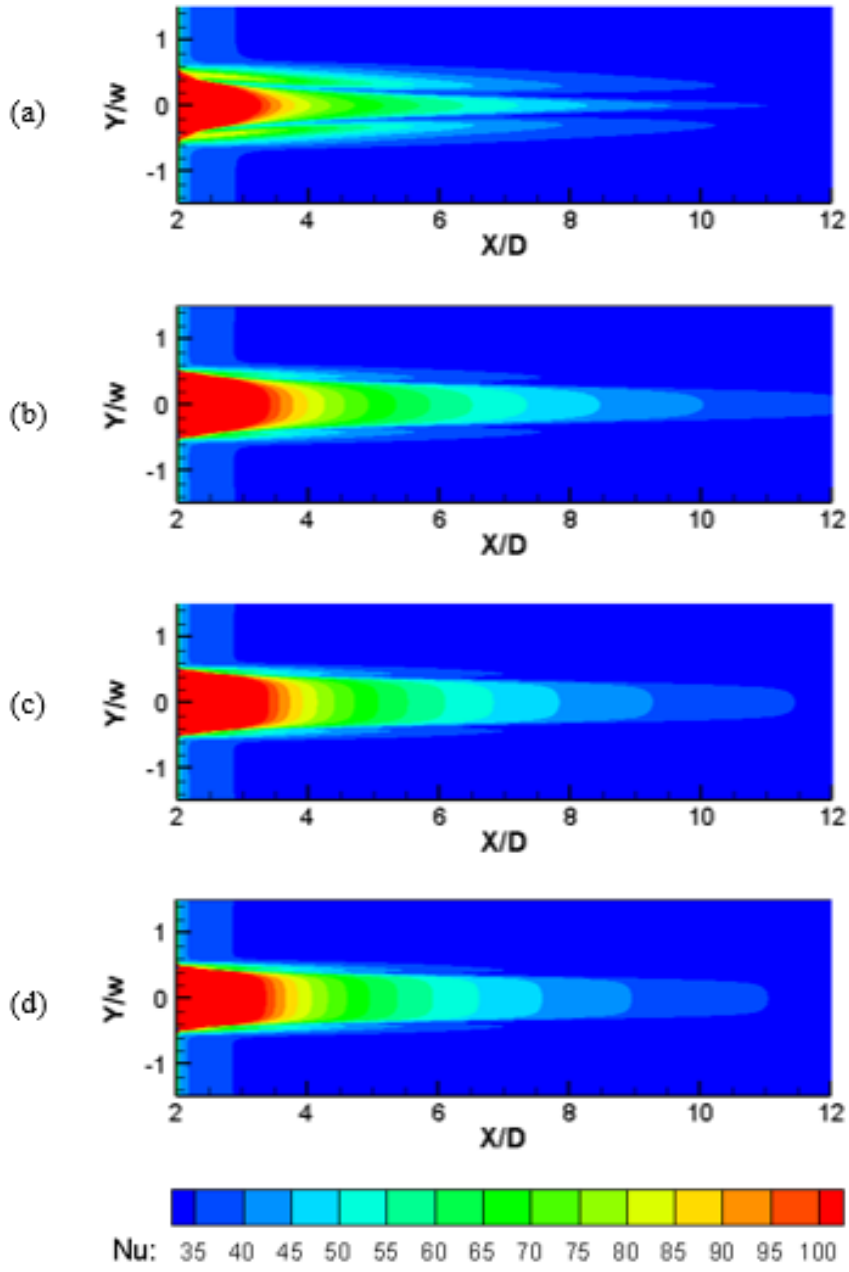

Figure 4.10: Nu number contours on the test surface at M=1 for racetrack slots; having p=3w, and (a) s=2.5b, (b) s=5b, (c) s=7b, (d) s=8b

Nusselt number contours support the finding of the laterally averaged adiabatic film effectiveness curves that the optimum aspect ratio is 7. It yields the higher laterally averaged adiabatic film effectiveness values which can be noticed from the curves in Figure 4.9.

Moreover, its film cooling effect continues with farther downstream distance which can be distinguished with careful examination of Figure 4.10.

The opposite response of the adiabatic film effectiveness indices (the centerline and the laterally averaged ones) to the change of the racetrack aspect ratio could be more clarified by inspecting Figure 4.11 that shows the adiabatic film effectiveness contours over the whole test surface for three selected aspect ratios; 3, 5, and 7. In spite of the confirmed relatively slower decay of the centerline adiabatic film effectiveness values, the contours for the lower racetrack aspect ratios show less uniform adiabatic film effectiveness along the lateral direction. The lateral uniformity is further degraded toward the downstream direction, resulting in the noticed quicker declination of the laterally averaged adiabatic film effectiveness for the lower racetrack aspect ratios.

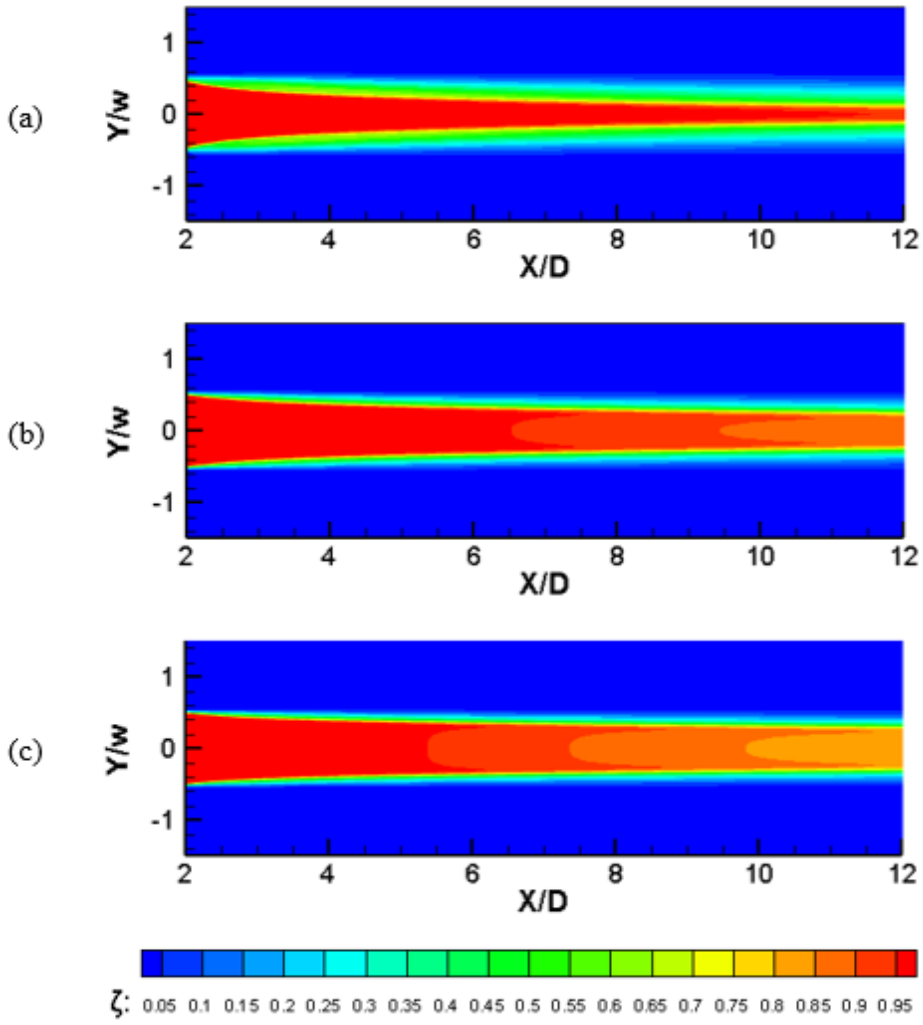

Figure 4.11: Adiabatic film effectiveness contours on the test surface at M=1 for racetrack slots; having p=3w, and (a) s=3b, (b) s=5b & (c) s=7b

4.4.2. Analysis of the Film Thermal Dissipation Mechanisms Associated with the Optimum Racetrack Geometry

The thermal dissipation mechanisms resulting in the film effectiveness decay toward the both sides could be understood by inspecting Figure 4.12 that displays the normalized temperature contours, and Figure 4.13 that presents the cross-flow velocity vectors over the downstream cross-flow plane X/D=10 for different racetrack aspect ratios. The figures suggest that the convective effect resulting from the CRVP is the major reason for the non-uniform

film effectiveness along the lateral direction. For the low racetrack aspect ratios, the CRVPs are more intense, resulting in more diluted film effectiveness at the jet sides. However, along the jet centerline, the low racetrack aspect ratios give higher film effectiveness due to thermal diffusion from the upper jet layers which balances the effect of the CRVP and keeps the jet core temperature unaffected for longer downstream distance. On the other hand, the jet ejected from the high racetrack aspect ratios contains less layers of coolant to cover its core and balance its temperature by thermal diffusion. Therefore, the centerline adiabatic effectiveness suffers from a relatively quicker decay.

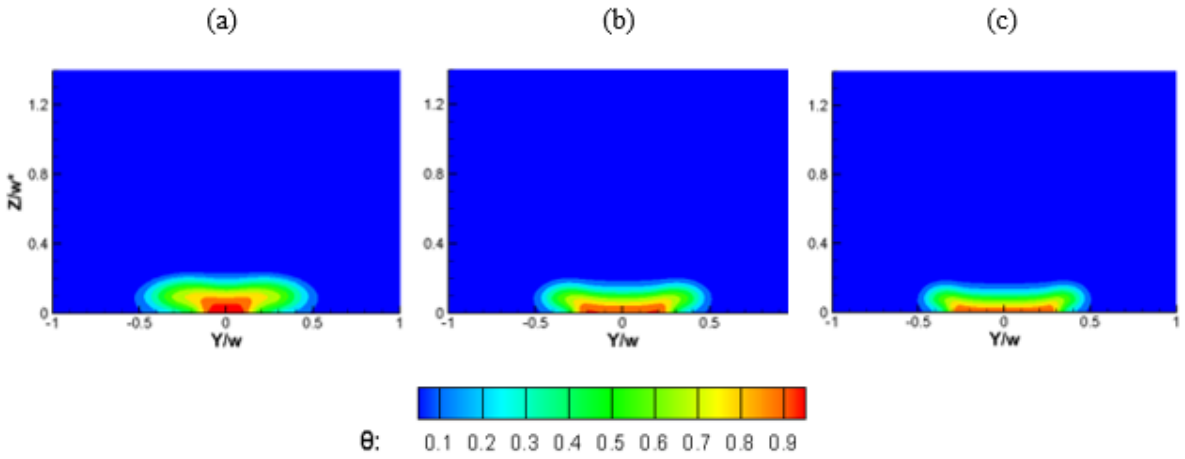

Figure 4.12: Normalized temperature contours on the cross-flow plane X/D=10 at M=1 for racetrack slots; having p=3w, and (a) s=3b, (b) s=5b, (c) s=7b

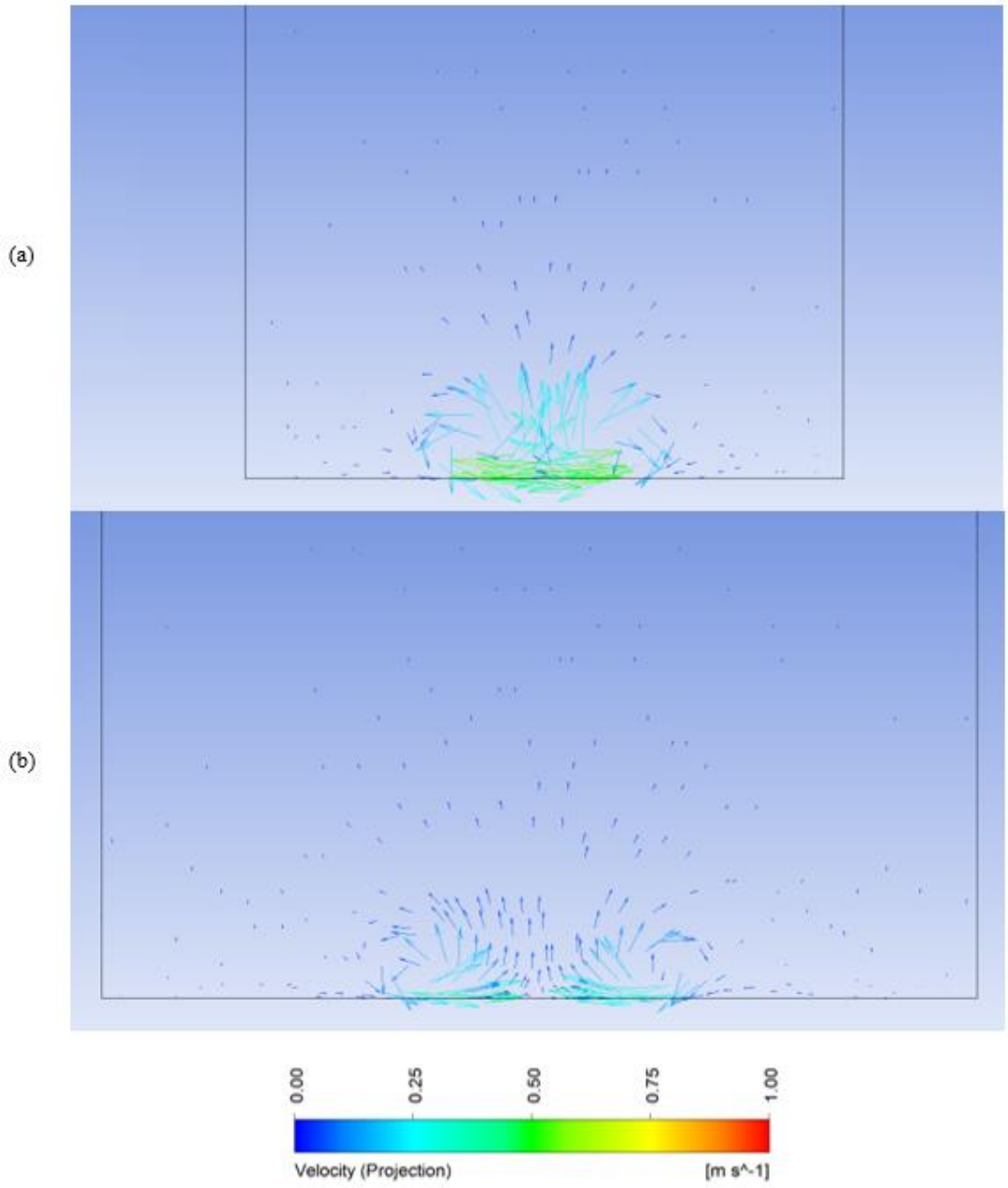

Figure 4.13: Cross-flow velocity vectors over the cross-flow plane X/D=10 at M=1 for racetrack slots; having p=3w, and (a) s=3b, (b) s=7b

To observe the development of the coolant jet and its attachment to the cooled surface, the normalized U-velocity contours along the jet centerline are presented in Figure 4.14. Although the jet is detached from the surface, it doesn't experience a severe lift-off. Figure 4.15 shows, side by side, the normalized U-velocity and temperature contours at three separate

downstream cross-flow planes X/D=2, X/D=6, and X/D=10 to compare the development of the jet with the temperature distribution. The detachment of the jet, along with the observed CRVP, led to a decrease in the surface film temperature which describes the decrease in adiabatic film effectiveness toward the downstream direction that was noticed from Figure 4.11. However, the effect of the jet detachment was balanced, to a certain extent, by the thermal diffusion as suggested before.

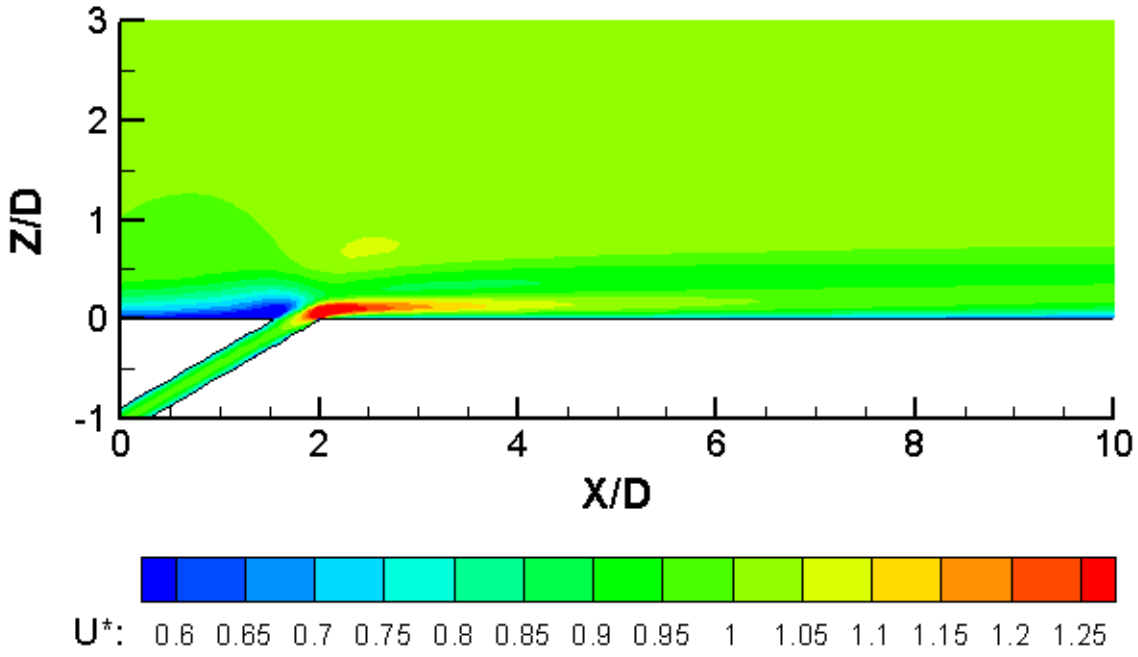

Figure 4.14: Normalized U-velocity contours along the jet centerline at M=1 for the racetrack slot; having p/w=3, and s/b=7

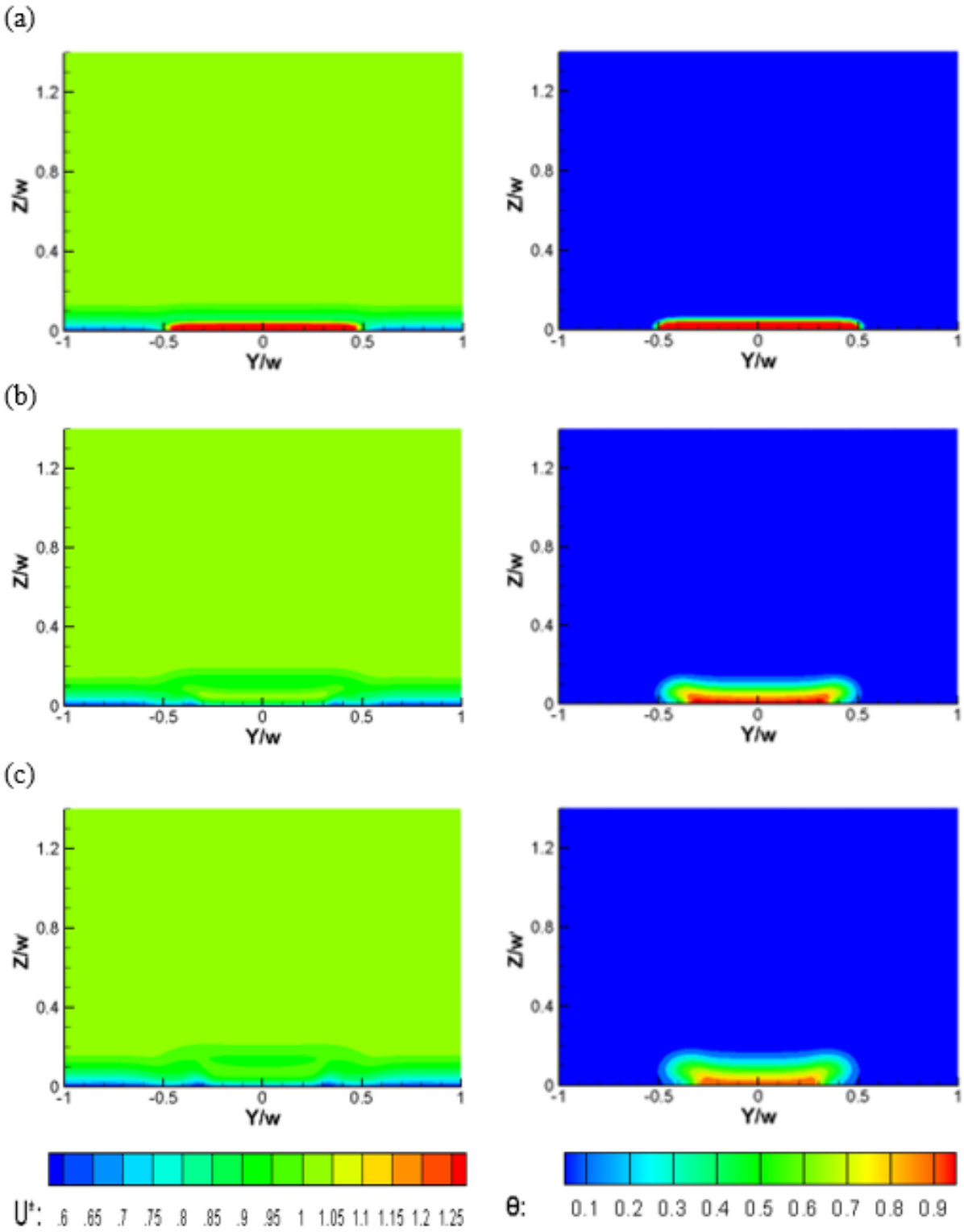

Figure 4.15: Normalized U-velocity and temperature contours on cross-flow planes (a) X/D=2, (b) X/D=6, (c) X/D=10; at M=1 for the racetrack slot having p/w=3, and s/b=7

4.5. Irregular Pipe Geometry Optimization Using the Adjoint Solver for the Case M=1

4.5.1. Stepwise Optimized Irregular Pipe Geometries

Starting from the optimum racetrack geometry, the optimization is proceeded with a less conservative strategy at which irregular coolant hole shape is allowed. However, making and testing irregular shape changes manually is not as powerful as using a reliable numerical optimization tool. The *ANSYS Fluent Adjoint solver* was chosen for the coolant nozzle's irregular shape optimization. The solver provides, based on the standing flow situation, a map of sensitivity of the selected observable to the surface deformation. Based on the sensitivity map, the predefined geometry morphing conditions, and the optimization objective; three consecutive cycles of the adjoint optimization tool suggested that the coolant holes exit shapes presented in Figure 4.16 progressively increase the average adiabatic film effectiveness over the test surface. However, the pipe cross-sectional shapes weren't fixed to the shape of the pipe exit. Figure 4.17 shows the coolant pipe geometries resulted from the three stepwise adjoint optimization cycles.

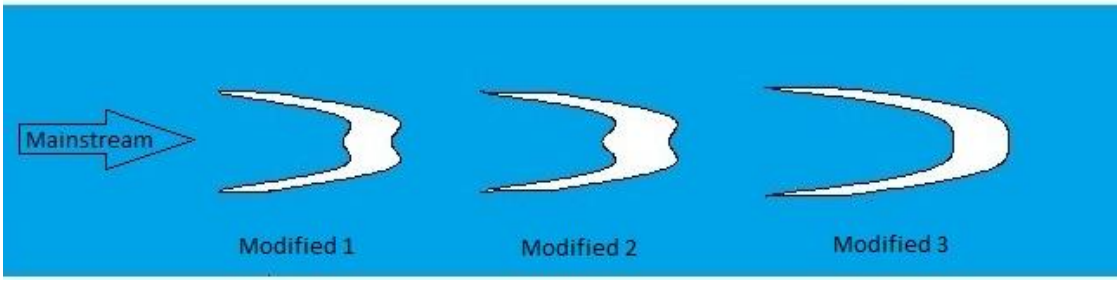

Figure 4.16: The coolant holes' exit shapes resulted from three steps of the Adjoint solver optimization tool

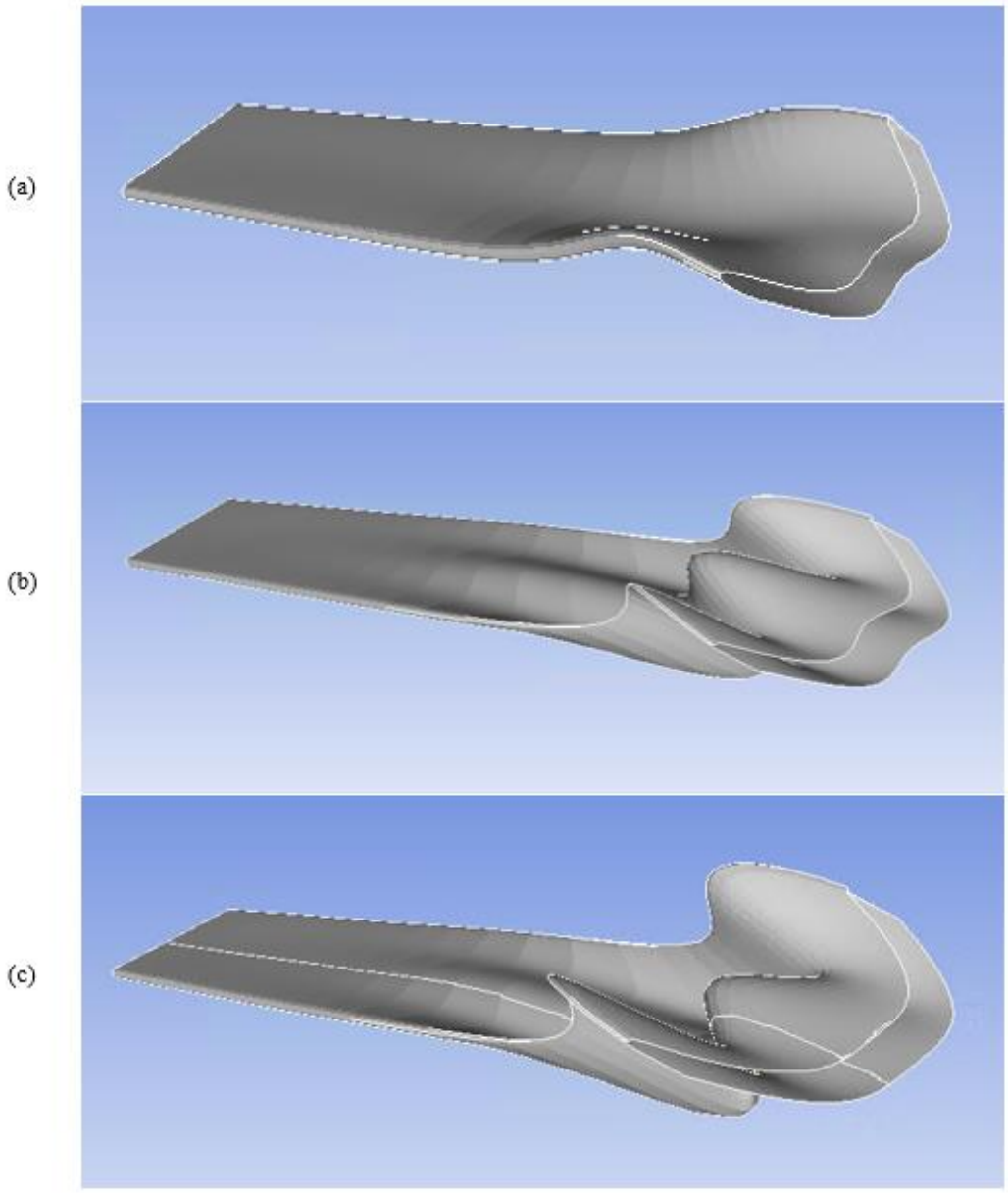

Figure 4.17: General view for the (a) 1st nozzle shape, (b) the 2nd nozzle shape, (c) the 3rd nozzle shape; modified from the racetrack slot, having s=7b; utilizing the ANSYS Fluent Adjoint solver

Each geometry was morphed from the previous one in a manner that satisfies the optimization goal with less geometric change; the optimal surface displacement. The strategy is to apply greater changes to the areas of higher sensitivity. Figure 4.18 shows an example of computed normal optimal displacement contours over the first modified coolant pipe wall that

are expected, when combined with the tangential components vectors, to achieve 1% reduction of the test surface average temperature. The positive values of the contours indicate a movement toward the flow domain, and vice versa. Applying these normal displacements, along with the tangential ones, morphed the coolant pipe from the first modified geometry to the second modified one appear in Figure 4.17a Figure 4.17b respectively.

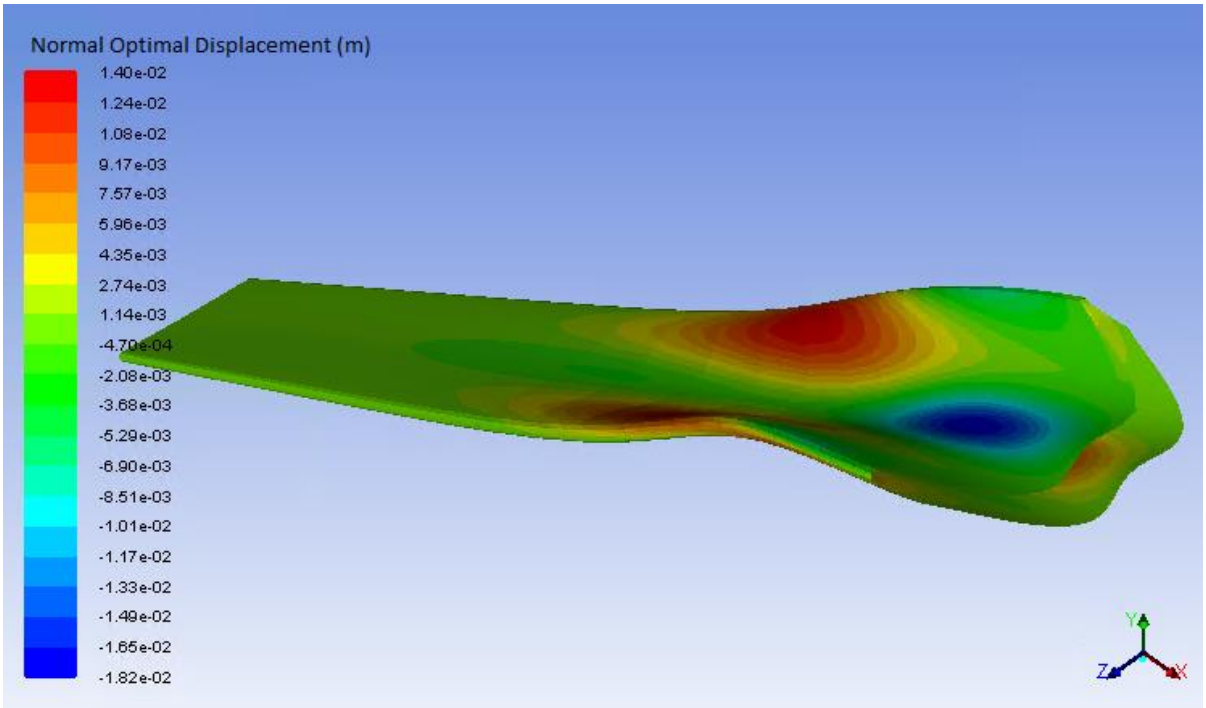

Figure 4.18: Example for the optimal displacement contours, normal to the coolant-pipe's wall, expected by the Adjoint solver to fulfill the optimization objective

1% reduction in test surface average temperature was targeted for the first and the second modification steps. For the third one, the optimization goal is declined to 0.5% average temperature reduction. It was found that targeting more promising goals lead to mesh distortion. Furthermore, the expectation accuracy deteriorates with the optimistic targets as the nonlinearity effect becomes more significant. To test the performance of each modified geometry, the flow was recomputed using the *ANSYS Fluent solver* and the validated realizable

k-ε model with scalable wall function. The results are utilized to identify the optimum pipe geometry and analyze its thermal performance.

4.5.2. Identifying the Optimum irregular pipe geometry

The laterally averaged adiabatic film effectiveness values of the three modified irregular pipe shapes are compared to that of the optimization basic shape, the racetrack slot having an aspect ratio of 7, in Figure 4.19. The curves show a significant enhancement attained through the first and the second optimization steps. No further improvement is provided out of the third optimization step except at the short downstream vicinity of the coolant hole trailing edge; from X/D=2 to X/D=3. Afterward, the laterally averaged adiabatic film effectiveness of the third modified shape rapidly decreased and became less than that of the first modified one before reaching the downstream location X/D=7, then continued to decline. The improvement associated with the first modified shape over the optimization basic one increases towards the downstream direction. The opposite is true for the second optimization step at which the curves of the firs and the second modified shapes converge with the advancement of the flow. However, the laterally average adiabatic film effectiveness of the second modified shape maintains its privilege over the first modified and the optimization basic ones all the way throughout the downstream distance presented in Figure 4.19, with minimum 2% improvement over the first modified shape at the downstream location X/D=10.

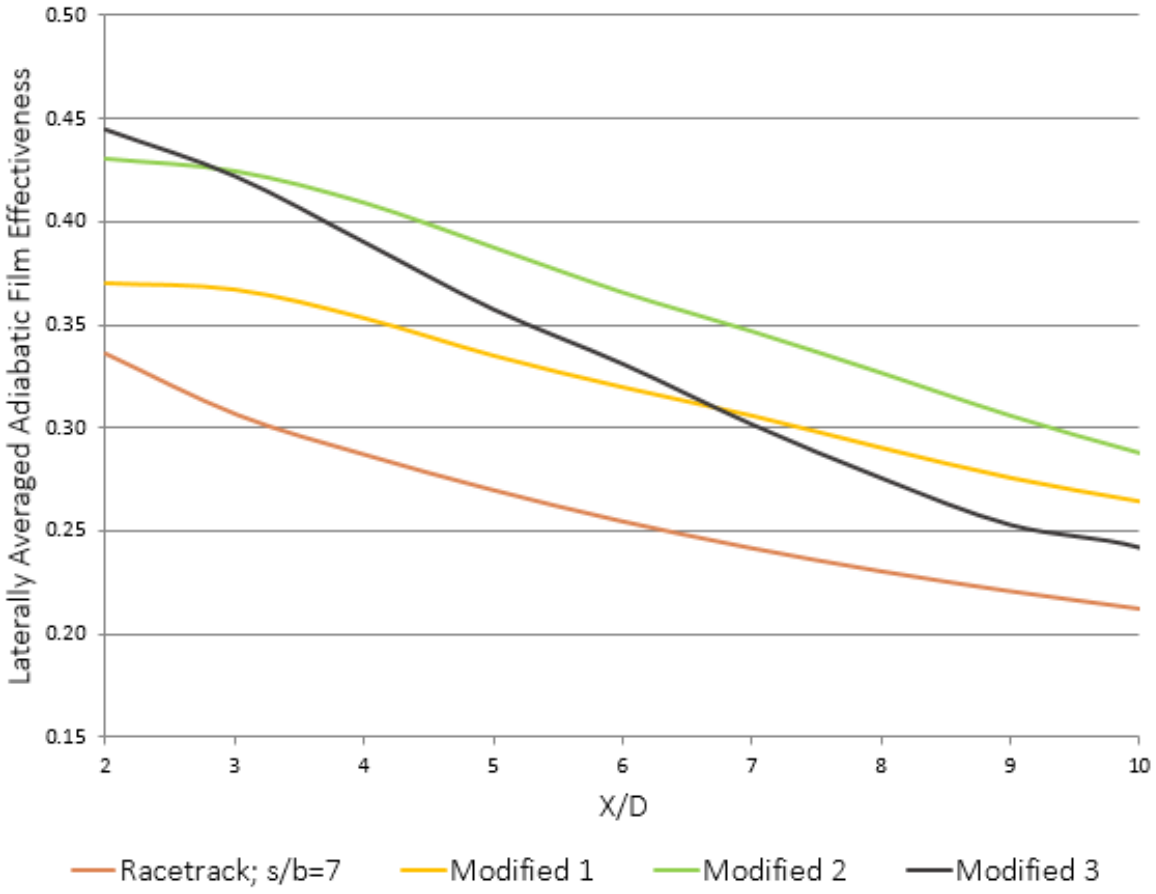

Figure 4.19: Laterally averaged adiabatic film effectiveness comparison between the racetrack slot, having s/b=7; and the three modified nozzles; at M=1

It is clear from the laterally average adiabatic film effectiveness curves, presented in Figure 4.19, that the second modified pipe shape gives the highest average film effectiveness among the tested geometries. Nevertheless, the lateral variance of the film effectiveness and the coverage area of the film are not clear yet. These key design indicators can be noticed by means of the adiabatic film effectiveness contours over the whole test area, presented in Figure 4.20. The contours show laterally expanding film for the second and the third irregular modified shapes. No lateral film expansion is noticed for the first modified shape, while the contours of the racetrack shows a laterally converging film trend. However, it seems that the

advantage of the lateral film expansion is associated with quick decay of the film effectiveness at the jet middle regions.

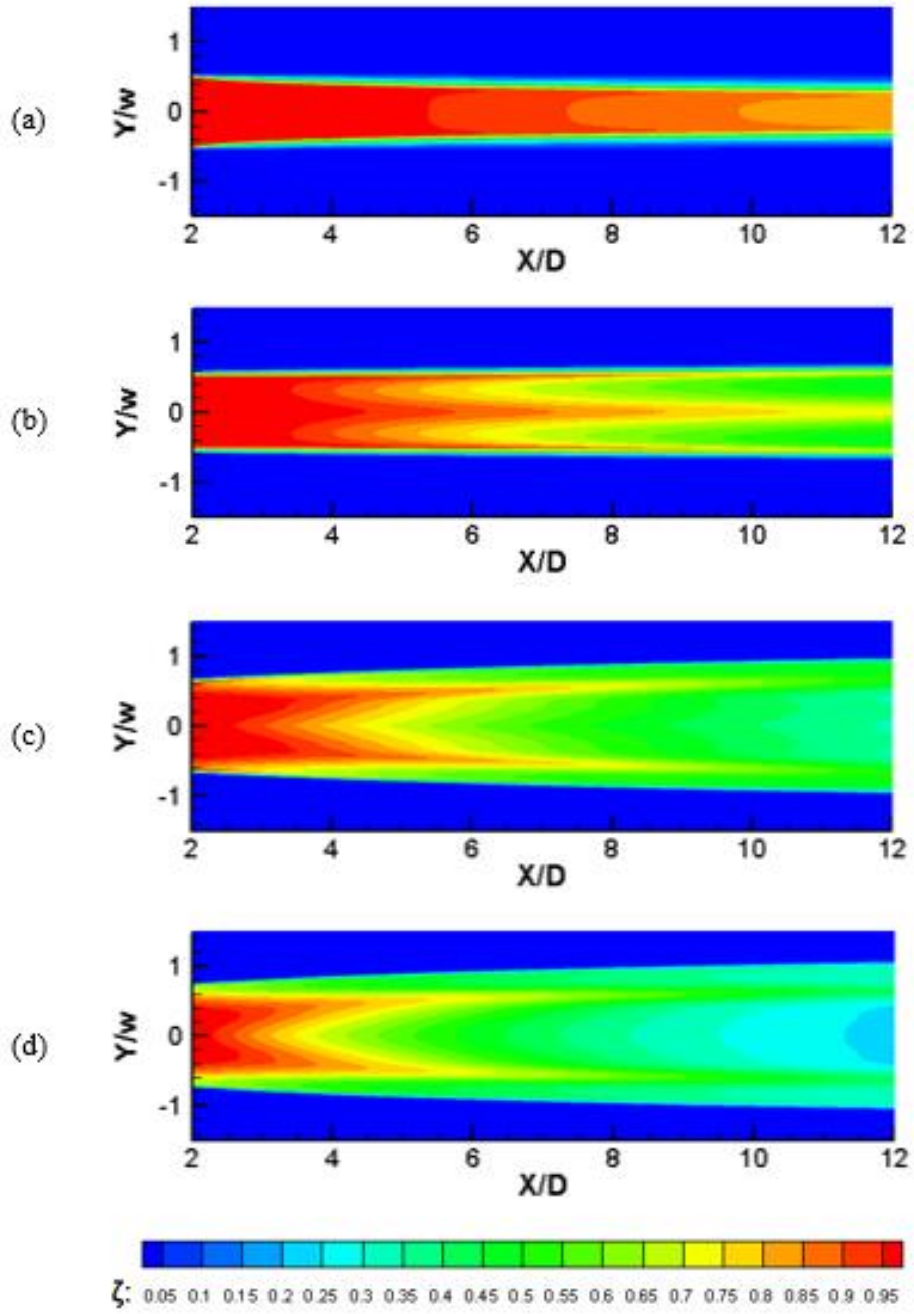

Figure 4.20: Adiabatic film effectiveness contours on the test surface at M=1 for (a) the racetrack slot, having s=7b; (b) 1st modified nozzle; (c) the 2nd modified nozzle; (d) the 3rd modified nozzle

The conclusion of the earlier decay of the film cooling effect along the jet centerline associated with each shape modification step is confirmed by Nusselt number contours over the test surface for the optimization basic and the three modified shapes presented in Figure 4.21. In spite of that, the two side spikes in Nusselt number contours accompanying with the second and the third modified shapes recover and spread the film cooling effect over broader regions with noticeable advantage of the former over the later.

According to the above analysis (both adiabatic and non-adiabatic ones), the second modified pipe geometry presented in Figure 4.17b was found to be the optimum pipe geometry modified by the Adjoint solver optimization tool. Therefore, it will be subjected to further analysis in the next section.

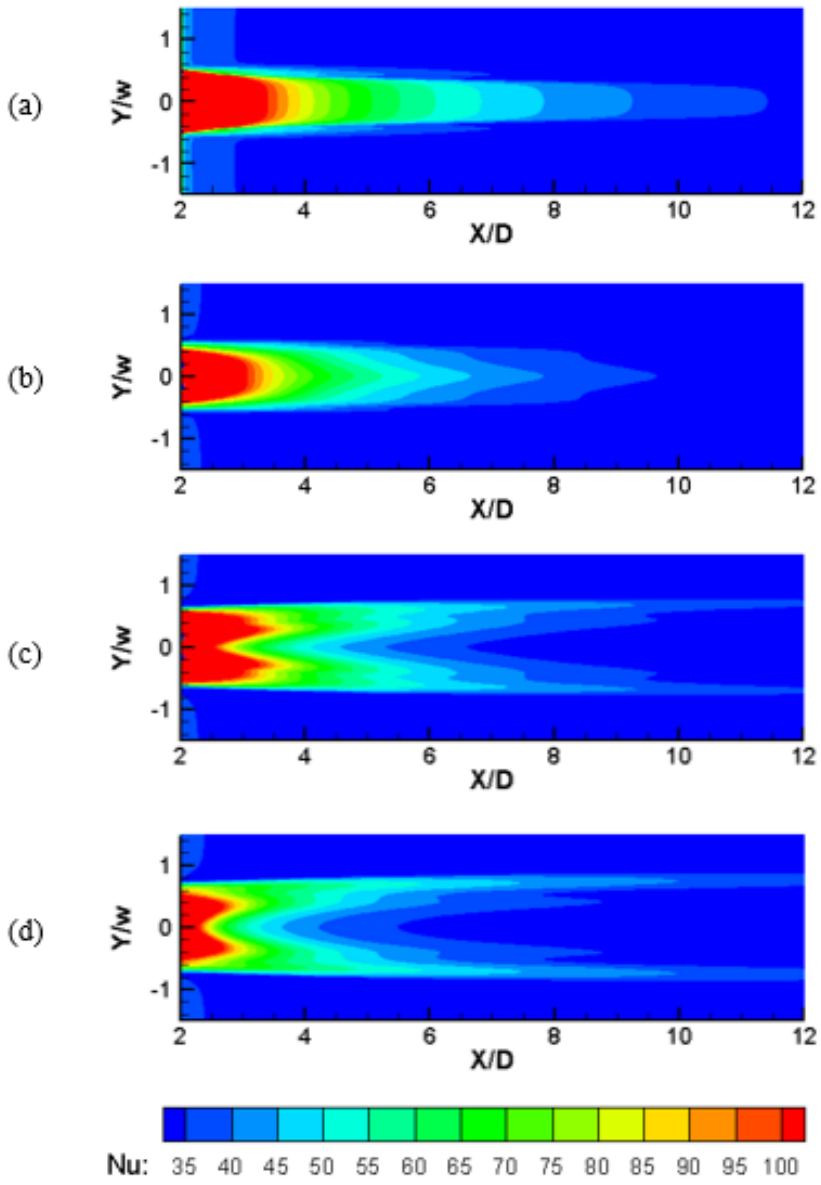

Figure 4.21: Nu number contours on the test surface at M=1 for (a) the racetrack slot, having s=7b; (b) 1st modified nozzle; (c) the 2nd modified nozzle; (d) the 3rd modified nozzle

4.5.3. Analysis of the Film Thermal Dissipation Mechanisms Associated with the Optimum Irregular Pipe Shape

To understand the film thermal behavior along the three dimensions, normalized temperature contours on the cross-flow plane X/D=10 is compared to these of the optimum racetrack slot in Figure 4.22. The figure shows less layers of the coolant jet covering the film

downstream the second modified shape when compared to the optimum racetrack slot. The lack of the covering layers decreases the chance of the film to partially compensate its cooling effect through thermal diffusion.

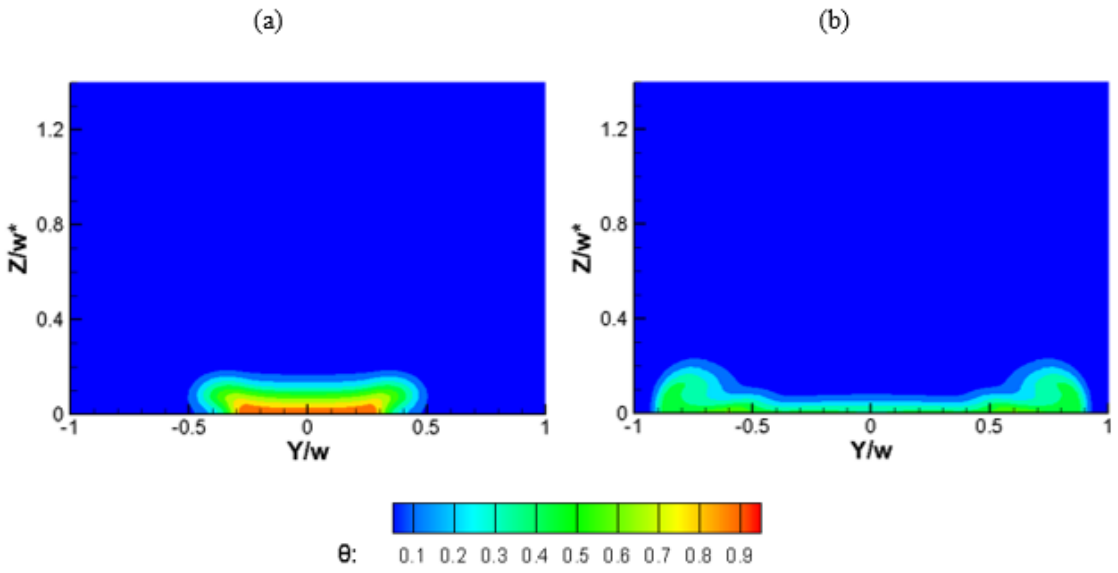

Figure 4.22: Normalized temperature contours on the cross-flow plane X/D=10 at M=1 for (a) the racetrack slot, having s=7b; (b) the 2nd modified nozzle

Figure 4.23 shows the cross-flow velocity vectors over two cross-flow planes: X/D=5, and X/D=10; downstream the second modified coolant pipe. The remarkable finding is the formation of a relatively large anti-vortex pair. The center of the anti-vortex pair moves away from the jet center toward the domain boarders. The lateral movement stops before the jet reach the downstream location X/D=5 at which each vortex meets another vortex that accompanies the adjacent coolant jet at the computational domain's side boundaries; This is the only interaction recorded between adjacent coolant holes during the current study. Afterwards, the effect of the vortex core movement is eliminated and only the tangential relative velocity component exists. A consequent lateral spread of the cooling film can be noticed from the normalized streamwise and temperature contours presented in Figure 4.24.

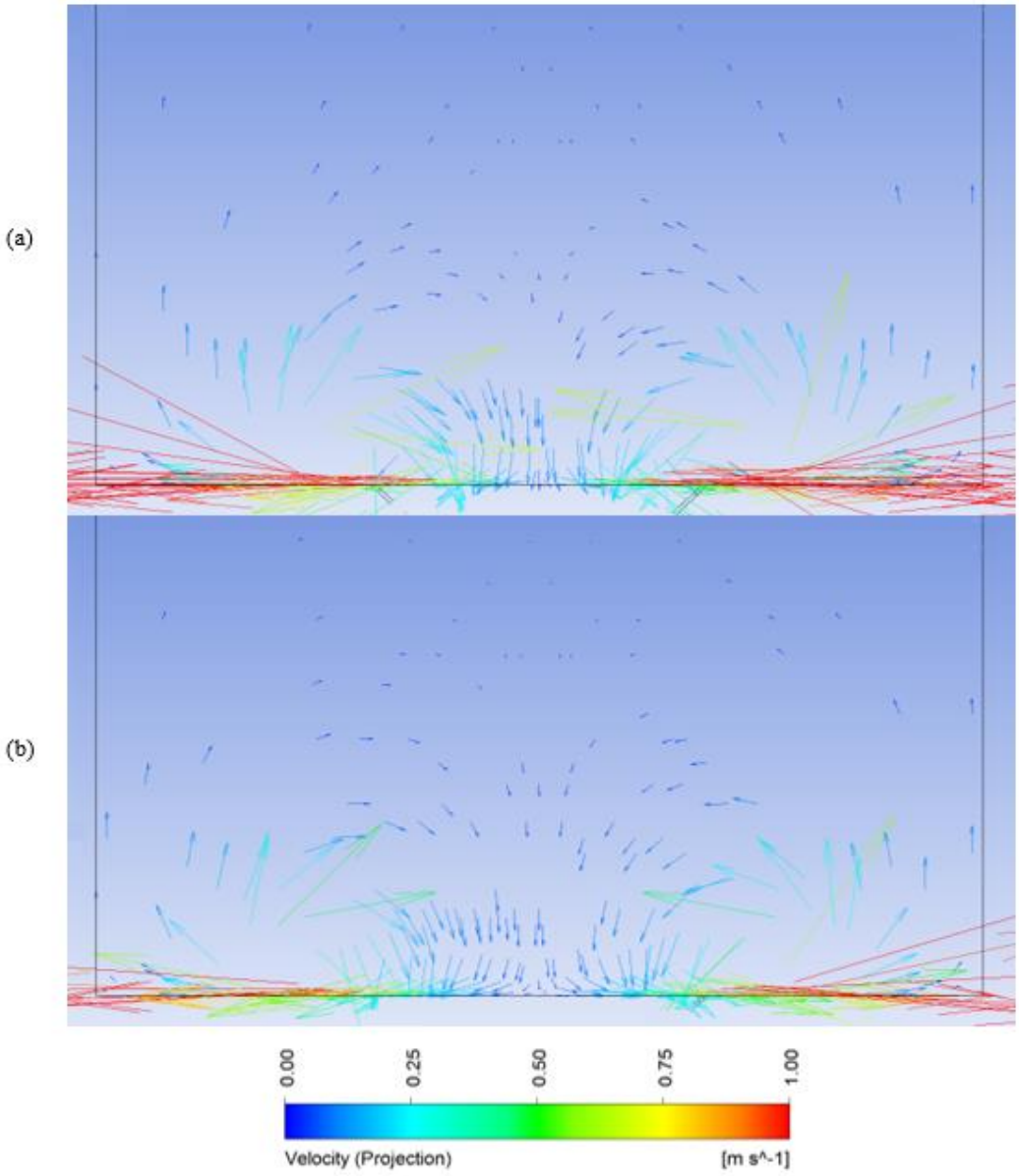

Figure 4.23: Cross-flow velocity vectors over cross-flow planes (a) X/D=5, (b) X/D=10; at M=1 for the 2nd modified nozzle

The downward velocity vectors at the jet center region, appear in Figure 4.23, results in a favorable and unfavorable effects. The favorable effect is the improved jet attachment witch is clear from the development of the normalized streamwise contours appear in Figure 4.24. On the other hand, the vortex carries the mainstream high temperature air into the jet core

resulting in an increasing film effectiveness dilution along the flow direction as it is clear from the normalized temperature contours in Figure 4.24.

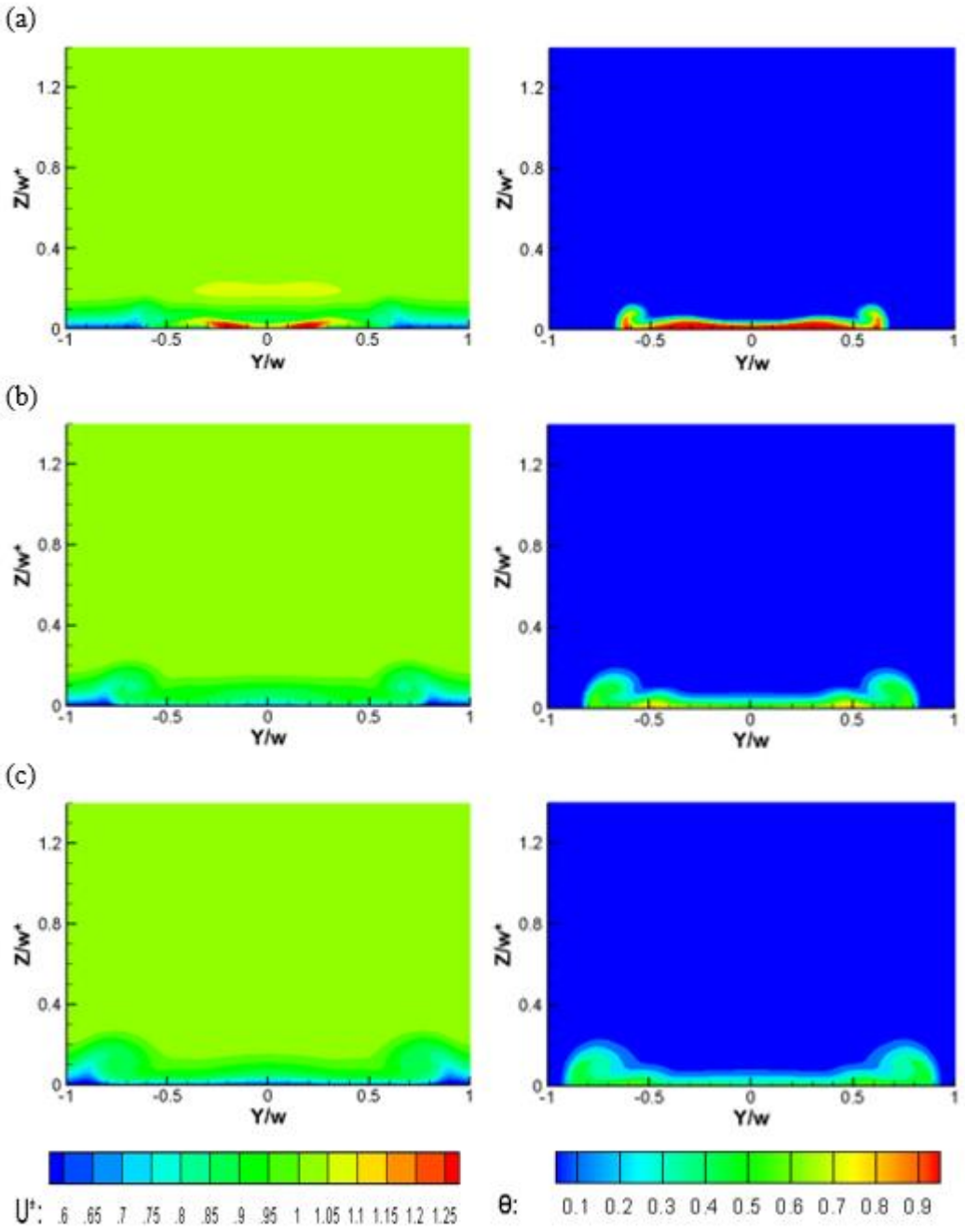

Figure 4.24: Normalized U-velocity and temperature contours on cross-flow planes (a) X/D=2, (b) X/D=6, (c) X/D=10; at M=1 for the 2nd modified nozzle

5. CONCLUSIONS

The realizable *k-ε* model with scalable wall function was found to be the more suitable numerical model, *among the other studied RANS-based ones*, conforming to the experimental aerodynamics and thermal performance indices at blowing ratio of one. The four compared RANS-based turbulence models are: *Standard k-ε with scalable wall function*, *Realizable k-ε with scalable wall function*, *SST k-ω*, and *EARSM k-ε with scalable wall function*. Turbulent Prandtl number was found to have direct effect on film cooling due to its impact to thermal diffusivity. Accordingly, it was progressively decreased for two studied turbulence models; *SST k-ω* and *standard k-ε with scalable wall function*, to counteract the models' over-predicted jet detachment by models' artificial thermal diffusion. However, for the blowing ratio of two, the tested models failed to predict the experimental measurement of film cooling, confirming the recognized inaccuracy of RANS-based models to predict film cooling behavior at high blowing ratios, which normally lead to severe jet detachment. Accordingly, the optimization study was limited to the flow with blowing ratio of one.

The realizable *k-ε* model with scalable wall function predicted the cooling effect for the racetrack slot to be higher than that for circular hole. Accordingly, the research was directed toward the investigation of the effect of a racetrack geometry parameter, *the aspect ratio*, on cooling performance at blowing ratio of one, to attain an optimum value. Seeking for even better cooling performance, the output of this manual regular shape optimization served as starting point for subsequent irregular shape optimization utilizing a numerical optimization tool; ANSYS Fluent Adjoint solver.

Throughout the optimization study, the coolant holes' flow area and the pitch-to-width; *alternatively, pitch-to-diameter*; ratio were fixed in order to single out the effect of the coolant hole geometry.

Results of the manual regular shape optimization showed that the racetrack slot yields higher performance than the circular hole and that the performance is a function of the aspect ratio. The aspect ratio was varied from 2.5 to 8 and, within this range, the laterally averaged adiabatic film effectiveness had increased from 0.15 to 0.21 at the downstream distance [X/D=10]. This is a notable enhancement (more than double) when compared to 0.09; the value of the laterally averaged adiabatic film effectiveness of circular hole at the same downstream distance [X/D=10]. The heat transfer was also evaluated for the seven racetrack geometries in terms of Nusselt number. The results showed higher overall heat transfer and greater spread at very low and very high aspect ratios. It also showed a more localized (around the centerline), but farther extent of heat transfer effect for the intermediate aspect ratio [s/b=5]. Combining adiabatic film effectiveness data with Nusselt number distribution over the test surface designated the racetrack aspect ratio of 7 to be the optimum one.

Date captured from the next stage, the irregular shape optimization, resulted in optimum coolant pipe geometry in two steps. Running the Adjoint solver for third step did not yield further cooling enhancement except for the near downstream region; from X/D=2 to X/D=3, indicating that the new expectation overshoots the local optimum point of the objective function. The adiabatic film effectiveness indicators over the test surface determine that the jet ejected from the optimum coolant pipe geometry (modified 2) expands as it moves toward the downstream direction, giving it an advantage of higher film effectiveness and broader film coverage area. The wider cooling effect of the film was also noticed from Nusselt number

contours over the test surface. However, the lateral spread of the second modified pipe dilutes the film around the jet centerline, but still gives higher average adiabatic film effectiveness over the test surface.

The CRVP associated with the coolant jet was found to be the most important phenomenon affecting the film thermal behavior, indicating great influence of the convective term over the diffusive one in film effectiveness dissipation. Increasing the racetrack aspect ratio resulted in less intense and far from each other vortex pair. Both features are expected to enhance the film cooling effect and lessen the jet detachment tendency. For the optimum irregular shape (modified 2), a formation of anti-vortex pair is noticed. The anti-vortex pair causes the film lateral expansion, but work on diluting the film effectiveness along jet centerline. However, it also encourages the jet attachment to the cooled surface, which adds balancing effect to the film dissipation mechanisms at this region.

6. RECOMMENDATIONS FOR FUTURE STUDIES

Developing an LES model to approach the system physics and behavior accurately at higher blowing ratio, which normally lead to severe jet detachment, is recommended to allow for further shape optimization under wider operating range.

Experimental measurements are needed to verify the outperformance of the designated optimum pipe geometry (modified 2). The recent advancement in additive manufacturing techniques facilitates the production of irregular shapes, and allows for experimental tests. Moreover, checking the impact of the new shape (modified 2) on the aerodynamic losses is essential to understand the effect of the optimized irregular geometry on turbine efficiency.

REFERENCES

[1] Y. Cengel and M. Boles, Thermodynamics: An Engineering Approach, 4th ed., McGraw-Hill, 2002.

[2] J. Sargison, "Development of a Novel Film Cooling Hole Geometry," Oxford, UK, 2001.

[3] M. Boyce, Gas Turbine Engineering Handbook, 2nd ed., Gulf Professional Publishing, 2002.

[4] C. Soares, Gas Turbines: A Handbook of Air, Land and Sea Applications, 2nd ed., Butterworth-Heinemann - Elsevier, 2015.

[5] J.-H. Han, S. Dutta and S. Ekkad, Gas Turbine Heat Transfer and Cooling Technology, 2nd ed., CRC Press, 2013.

[6] R. Goldstein, "Film Cooling," in *Advances in Heat Transfer*, vol. 7, Elsevier, 1971, pp. 321-379.

[7] H. Kruse, "Effects of Hole Geometry, Wall Curvature and Pressure Gradient on Film Cooling Downstream of a Single Row," in *Heat Transfer and Cooling in Gas Turbines: AGARD-CP-390*, Bergen, 1985.

[8] J.-C. HAN and S. EKKAD, "Recent Development in Turbine Blade Film Cooling," *International Journal of Rotating Machinery,* vol. 7, no. 1, pp. 21-40, 2001.

[9] M. Akbar, B. Alsaidi, R. Painter, L. Sharpe and S. Ghiaasiaan, "The Effects of Coolant Pipe Geometry and Flow Conditions on Turbine Blade Film Cooling," *Journal of Thermal Engineering,* vol. 3, pp. 1196-1210, 2017.

[10] T. Fric and A. Roshko, "Vortical Structure in the Wake of a Transverse Jet," *Journal of Fluid Mechanics,* vol. 279, pp. 1-47, 1994.

[11] J. Ramsey and R. Goldstein, "Interaction of a Heated Jet With a Deflecting Stream," *ASME Journal of Heat Transfer,* vol. 93, no. 4, pp. 365-372, 1971.

[12] R. Martinez-Botas and C. Yuen, "Measurement of Local Heat Transfer Coefficient and Film Cooling Effectiveness through Discrete Holes," in *ASME Turbo Expo 2000: Power for Land, Sea, and Air*, Munich, 2000.

[13] P. Renze, W. Schroder and M. Meinke, "Large-Eddy Simulation of Film Cooling Flows at Density Gradients," *International Journal of Heat and Fluid Flow,* vol. 29, no. 1, pp. 18-34, 2008.

[14] K. Thole, A. Sinha, D. Bogard and M. Crawford, "Mean Temperature Measurements of Jets with a Crossflow for Gas Turbine Film Cooling Application," in *the Third International Symposium on Transport Phenomena and Dynamics of Rotating Machinery (ISROMAC-3)*, Honolulu, 1990.

[15] A. Sinha, D. Bogard and M. Crawford, "Film-Cooling Effectiveness Downstream of a Single Row of Holes With Variable Density Ratio," *ASME Journal of Turbomachinery,* vol. 113, no. 3, pp. 442-449, 1991.

[16] J. Bons, C. MacArthur and R. Rivir, "The Effect of High Free-Stream Turbulence on Film Cooling Effectiveness," *ASME Journal of Turbomachinery,* vol. 118, no. 4, pp. 814-825, 1 October 1996.

[17] J. Mayhew, J. Baughn and A. Byerley, "The Effect of Freestream Turbulence on Film Cooling Adiabatic Effectiveness," *International Journal of Heat and Fluid Flow,* vol. 24, no. 5, p. 669–679, 2003.

[18] N. Foster and D. Lampard, "The Flow and Film Cooling Effectiveness Following Injection through a Row of Holes," *ASME Journal of Engineering for Power,* vol. 102, no. 3, pp. 584-588, 1980.

[19] R. Goldstein, E. Eckert and F. Burggraf, "Effects of Hole Geometry and Density on Three-Dimensional Film Cooling," *International Journal of Heat and Mass Transfer,* vol. 17, no. 5, pp. 595-607, 1974.

[20] A. Teekaram, C. Forth and T. Jones, "Film Cooling in the Presence of Mainstream Pressure Gradients," *ASME Journal of Turbomachinery,* vol. 113, no. 3, pp. 484-492, 1991.

[21] D. Schmidt and D. Bogard, "Pressure Gradient Effects on Film Cooling," in *ASME 1995 International Gas Turbine and Aeroengine Congress and Exposition*, Houston, 1995.

[22] J. Hartnett, R. Birkebak and E. Eckert, "Velocity Distributions, Temperature Distributions, Effectiveness and Heat Transfer for Air Injected Through a Tangential Slot into a Turbulent Boundary Layer," *ASME Journal of Heat Transfer,* vol. 83, no. 3, pp. 293-305, 1961.

[23] K. Wieghardt, "Hot Air Discharge for De-Icing," 1943.

[24] R. Seban, "Heat Transfer and Effectiveness for a Turbulent Boundary Layer with Tangential Fluid Injection," *ASME Journal of Heat Transfer,* vol. 82, no. 4, pp. 303-312, 1960.

[25] D. Metzger, H. Carper and L. Swank, "Heat Transfer with Film Cooling near Nontangential Injection Slots," *ASME Journal of Engineering for Power,* vol. 90, no. 2, pp. 157-162, 1968.

[26] E. J. Logan and R. Roy, Handbook of Turbomachinery, 2nd ed., New York: Marcel Dekker, 2003.

[27] K. Shalash, L. El-Gabry and M. Abo El-Azm, "Numerical Modelling of Slot Film Cooling Using a Wall Function," in *ASME Turbo Expo 2013: Turbine Technical Conference and Exposition*, San Antonio, 2013.

[28] P. Singh, B. Ravi and S. Ekkad, "Experimental Investigation of Heat Transfer Augmentation by Different Jet Impingement Hole Shapes under Maximum Crossflow," in *ASME Turbo Expo 2016: Turbomachinery Technical Conference and Exposition*, Seoul, 2016.

[29] R. Goldstein, E. Eckert and J. Ramsey, "Film Cooling with Injection Through Holes: Adiabatic Wall Temperatures Downstream of a Circular Hole," *ASME Journal of Engineering for Power,* vol. 90, no. 4, pp. 384-393, 1968.

[30] P. Ligrani, S. Ciriello and D. Bishop, "Heat Transfer, Adiabatic Effectiveness, and Injectant Distributions Downstream of a Single Row and Two Staggered Rows of Compound Angle Film-Cooling Holes," *ASME Journal of Turbomachinery,* vol. 114, no. 4, pp. 687-700, 1992.

[31] P. Ligrani, J. Wigle, S. Ciriello and S. Jackson, "Film-Cooling From Holes With Compound Angle Orientations: Part 1—Results Downstream of Two Staggered Rows of Holes With 3d Spanwise Spacing," *ASME Journal of Heat Transfer,* vol. 116, no. 2, pp. 341-352, 1 May 1994.

[32] M. Berhe, "A Numerical Study of Discrete-Hole Film Cooling," Minneapolis, USA, 1997.

[33] S. Ekkad, D. Zapata and J. Han, "Film Effectiveness Over a Flat Surface With Air and CO2 Injection Through Compound Angle Holes Using a Transient Liquid Crystal Image Method," *ASME Journal of Turbomachinery,* vol. 119, no. 3, pp. 587-593, 1 July 1997.

[34] S. Ekkad, D. Zapata and J. Han, "Heat Transfer Coefficients Over a Flat Surface With Air and CO2 Injection Through Compound Angle Holes Using a Transient Liquid Crystal Image Method," *ASME Journal of Turbomachinery,* vol. 119, no. 3, pp. 580-586, 1 July 1997.

[35] B. Sen, D. Schmidt and D. Bogard, "Film Cooling With Compound Angle Holes: Heat Transfer," *ASME Journal of Turbomachinery,* vol. 118, no. 4, pp. 800-806, 1 October 1996.

[36] Z. Gao, D. Narzary and J. Han, "Film Cooling on a Gas Turbine Blade Pressure Side or Suction Side with Axial Shaped Holes," *International Journal of Heat and Mass Transfer,* vol. 51, no. 9-10, p. 2139–2152, 2008.

[37] C. Yuen and R. Martines-Botas, "Film Cooling Characteristics of a Single Round Hole at Various Streamwise Angles in a Crossflow: Part I Effectiveness," *International Journal of Heat and Mass Transfer,* vol. 46, no. 2, p. 221–235, 2003.

[38] A. Kohli and D. Bogard, "Adiabatic Effectiveness, Thermal Fields, and Velocity Fields for Film Cooling With Large Angle Injection," *Journal of Turbomachinery,* vol. 119, no. 2, pp. 352-358, 1997.

[39] R. Jai, B. Sunden, P. Miron and B. Leger, "A Numerical and Experimental Investigation of the Slot Film-cooling Jet With Various Angles," *ASME Journal of Turbomachinery,* vol. 127, no. 3, pp. 635-645, 2005.

[40] R. Bunker, "A Review of Shaped Hole Turbine Film-Cooling Technology," *ASME Journal of Heat Transfer,* vol. 127, no. 4, pp. 441-453, 2005.

[41] W. Colban and K. Thole, "Influence of Hole Shape on the Performance of a Turbine Vane Endwall Film-Cooling Scheme," *International Journal of Heat and Fluid Flow,* vol. 28, no. 3, p. 341–356, 2007.

[42] J. Farmer, D. Seager and J. Liburdy, "The Effect of Shaping Inclined Slots on Film Cooling Effectiveness and Heat Transfer Coefficient," in *ASME 1997 International Gas Turbine and Aeroengine Congress and Exhibition*, Orlando, 1997.

[43] D. Hyams, K. McGovern and J. Leylek, "Effects of Geometry on Slot-Jet Film Cooling Performance," ASME Paper 96-GT-187," in *ASME 1996 International Gas Turbine and Aeroengine Congress and Exhibition*, Birmingham, 1996.

[44] J. Sargison, S. M. Guo, M. Oldfield, L. G.D. and A. Rawlinson, "A Converging Slot-Hole Film-Cooling Geometry: Part 1 — Low-Speed Flat-Plate Heat Transfer and Loss," in *ASME Turbo Expo 2001: Power for Land, Sea, and Air*, New Orleans, 2001.

[45] J. Sargison, M. Oldfield, S. Guo, G. Lock and A. Rawlinson, "Flow Visualisation of the External Flow from a Converging Slot-Hole Film-Cooling Geometry," *Experiments in Fluids,* vol. 38, no. 3, pp. 304-318, 2005.

[46] A. Gehrer, J. Woisetschiliger and H. Jericha, "Blade Film Cooling by Underexpanded Transonic Jet Layers," in *ASME 1997 International Gas Turbine and Aeroengine Congress and Exhibition*, Orlando, 1997.

[47] S. Kim, K. Lee and K. Kim, "A Comparative Analysis of Various Shaped Film-Cooling Holes," *Journal of Heat and Mass Transfer,* vol. 48, no. 11, p. 1929–1939, 2012.

[48] L. El-Gabry, D. Thurman, P. Poinsatte and J. Heidmann, "Detailed Velocity and Turbulence Measurements in an Inclined Large-Scale Film Cooling Array," *ASME Journal of Turbomachinery,* vol. 135, no. 6, 2013.

[49] D. Thurman, L. El-Gabry, P. Poinsatte and J. Heidmann, "Turbulence and Heat Transfer Measurements in an Inclined Large Scale Film Cooling Array – Part II, Temperature and Heat Transfer Measurements," in *ASME 2011 Turbo Expo: Turbine Technical Conference and Exposition*, Vancouver, 2011.

[50] J. Pietrzyk, D. Bogard and M. Crawford, "Effects of Density Ratio on the Hydrodynamics of Film Cooling," *ASME Journal of Turbomachinery,* vol. 112, no. 3, pp. 437-443, 1990.

[51] P. Johnson, V. Shyam and C. Hah, "Reynolds-Averaged Navier-Stokes Solutions to Flat Plate Film Cooling Scenarios," 2011.

[52] *Fluent Theory Guide,* ANSYS Inc., 2015.

[53] *CFX-Solver Theory Guide,* ANSYS Inc., 2015.

[54] *Fluent Advanced Add-On Modules – I. Ansys Fluent Adjoint Solver,* ANSYS, Inc., 2015.

[55] A. Tzanakis, "Duct Optimization Using CFD Software 'ANSYS Fluent Adjoint Solver'," Goteborg, Sweden, 2014.

[56] T.-H. Shih, W. Liou, A. Shabbir, Z. Yang and J. Zhu, "A New K-epsilon Eddy Viscosity Model for High Reynolds Number Turbulent Flows: Model Development and Validation," United States, Cleveland, 1994.

[57] *ANSYS ICEM CFD,* ANSYS Inc., 2015.